Experimental and Mechanistic Study of Copper Electrodeposition in the Absence and Presence of Chloride Ions and Polyethylene Glycol

by

Maria Eugenia Huerta Garrido

A thesis
presented to the University of Waterloo
in fulfillment of the
thesis requirement for the degree of
Doctor of Philosophy
in
Chemical Engineering

Waterloo, Ontario, Canada, 2007

Author's declaration

I hereby declare that I am the sole author of this thesis. This is a true copy of the thesis, including any required final revisions, as accepted by my examiners.

I understand that my thesis may be made electronically available to the public.

Abstract

The trend to miniaturize electronic devices has led to the development of new fabrication processes. Copper electrodeposition has been used extensively in the fabrication of microelectronic circuits due to the excellent conducting properties of this metal. Control of the operating conditions and understanding of the mechanism of metal deposition is necessary in order to successfully produce the micron–scale features required in these new devices. The implementation of new processes and operating conditions in the fabrication of microelectronic devices has spurred a considerable amount of research into their understanding and improvement.

An approach to achieve the desired electrodeposits is the incorporation of mixtures of chemical additives into the electroplating solutions. Many modeling and experimental studies have been devoted to exploring the mechanisms by which additives operate. However, details of these mechanisms are not completely understood. A part of this study focuses on the investigation of the conditions and dynamics of the adsorption and desorption of the additives chloride ions and polyethylene glycol (PEG) on copper substrates in voltammetry and multi–step voltammetry–chronoamperometry experiments. Voltammetry scans are classified into three categories according to the range of potentials where the inhibition of Cu^{2+} reduction in the presence of various concentrations of Cl^- and PEG is observed. Each type is explained based on the results of this study and the ideas presented in the literature on how the conformation of adsorbed PEG on the substrate can change during the course of deposition.

One of the techniques that is widely used to study electrochemical processes is electrochemical impedance spectroscopy (EIS). Insight into these processes gained from measured EIS data is better when it is combined with the use of a physicochemical model. However, the models typically used involve a number of simplifying assumptions, partly due to mathematical complications. One of the purposes of this study is to relax some of these assumptions such as the neglect of convection, migration and homogeneous reactions and investigate their effect by comparing the model results to experimental data. This approach is applied to Cu^{2+} reduction onto a rotating disk electrode in acidic additive–free solutions. Estimates of the kinetic parameters are obtained with the non-linear least squares method. A statistical analysis reveals that the model is further improved by accounting for the correlation between consecutive residuals. The experimental data are found to be poorly predicted when the parameters estimated from the full model are used in simpler models that do not include convection and/or homogeneous reactions.

The model of Cu^{2+} reduction in additive–free solutions is extended to account for the presence of Cl$^-$ and PEG under transient conditions. The model accounts for the formation of the inhibiting film, blockage of adsorption sites on the electrode surface and displacement of the inhibiting film by depositing copper. A distinction is made between the condition when the electrode is completely covered with the inhibiting film and when it is only partially covered. Estimates of the kinetic parameters are obtained from fitting the model to electrode responses of linear potential scans obtained at various Cl$^-$ and PEG concentrations. The model is able to predict both the sudden loss of inhibition that occurs at intermediate Cl$^-$ and PEG concentrations and the more gradual increases in current at low and high additive levels. EIS spectra are also predicted and compared to measured ones.

Acknowledgements

I want to thank the various people who made possible my stay in the University of Waterloo and the successful completion of my degree. I would like to express my gratitude to my thesis supervisor Dr. Mark Pritzker for all his useful advice and continuous support. His discipline to work and expertise in electrochemistry has provided me with a good basis to work during this endeavor.

Thank you for the valuable comments of Drs. Thomas Duever, Neil McManus, Jessada Jitjareonchai, Alan West, Hector Budman, Mario Ioannidis and Dan Thomas. I am also indebted to all the staff members that facilitated the services that I used to do my research work.

The research presented in this thesis was conducted through the support from a scholarship offered by Consejo Nacional de Ciencia y Tecnología (CONACYT), Mexico and operating funds from the National Sciences and Engineering Research Council of Canada (NSERC). The financial support provided by these research councils is gratefully acknowledged.

I want to express my deepest gratitude to my parents, my sisters and my husband. You have been very important for me to go through this long journey. With all my love, I dedicate this thesis to you. Dear parents, this thesis is the result of your example of hardworking to overcome all obstacles and materialize my dreams. No matter the distance, you and my sisters have always been on my mind and my heart. My beloved Guillermo, all our efforts and sacrifices have finally been compensated with this achievement. Thank you for your company, encouragement and for being my inspiration.

Contents

List of Tables

List of Figures

Nomenclature

Acronyms:

AC	Alternating current
CE	Counter electrode
CEAC	Curvature enhanced accelerator coverage model
CV	Cyclic voltammetry
DC	Direct current
EIS	Electrochemical impedance spectroscopy
EQCM	Electrochemical quartz crystal microbalance
FFT	Fast Fourier transform
FRA	Frequency response analysis
jcr	Joint confidence region
LSV	Linear sweep voltammetry
MSE	Mercury-mercury sulfate reference electrode
OCP	Open circuit potential
PSD	Phase-sensitive detection
RDE	Rotating disk electrode
RE	Reference electrode
RRDE	Rotating ring–disc electrode

RSS	Error or residual sum of squares
SERS	Surface–enhanced Raman spectroscopy
WE	Working electrode

Indices:

b	Bulk conditions
exp	Experimental response
im	Imaginary component
j	j^{th} data point
min	Minimum value
mod	Model response
real	Real component
s	Value evaluated on the electrode surface
ss	Value evaluated at steady state conditions

Constants and Variables:

C_{dl}	Double layer capacitance
C_i	Concentration of species i
D_i	Diffusivity of species i
E'	Electrode potential corrected for the solution resistance
E_0	Initial potential
E_a	Potential amplitude
E_{eq}	Equilibrium potential
f	Frequency in cycles/sec

f_k	Autocorrelation function
F	Faraday constant, 96485.31 C/equiv
i	Total current density
i_0	Exchange current density
i_a	Current density amplitude
i_{dl}	Double layer component of the current density
i_f	Faradaic current density
i_L	Limiting current density
j	Imaginary unit, $\sqrt{-1}$
k	Rate constant
K' and K"	Equilibrium constants
n	Number of electrons per mole of reduced species
N_{ss}	Total number of current–potential points
N_{tr}	Total number of impedance measurements
p	Total number of fitting parameters
r	Reaction rate
r_{net}	Net rate at which a species is consumed at the surface
R_{ct}	Charge transfer resistance
R_i	Generation rate by homogeneous reaction of species i
R_s	Solution resistance
R	Gas constant, 8.314 J/(mol K)
s	Laplace transform variable
s^2	Variance
t	Time variable

T	Electrolyte temperature
z	Spatial variable normal to the electrode surface
Z or Z(ω)	Impedance
z_i	Charge transfer coefficient of species i
z_n	Error at nth data point
β	Charge transfer coefficient
δ	Diffusion layer thickness
η	Overpotential
θ or θ_{Cu}	Fractional coverage of Cu(I)
θ_{Clc}	Fractional coverage of CuCl
ϑ	Sweep rate
λ	Parameter that accounts for the linear dependence between two consecutive residuals
ν	Kinematic viscosity of the solution
π	3.1416
ρ_{XY}	Correlation coefficient for the parameters X and Y
υ_z	Normal velocity component
ϕ_s	Potential within the electrolyte
φ	Phase-shift
Γ or Γ_{Cu}	Maximum adsorption density of a monolayer of Cu(I) on the surface
Γ_{Clc}	Maximum adsorption density of a monolayer of CuCl on the surface
Γ_0	Minimum adsorption density of ClCuPEG for a complete coverage
Γ_p	Adsorption density of ClCuPEG on the surface
Γ_s	Saturation adsorption density of ClCuPEG on the surface

φ_y	Phase shift of the variable y
ω	Frequency in rad/sec
Ω	Rotational speed of the working electrode

Matrices:

Cov	Covariance matrix
J	Jacobian

Symbols:

$\overline{(\cdot)}$	Steady state value
$\widetilde{(\cdot)}$	Phasor of a transient variable
$\mathrm{Re}\{\cdot\}$	Real component

Chapter 1

Introduction

Due to its inherent characteristics as a good electronic conductor, copper is preferred over other metals such as aluminium for numerous applications [1, 2]. One of the main applications of copper deposition is for the microelectronics industry where the fabrication of integrated circuits requires the filling of micron and sub-micron scale features. Studies on the filling of such features as trenches and vias have shown that its effectiveness is strongly affected by the operating conditions of the process, as well as by the geometry and size of these features. The mode of deposition called superfilling is desired because it ensures that the feature is filled without any voids or seams. As will be discussed, superfilling requires careful control of the electrodeposition process through application of the appropriate current or potential in the presence of specific chemical reagents.

A factor that affects how the deposit grows on flat or patterned electrodes is the presence of additives in the plating solution. Additives such as chloride ions, polyethylene glycol (PEG) and 3-mercapto-1-propanesulfonate acid (MPS) or bis(3-sulfopropyl) disulfide (SPS) and Janus Green B have been successfully used to help achieve the required physical properties of copper deposits [3–17]. They can modify the mechanism and rate of Cu^{2+} reduction and enable superfilling to occur. Since these additives have specific effects on metal ion reduction, they are added in combination with one another. Thus, a crucial aspect to the successful use of these additives is to understand not only their specific effects, but the interplay between their effects when present together. This has spurred a great deal of research in recent years.

Electrochemical impedance spectroscopy (EIS) has become a very popular technique to study electrochemical processes such as metal electrodeposition and corrosion and gain insight into the phenomena occurring at the interface between the electrode and the electrolytic solution. By sampling a system in the frequency domain, EIS can effectively distinguish between processes that remain convoluted in the time domain. This technique is used alone or in combination with other techniques such as chronopotentiometry, chronoamperometry and voltammetry. Unlike some other electrochemical techniques, EIS data must be interpreted in terms of a mathematical model for the system in order to be most useful. Nor surprisingly, the more details the model can provide concerning the important physicochemical phenomena that occur, the more illuminating the EIS technique can be.

1.1 Research Motivation

Many models have been used to describe the conditions in electrochemical impedance spectroscopy experiments. Among the approaches that have been followed for metal deposition is the use of electrical circuit elements as analogs for phenomena in an electrochemical system [18–24]. Although this approach is very popular and has been successful in many respects, it has been found to be ambiguous in some cases because more than one electrical circuit configuration can be used to represent the same electrochemical process [25]. Another approach to interpret EIS data is the use of a mechanistic model including kinetics and/or mass transport effects [26–40]. The development of such a model inevitably requires some assumptions that can be assessed by comparison with experimental data. The development of a more complete model would allow more insight into the electrochemical process to be gained and a wider range of conditions to be investigated. This is one of the objectives of the current study. It begins with the analysis of additive–free copper deposition and is subsequently extended to copper deposition in the presence of Cl^- and PEG. The model for Cu^{2+} reduction in the presence of Cl^- and PEG accounts for the effect of the concentrations of both additives on the inhibition of copper electrodeposition, something which has not been previously investigated.

Since the introduction of copper electrodeposition for feature filling in the microelectronics industry, many experimental and modeling studies have been conducted to better understand the mechanisms involved due to the presence of additives. However, the conditions for the adsorption and desorption of the accelerating and inhibiting species are not yet completely understood. Consequently, a portion of this study is devoted to experiments on the conditions for the formation and disruption of the inhibiting film during copper deposition onto planar substrates in the presence of Cl^- and PEG.

1.2 Objectives

The overall objectives to be achieved in this study are:

- To develop a comprehensive physicochemical model for copper electrodeposition to be used in the analysis of electrochemical impedance spectroscopy experiments.
- To investigate the conditions for the adsorption and desorption of Cl^- and PEG on a copper substrate and their effect on copper deposition.
- To develop a model to account for the effects of Cl^- and PEG on the electrode response for Cu^{2+} reduction during linear potential scans and EIS experiments.

Toward these objectives, the following research topics were investigated:

i) Electrodeposition of copper in the absence of additives.

   Experiments were conducted to obtain EIS and steady state polarization curves for Cu^{2+} reduction on a rotating disc electrode (RDE). A comprehensive 1-D model was developed for plating on a RDE incorporating diffusion, convection, migration, electrode reactions and homogeneous reactions. There was a special interest in incorporating some additional effects not considered in earlier impedance studies, *e.g.*, effects of convection, migration and homogeneous reactions. An impedance model was derived by linearizing the various kinetic and mass transport equations. The kinetic parameters of the model were estimated using non-linear regression to fit the model to experimental data. A detailed statistical analysis was also conducted to account for correlation between model residuals and improve the fitting.

ii) Electrodeposition of copper in the presence of the additives Cl^- and PEG.

- ii.a) Voltammetry and multi-step chronoamperometry-voltammetry experiments into Cu^{2+} reduction on a RDE in the presence of Cl^{-} and PEG were conducted. The effect of Cl^{-} and PEG concentrations on the inhibition of Cu^{2+} reduction was investigated. Attention was also focused on the dynamics of inhibiting film formation. The relation between electrode responses and the adsorption and desorption of the additives is also discussed on the basis of these experimental results and others reported in the literature.
- ii.b) The 1-D model developed for additive-free deposition was extended to account for copper deposition in the presence of Cl^{-} and PEG. Ideas obtained on the basis of the experimental results described in ii.a) above and from the literature were incorporated into this model. The mechanism proposed accounts for the interaction of additives, Cu^{2+} and the electrode during electrodeposition. These interactions include such aspects as the formation of the inhibiting film, blockage of adsorption sites on the electrode surface and displacement of the inhibiting film by depositing copper. This work improves upon previous models by quantitatively taking into account the effects of both Cl^{-} and PEG. A comparison of the model to experimental cathodic scan curves enabled the estimation of kinetic parameters. Once the kinetic parameters were obtained, the model was used to simulate EIS spectra and some experiments conducted in ii.a) for comparison with measured data.

1.3 Structure of the Thesis

This thesis is organized into 6 chapters and 1 appendix. In Chapter 2, general aspects of copper electrodeposition are introduced. The Damascene process used to fill small features in the industry is described. A classification of the additives commonly used in the Damascene process is presented according to their effect on the rate of Cu^{2+} reduction. Fundamentals of the physics and chemistry of the electrode-electrolytic solution interface are also briefly described. The principles of the electrochemical techniques used in this study are presented.

In Chapter 3, the development of a model for metal deposition accounting for some of the phenomena neglected in previous studies is presented. This model is applied to additive–free Cu^{2+} reduction. This chapter also includes a detailed statistical analysis of the model fitting and an analysis of neglecting phenomena such as convection, migration and homogeneous reactions that has been common in previous impedance studies.

Chapter 4 includes the results of voltammetry and multi–step experiments to study the effects of Cl^- and PEG on the inhibition of Cu^{2+} reduction and the conditions for the formation and disruption of the inhibiting film.

In Chapter 5, the development of a model applied to Cu^{2+} reduction in the presence of Cl^- and PEG is presented. This model is based on the model developed in Chapter 3 and ideas obtained from the experiments in Chapter 4 and the literature. The model is fit to experimental current–potential curves and then used to predict EIS spectra that are compared to the measured ones. A summary of the contributions of this study and directions for future research are presented in Chapter 6. The linearization procedure of the model expressions in Chapters 3 and 5 used to fit to the impedance data is presented in the Appendix.

Chapter 2

Background

Copper has found widespread applications and been the subject of a great deal of electrochemical research over the years. For a long time, aluminum has been used as the metal of choice in the fabrication of interconnects for integrated circuits. The trend of technology is to use progressively smaller devices, which demands more efficient connections. This has lead to an upsurge of interest in the use of copper for such applications. Not surprisingly, the use of electrodeposition of copper as the basis for the fabrication of such devices has been widely considered due to its relative ease and the vast knowledge of this topic that has already been accumulated. In this chapter, some basics of copper electrodeposition and its analysis are discussed.

2.1 Copper Electrodeposition

Copper is an excellent substitute for aluminium in many electronic applications due to its unique characteristics such as: i) superior electromigration resistance, ii) lower wiring resistance and iii) higher allowable current density [1]. These characteristics improve the signal transmission in circuits when the size of the wire is reduced. The better the transmission in the wiring, the lower the power consumption of the device. For this reason, interest rose in the microelectronics industry during the 1990's for the use of copper in the fabrication of chips [1, 41]. When copper was introduced as a substitute for aluminium, a variety of techniques in addition to electrodeposition, such as physical vapor deposition, chemical vapor deposition and electroless plating, were considered. However, *electrodepo-*

sition or *electroplating* has proved to be effective, particularly for filling and coating small structures [1].

One of the techniques currently used to deposit copper in circuits is so-called *Damascene electroplating.* The purpose of this technique is to fill features having sizes on the order of hundreds of nanometers with copper. The substrate used is a silicon wafer that is patterned with sub-micron features such as trenches and vias. The first step is to sputter a *barrier layer* made of tungsten, tantalum, niobium or tantalum nitride on top [10, 42]. The main purposes of the barrier layer are to inhibit diffusion of copper into the silicon wafer and improve the adhesion of the subsequent deposit. Over the barrier layer is spread a very thin *seed layer* of copper layer; this layer has a thickness on the order of tens of nanometers and is applied by chemical vapor deposition. The seed layer allows uniform conductivity over all the points of the surface during subsequent electrodeposition. Under certain conditions, good deposits can be achieved in the absence of a seed layer [43]. After the seed layer is formed, copper is electrochemically deposited, filling the features of the pattern. Typically, a bump is formed on the top surface of the deposit at the end of the filling step. In such cases, it is necessary to remove this excess material by using a process such as *chemical mechanical planarization* [44] or electropolishing [45].

2.2 Deposit Terminology for Patterned Electrodes

Deposits are classified according to the manner in which the deposit grows inside a trench or a via (Fig. 2.1) [44]. The term *conformal deposition* is used to describe the phenomenon that occurs when a deposit grows at the trench or via wall and bottom at the same rate. This kind of deposit usually results in the appearance of a seam when the process is complete. If the deposit at the mouth of the feature closes before the portion in the base of the feature, then the deposition is termed *subconformal.* This type of deposit leads to the formation of voids which can be as large as 10% of the trench width [14]. The formation of voids and seams is attributed to diffusion limitations of the metal ion that becomes depleted at the bottom of the feature since the trench size is smaller than the diffusion layer thickness [14, 46]. Obviously, the optimal condition occurs when the feature is completely filled by the deposit metal without any voids or seams. For this to happen, deposition must

Figure 2.1: Classification of deposition modes in a trench or via.

occur preferentially at the base and fill the feature bottom-up according to what is termed *superfilling* or *superconformal deposition*. One of the major challenges when depositing copper in small devices with features of micron or sub-micron scale is complete filling of the features. Voids or seams formed inside the feature deposit result in poor conduction within the circuit and deposit degradation. Since the introduction of the Damascene process, numerous studies have been conducted to reduce the formation of voids in features with aspect ratios (depth/width) as high as 5 and widths as small as 100 nm [47]. To improve the filling of recesses and deposition of micron and sub–micron size features, additives are used during plating [3–7, 9–17, 48–54]. Also, the use of transient techniques such as pulsed current plating has been used to achieve superfilling [55].

2.3 Additives

The presence of small amounts of additives in a solution used for metal electrodeposition has several functions. The additives can affect the roughness, structure and properties of the deposit by controlling the deposit growth mechanism [10, 56, 57]. When this effect leads to the formation of smaller and more numerous grains, an increased brightness of the deposit is observed. Additives also affect the kinetics of deposition by formation of complexes with metal ions or by blockage of adsorption sites on the electrode surface. The additive molecules modify the deposit when they adsorb, desorb or are incorporated with the metal or when they float on the surface and block part of the deposit.

Additives can be classified according to their function as accelerators, inhibitors or carriers, and levelers. The accelerators increase the rate of metal deposition on the sites where they adsorb or float and create brighter deposits. These additives usually contain disulfide bonds and sulfonic acid groups. The inhibitors suppress the deposition rate on the sites where they adsorb or block the adsorption of other species and promote the formation of ductile copper films. Finally, the levelers suppress local deposition and tend to adsorb preferentially on surface protrusions, impeding the growth on those spots and allowing deposition on other areas to catch up. Some authors [11, 58] consider that the leveling effect is not the result of just one additive, but is produced when accelerator and inhibitor effects interact.

Accelerators of copper deposition include chloride ions added as NaCl, KCl or HCl to the plating baths and bromide ions. 3-mercapto-1-propanesulfonate acid (MPS) or its dimer bis(3-sulfopropyl) disulfide (SPS), 8-hydroxy-7-iodo-5-quinoline sulfonic acid (HIQSA) and 3-N,N-dimethylaminodithiocarbamoyl-1-propanesulfonic acid (DPS) are also added as accelerators to the electrolytic bath. Inhibitors used in copper plating solutions include polyethylene glycol (PEG) and levelers include thiourea, Janus Green B and benzotriazole.

For the deposition of copper in trenches and vias different additives are combined in the plating bath. A common combination that produces defect-free deposits includes chloride ions, polyethylene glycol and SPS or MPS [4, 5, 7, 9, 10, 12, 14–16]. Janus Green B is often added to this mixture [3, 6, 8, 11, 13, 17]. Superfilling has also been observed on deposits formed in baths containing DPS, Cl^- and PEG [48]. Under certain conditions, excellent deposits have been shown to be possible if copper is electrodeposited in the presence of only bromide ions and PEG [50] or chloride ions and PEG [49, 54]. The effect of Cl^- and PEG on copper electrodeposition will be investigated in detail later in Chapters 4 and 5.

It should be noted that electroless plating with the use of the additives HIQSA and PEG has been reported to produce void-free deposits [59].

2.4 Electrode-Electrolyte Interface

A three-electrode system used for electrodeposition is composed of a cathode (also known as the working electrode WE), an anode (counter electrode CE) and the reference electrode (RE) (see Fig. 2.2). When the system is connected to a power source, current flows through the system. The electrode potential of the working electrode is always measured with respect to a reference. The potential of an ideal reference electrode remains stable and well-known even when current flows through the circuit. When current flows, the required working electrode potential must overcome the ohmic resistance of the solution adjacent to the working electrode and the kinetic and mass transfer barriers at the electrode surface. A description of the system in which electrodeposition experiments are normally conducted is given in this section. The focus is on the working electrode where metal deposition occurs.

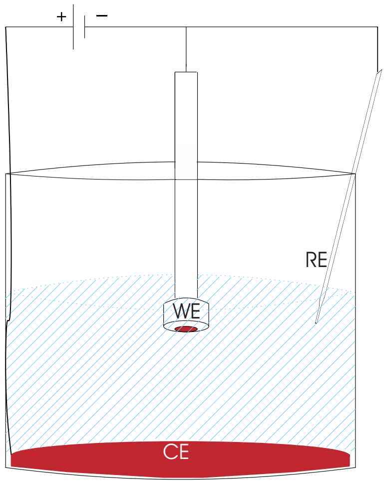

Figure 2.2: Electrochemical cell.

2.4.1 Double Layer

When the working electrode is immersed in the electrolytic solution, a very thin region called the *double layer* is formed at the electrode-electrolyte interface. The double layer contains a distribution of ions at the interface (see Fig. 2.3). Its name is derived from the separated distribution of species having opposite charges. Some ions are specifically adsorbed at the interface, while others are located in a very narrow region close to the interface. The distribution of these ions near the electrode depends on the electrostatic forces existing in the interfacial region. As a whole, the charged metal and the ionic distribution in the solution can be represented as a capacitor. The temporal structural changes of the double layer can be characterized by a time constant described in terms of the *double layer capacitance*. The distribution in the double layer changes whenever the potential of the electrode changes [60].

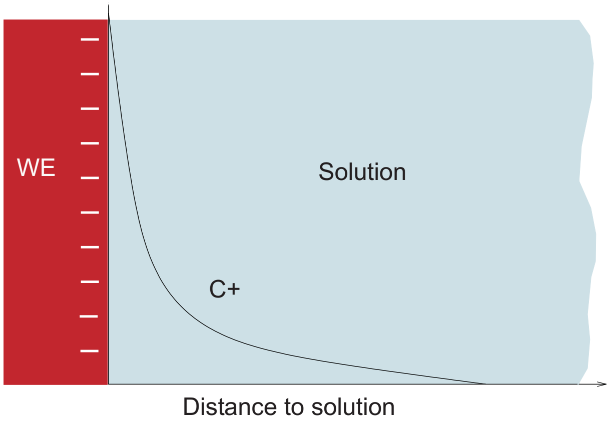

Figure 2.3: Concentration profile of counter-ions in the double layer.

2.4.2 Kinetics

In order to deposit a metal electrolytically, a net current must be passed through the system. In the case of copper electrodeposition from acidic sulphate solutions, the reduction reactions that take place at the working electrode surface are

$$Cu^{2+}_{(aq)} + 2e^- \rightleftharpoons Cu^0_{(s)}, \tag{2.1}$$

$$2H^+_{(aq)} + 2e^- \rightleftharpoons H_{2(g)}. \tag{2.2}$$

The total cathodic current is the sum of the contributions due to each of these reactions. Since the main purpose of the process is to deposit copper, the experimental conditions should be set so that as much of the current as possible is invested in the reduction of copper and the current efficiency is as high as possible. If the efficiency is lower than 100% and hydrogen evolution occurs, not only is some current wasted but also the morphology of the deposit can be adversely affected, producing rough and porous deposits. Due to the noble nature of copper, it is generally not difficult to electrodeposit copper with current efficiency at or very close to 100%.

While copper is deposited at the working electrode under acidic conditions, the possible anodic reactions taking place at the counter electrode are usually

$$H_2O_{(l)} \rightleftharpoons \frac{1}{2}O_{2(g)} + 2H^+_{(aq)} + 2e^- \tag{2.3}$$

or

$$Cu^0 \rightleftharpoons Cu^{2+} + 2e^- \tag{2.4}$$

depending on whether an inert material (*e.g.*, Pt, Au) or a reactive material (*e.g.*, Cu^0) is used as the anode.

2.4.3 Mass Transport

Electrode kinetics depends on surface concentrations which are known only at the beginning of the process; in a well-mixed solution, they are equal to their respective values in the bulk of the solution. However, once metal deposition starts, the concentrations of all species at the electrode-electrolyte interface change. A region called the *mass transport layer* forms close to the solution interface with a thickness depending on the concentration distribution in the solution and the hydrodynamics. Throughout this layer, concentrations vary with the distance from the electrode surface as a result of mass transport and charge transfer occurring during electrodeposition. Beyond the mass transport layer, the concentrations of the various species are considered constant and equal to the bulk concentration in a well-mixed solution.

Three different mechanisms are known to promote the transport of dissolved species in solution -diffusion, convection and migration. Diffusion transports species to or from the electrode due to concentration gradients. A common experimental approach for studying electrodeposition uses the rotating disk electrode (RDE) since it provides well-defined and reproducible hydrodynamic conditions. Migration is the third mode of transport and arises from electrostatic forces that move charged species in an electric field. Diffusion and convection operate on both ions and neutral species whereas migration affects ions only.

2.5 Electroanalytical Techniques

Electroanalytical techniques are used to study the kinetics and mass transport phenomena associated with electrochemical systems. In this study, some of the most common techniques reported for copper electrodeposition were used. They include chronopotentiometry, chronoamperometry, voltammetry and electrochemical impedance spectroscopy. Basic aspects of each of these techniques are reviewed in the sections below.

2.5.1 Single Step Methods

Chronopotentiometry and chronoamperometry involve the monitoring of the response of a system over a period of time to a step change of the input signal. In the first case, the input signal is current and the response is the electrode potential. In the second case, the input signal and response are reversed. These techniques can be used to obtain the steady state polarization curve of a system in addition to investigating its transient behavior. This requires that the input signal be applied and response monitored long enough for steady state to be reached. This also requires that a steady state can actually be reached for a given set of conditions.

2.5.2 Voltammetric Methods

The linear sweep voltammetry (LSV) technique involves varying the electrode potential linearly with time in either the cathodic or anodic direction and continually measuring the current. Cyclic voltammetry (CV) is related to LSV in that it combines two linear potential scans, first in one direction and then switched back in the other direction [61]. The input potential signal thus takes the form of a triangular wave form. In both techniques, the rate at which potential is scanned is a variable that can be used to advantage to investigate a system. Often the sweep rate is made slow enough that the system has time enough for relaxation and the electrode response approximates steady state behavior [62].

The LSV shown in Fig. 2.4 is typical of the electrode response during Cu^{2+} reduction. The vertical axis represents the current density i which is equivalent to the current normalized with respect to the electrode area. The horizontal axis represents the overpotential η which expresses the deviation of the electrode potential from the equilibrium value. Three regions can be identified according to overpotential. At low overpotential, the electrochemical process is controlled by kinetics of the reaction taking place at the electrode surface. At intermediate overpotential, the reaction proceeds under mixed kinetic-mass transfer control. Finally, at high overpotentials, the process is controlled entirely by mass transfer, most commonly the rate at which the reactant is transported from the bulk to the electrode surface. Secondary reactions such as hydrogen evolution usually only begin when Cu^{2+} reduction is at or near mass transfer limiting conditions. In the mass transport controlled region, the current density for electrodeposition reaches the maximum possible value called the limiting current density i_L.

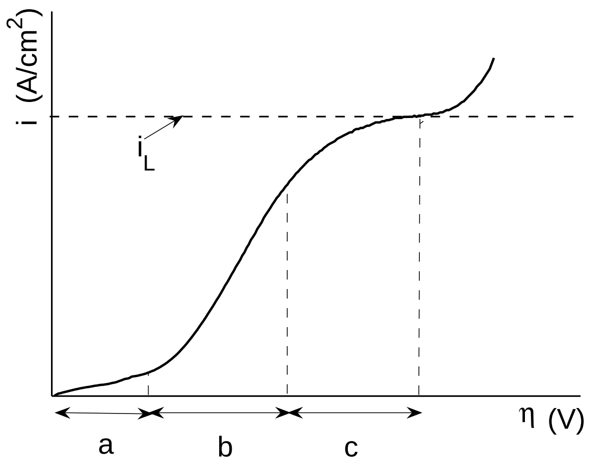

Figure 2.4: Rate-control regions in a typical polarization curve: a) kinetic, b) mixed kinetic-mass transport and c) mass transport control.

2.5.3 Electrochemical Impedance Spectroscopy

In the previously discussed techniques, the response to large perturbations in electrode potential or current imposed on the electrode is measured. In contrast, electrochemical impedance spectroscopy (EIS), also known as the alternating current (AC) technique, consists of measuring the electrode response when a small-amplitude periodic sinusoidal wave is superimposed on a pre-specified constant input signal. Although electrochemical processes as a whole are generally non-linear, the imposition of a small-amplitude perturbation allows the response to be approximated as a linear system. The ratio of the potential and the current perturbations in the frequency domain is called the *impedance* Z. The term *spectroscopy* originates from the fact that the impedance of a system is measured over a range of frequencies. This technique can be carried out in either potentiostatic or galvanostatic mode. Fig. 2.5 shows a typical input signal for potentiostatic mode of operation. The variables that characterize this wave are the DC input signal $\overline{E}$, frequency (f in cycles/sec or ω in rad/sec, where ω=2πf) and a small amplitude (E$_a$). The output signal consists of a wave with DC output signal $\overline{\imath}$, same frequency f but with a different amplitude (i$_a$) and a phase-shift (φ), as depicted in Fig. 2.6 for the potentiostatic case. EIS is often used in combination with other techniques to study electrodeposition. It can reveal information about the electrode-solution interface, its structure and the reactions that take place there, as well as the growth mode of the deposit [26–29, 34, 36, 63–66]. EIS has also been used to study the adsorption and aging of additives and their effect on metal deposition [20, 21, 28, 30, 31, 35, 37, 38, 54, 67–71].

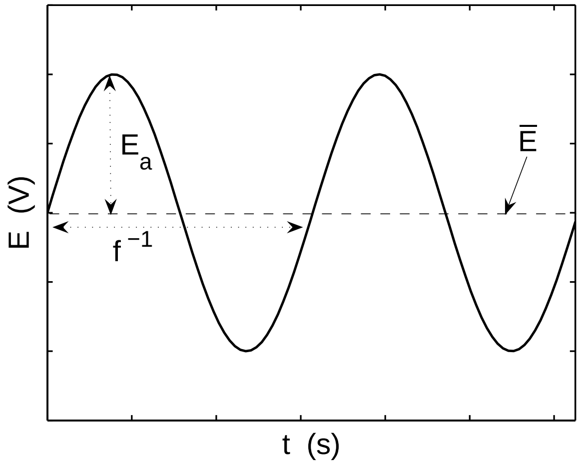

Figure 2.5: Sinusoidal input signal in EIS operating in potentiostatic mode.

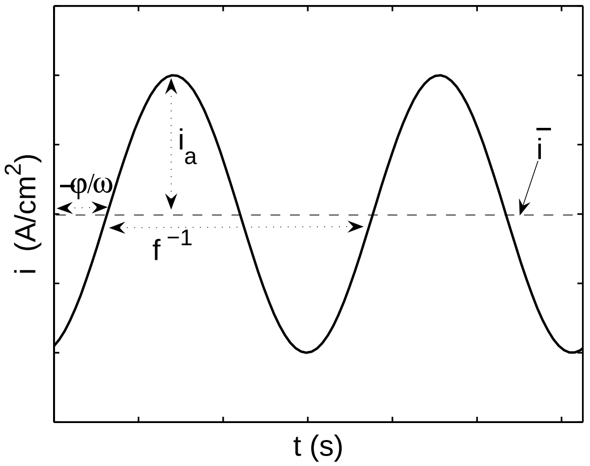

Figure 2.6: Sinusoidal output signal in EIS operating in potentiostatic mode.

EIS modeling

EIS has proven to be a very good technique for obtaining quantitative information concerning electrochemical systems. Several approaches are used to interpret EIS data for the study of electrochemical systems such as metal deposition, dissolution, corrosion and electrowinning. One approach is the use of electrical circuit components (resistors, capacitors or inductors) connected in series and/or parallel as linear analogs to represent physical or chemical elements of electrochemical systems [18–24]. Although the mathematical analysis using this approach is relatively simple, it can lead to ambiguous results because more than one electrical circuit can sometimes represent the same electrochemical process [25]. In addition, the parameters so obtained often cannot be directly related to the parameters typically used in physicochemical models. A different approach is to begin with a physicochemical model describing kinetics and/or mass transport effects [26–40]. The purpose of the EIS technique is to measure the response of the system to a small-amplitude perturbation. Thus, the response during an EIS experiment can be obtained by linearizing the physicochemical model. Subsequent mathematical analysis leads to an expression for the impedance that can be compared to experimental EIS data. This approach has the advantage that EIS data are interpreted in terms of a physicochemical model and the corresponding parameters directly obtained. On the other hand, the mathematical analysis required for most realistic models is lengthy enough that important simplifying assumptions are typically made. A third approach combines the use of an electrical circuit and a simplified physicochemical model. In this case, a circuit–based model is first fitted to experimental data to obtain values for every circuit component. Then, the circuit components are related to physical or chemical parameters in the system [63, 64, 67, 69, 71].

Graphical interpretation

There are several ways in which EIS results can be graphically represented. The most common include Nyquist and Bode plots. In a Nyquist plot, also known as a complex plane or Argand plot, the negative of the imaginary component of the impedance Z_{im} is plotted versus the real component Z_{real} at different frequencies. The Bode plot can be represented in two ways depending on the variable used in the vertical axis: $\log|Z(\omega)|$ versus $\log(\omega)$ or $\log(\varphi)$ versus $\log(\omega)$.

The Nyquist plot determined over a range of frequencies will generally take the form of one or more semi-circles, as shown in Fig. 2.7. Some information that can be directly obtained from the Nyquist plot is the solution resistance R_s and the charge transfer resistance R_{ct}. R_s is given by the intersection of the impedance data with the real axis at high frequencies. The diameter of the semi-circle is equal to the charge transfer resistance. If

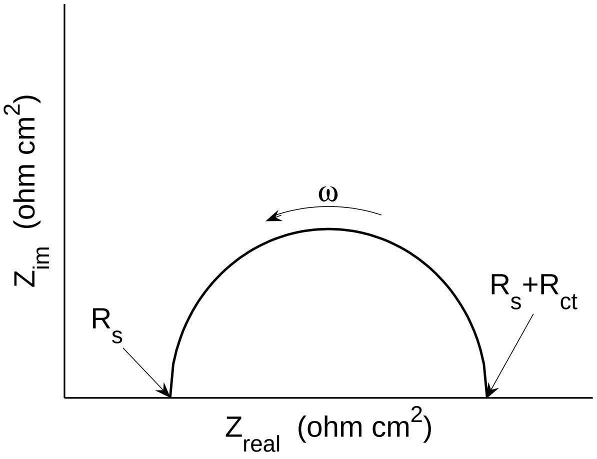

Figure 2.7: General Nyquist plot.

the process involves the adsorption of one or more species, then more than one semicircle is observed in the Nyquist plot [72]. As in the case of LSV plots, two regions can be distinguished in a impedance plot: a charge transfer-controlled region at high frequencies and a diffusion-controlled region at low frequencies [65].

Measurement techniques

The techniques that have been used in experiments to acquire impedance data include: i) ac bridges, ii) Lissajous figures, iii) phase-sensitive detection (PSD), iv) fast Fourier transform (FFT) and v) frequency response analysis (FRA).

The impedance of the electrochemical cell and with some assumptions the impedance of the working electrode can be estimated using alternating current bridges. This method consists of regulating the values of the reference resistance and capacitance that balance the series connection forming the ac bridge at a specific frequency. This connection is formed by the cell, two resistors of known resistance and the reference resistance and capacitance which can be connected in series or parallel. The impedance of each element in the circuit is calculated using well-known expressions for resistances, capacitors and combinations of them. Although this technique may be accurate, it is very time consuming [61, 62].

A direct method used to measure impedance uses an oscilloscope to record the applied and response sinusoidal signals versus time. A Lissajous curve, which appears as an ellipse, results from a plot of the response signal versus the applied signal at a specific frequency. The components of the impedance are calculated from the dimensions of the ellipse. A drawback of this technique is that it is sensitive to noise and frequency limited [25].

PSD is a technique that consists of transforming the time-dependent wave signal by multiplication with a rectangular wave (reference signal) of the same frequency. The resulting expression is averaged over time. The final expression depends only on the amplitude of the initial signal and the phase-shift between the measured and the reference signal. The amplitude of the signal and the phase-shift define the impedance of the system [25].

The FFT technique applies the imaginary Laplace transform (where $s = j\omega$) to both the input and output time-dependent signals. The ratio of the resulting frequency-domain variables for potential and current is the impedance. The Laplace transform requires the integration in time from zero to infinite. However, sampling of data over an infinite period of time is unfeasible. Sampling is adjusted in order to overcome the problems associated with obtaining data over a limited period. Sampling time is synchronized with the wave period and sampling frequency is set to be at least twice the highest frequency of the measured signal [72].

The FRA technique transforms the measured signals by multiplication with two kinds of sinusoidal reference waves and integration over one or more wave periods. One kind of reference signal is in phase with the measured wave while the other kind is shifted by 90^o. This transformation generates the real and imaginary parts of the transformed variables separately which are used to obtain the impedance [25]. With this kind of transformation, higher-order harmonics which cause non-linearity in the measured signal are canceled. The FRA technique has become the most common method used in commercial instruments to measure EIS and is employed during the experiments of this study.

Chapter 3

Modeling of Additive-Free Copper Electrodeposition

Simplified models and circuit analogs are commonly used to describe electrochemical processes when applying electrochemical impedance spectroscopy (EIS). One of the objectives of the modeling presented here is to relax some of the simplifications considered in models used for EIS analysis. The analysis is applied to additive–free copper electrodeposition from acidic sulphate solutions, a topic that has received considerable interest over the years due to its technological importance. The results of this analysis will also be used for the modeling of Cu^{2+} reduction in the presence of Cl^{-} and PEG presented in Chapter 5. Kinetic parameters for Cu^{2+} reduction are obtained by fitting the model to experimental EIS and steady state current–potential data. The results from this chapter formed the basis for a paper that has already been published [73].

3.1 Background

Most EIS models found in the literature that account for mass transport include diffusion only in the transport equations, but neglect convection and migration [29, 30, 36–38, 64]. In some of these cases, hydrodynamic effects in the vicinity of rotating disk electrodes are included only to define the mass transport boundary layer thickness, but not added as a term in the mass transport equation. Some researchers have included diffusion and convection within the transport equations. Diffusion and convection have often been incorporated as a complex variable called the Warburg impedance in models that consider uncoupled mass transport equations [27, 32, 33, 35, 39, 40]. This approach involves solving the transport equation that includes diffusion and convection through a semi–infinite boundary layer. The Warburg impedance relates the concentration to the concentration gradient at the electrode surface [40]. The model proposed in the present study accounts for species transport by diffusion, convection and migration as well as electrochemical and homogeneous reactions. This model is used in the analysis of Cu^{2+} reduction onto a rotating disk electrode (RDE) immersed in acidic sulphate solutions.

Many studies of Cu^{2+} reduction in the absence of additives have fit models to data obtained from various electrochemical techniques including pulse current, pulse reverse plating, voltammetry and EIS [28, 35, 36, 55, 64, 67, 69, 74–79]. In a few cases, parameters for the Cu^{2+} reduction system have been estimated by fitting models to voltammetry data and impedance data using nonlinear regression methods [69, 74]. However, most previous analyses of the reduction of Cu^{2+} using physicochemical models to obtain kinetic parameters have been based on a qualitative comparison or approximate fitting. In this chapter, particular focus is put on more rigorous least–square fitting to obtain the system parameters and a statistical analysis of the fit of the model to the experimental data. This includes analysis of the correlation between the parameters as well as between the residuals. Also included in this chapter is a sensitivity analysis of the parameters and comparisons of the predicted steady state and impedance plots using simpler versions of the model.

3.2 Experimental

All experiments were conducted in electrolytes prepared with cupric sulfate pentahydrate (99.5%, VWR), sulfuric acid (98%, Fisher Scientific) and distilled water at room temperature. Measurements were carried out at three different $CuSO_4$ compositions described in Table 3.1. In all cases, the H_2SO_4 concentration was maintained at 1.8M. These concentrations were chosen on the basis of plating solutions typically used in the fabrication of interconnects for integrated circuits. Prior to each experiment, the working electrode was polished using SiC–type abrasive paper (600 and 1200 grade) and 0.3μm alumina powder. The cell consisted of a 0.635cm diameter copper rotating disk working electrode, 3.8cm

Table 3.1: Experimental conditions.

Experiment	$[CuSO_4]$, M	rpm
1	0.25	500
2	0.25	200
3	0.25	1000
4	0.1	500
5	0.4	500

diameter copper counter electrode and a Hg–Hg_2SO_4 reference electrode (MSE). All electrode potentials reported herein correspond to the MSE scale. During experiments, the working electrode was rotated using a Pine Instruments analytical rotator model AFASR at the three speeds given in Table 3.1.

The current–potential data were obtained from chronoamperometry experiments by applying potentials in the range of -0.4 to -0.8V and monitoring the current for 600s. Steady state was reached at all applied potentials by the end of this period. The electrochemical impedance spectra were obtained using the frequency response analyzer (FRA) module of the Autolab PGSTAT 10 system (Eco Chemie) in the potentiostatic mode. This mode yielded a more stable response than galvanostatic mode. The procedure followed was to hold the potential at the base value of -0.6V MSE for 200 seconds to reach steady state conditions prior to applying the EIS signal. Immediately thereafter, a sinusoidal wave with an amplitude of 6mV was applied over a frequency range from 65000 to 0.05Hz.

3.3 Model Development

In this section, the general kinetic and mass transport equations of the model are first presented. Then, the equations that correspond to the special case of copper electrodeposition are described. This is followed by the mathematical analysis to transform the system equations into the frequency domain, linearize resulting equations and obtain the dependence of the impedance on the frequency of the input sinusoidal wave.

3.3.1 General Equations

Several simplifying assumptions are made in developing the model: *i)* uniform current distribution over the rotating disk, *ii)* constant physical parameters such as diffusion coefficients and viscosity and *iii)* electroneutrality throughout the system. From the first assumption, mass transport occurs only in the direction normal to the electrode surface. Bulk conditions are considered to prevail in the solution beyond a distance 3δ from the electrode surface, where δ is given by [61]

$$\delta = 1.61 D_{min}^{1/3} \Omega^{-1/2} \nu^{1/6}. \tag{3.1}$$

where D_{min} is the minimum diffusivity, Ω is the rotational speed of the working electrode and ν is the kinematic viscosity of the solution. The following 1–D mass balance equation for species i within the boundary layer including contributions from diffusion, convection, migration and homogeneous reactions can be written:

$$\frac{\partial C_i}{\partial t} = D_i \frac{\partial^2 C_i}{\partial z^2} - \upsilon_z \frac{\partial C_i}{\partial z} + \frac{z_i D_i F}{RT} \frac{\partial}{\partial z} \left(C_i \frac{\partial \phi_{\mathrm{s}}}{\partial z} \right) + R_i, \ on\ 0 < z < 3\delta, \tag{3.2}$$

where C_i, D_i, z_i and R_i are the concentration, diffusivity, charge and generation rate by homogeneous reactions, respectively, of species i, ϕ_{s} is the potential within the electrolyte, F and R are the Faraday and gas constants and T is the electrolyte temperature. Second and higher order terms in the series expansion of the normal velocity component υ_z for a RDE are neglected to yield [80]:

$$\upsilon_z = -0.51023\, \Omega^{\frac{3}{2}} \nu^{-\frac{1}{2}} z^2. \tag{3.3}$$

In the case of a multi–component system, a mass balance given by Eq. (3.2) is written for each species and then solved in conjunction with the electroneutrality condition written as:

$$\Sigma z_i C_i = 0. \tag{3.4}$$

The electroneutrality condition and the migration and homogeneous reaction terms in Eq. (3.2) couple the transport equations together.

The conditions at the bulk boundary are:

$$C_i = C_i^{\mathrm{b}} \qquad at \quad z = 3\delta, \tag{3.5}$$

$$\phi_{\mathrm{s}} = 0 \qquad at \quad z = 3\delta. \tag{3.6}$$

where the superscript b in C_i denotes bulk conditions.

If species i participates in an electrode reaction proceeding at a current density i_f, then the boundary condition at the electrode surface is given by

$$D_i \frac{\partial C_i}{\partial z} + \frac{z_i D_i F}{RT} C_i \frac{\partial \phi_{\mathrm{s}}}{\partial z} = -\frac{i_{\mathrm{f}}}{n_i F} \qquad at \quad z = 0. \tag{3.7}$$

where n_i is the ratio of the stoichiometric coefficient of the electron to that of species i in the electrode reaction. If the species does not participate in an electrode reaction, then the following condition applies:

$$D_i \frac{\partial C_i}{\partial z} + \frac{z_i D_i F}{RT} C_i \frac{\partial \phi_{\mathrm{s}}}{\partial z} = 0 \qquad at \quad z = 0, \tag{3.8}$$

The total current density applied or measured in the system is made up of the faradaic i_{f} and double layer i_{dl} components, *i.e.*, ,

$$i = i_{\mathrm{f}} + i_{\mathrm{dl}} = i_{\mathrm{f}} + C_{\mathrm{dl}} \frac{\partial E'}{\partial t}, \tag{3.9}$$

where C_{dl} is the double layer capacitance and E' is the electrode potential corrected for the solution resistance R_{s} as follows:

$$E' = E - iR_{\mathrm{s}}. \tag{3.10}$$

3.3.2 Application to Cu^{2+} Reduction

The EIS analysis is applied to the case of copper deposition from acidic sulphate solutions. As mentioned in Section 2.4.2, hydrogen evolution can occur at the cathode as a secondary reaction during copper deposition. However, since cathodic polarization during the experiments of this study on which the model is based is never large enough for H^+ reduction to occur, H_2 evolution is not included in the model. Copper deposition is generally considered to occur via two consecutive one-electron transfer steps [28, 35, 36, 64, 74, 76–78], *i.e.*,

$$Cu^{2+}_{(\mathrm{aq})} + e^- \underset{k_{-1}}{\overset{k_1}{\rightleftharpoons}} Cu(I), \tag{3.11}$$

$$Cu(I) + e^- \underset{k_{-2}}{\overset{k_2}{\rightleftharpoons}} Cu^0_{(\mathrm{s})}. \tag{3.12}$$

In this model, the intermediate $Cu(I)$ is assumed to be adsorbed on the surface. The generation of very small amounts of $Cu(I)$ in solution has been reported in deoxygenated solutions at low cathodic overpotentials on the basis of rotating ring-disc electrode measurements [81–84]. The experiments of this chapter are conducted in a well–stirred solution, with no precautions to eliminate oxygen from solution and generally at potentials well below the open–circuit value. For these conditions, Barkey *et al.* [85] and Hua and Barkey [86] have shown that all $Cu(I)$ should be confined to the electrode surface.

The forward and backward rates of reactions (3.11) and (3.12) are given in terms of the Cu^{2+} surface concentration $C_1^s = C_1(0,t)$ and the fractional coverage θ of $Cu(I)$ on the electrode surface:

$$r_1 = k_1 \exp\left(-\beta_1 \frac{FE'}{RT}\right) C_1^{\mathrm{s}}(1-\theta_{Cu}), \tag{3.13}$$

$$r_{-1} = k_{-1} \exp\left((1-\beta_1) \frac{FE'}{RT}\right) \theta_{Cu}, \tag{3.14}$$

$$r_2 = k_2 \exp\left(-\beta_2 \frac{FE'}{RT}\right) \theta_{Cu}, \tag{3.15}$$

$$r_{-2} = k_{-2} \exp\left((1-\beta_2) \frac{FE'}{RT}\right) (1-\theta_{Cu}), \tag{3.16}$$

where β_1 and β_2 are the charge transfer coefficients for steps 1 and 2, respectively, and k_1, k_{-1}, k_2 and k_{-2} are rate constants independent of the electrolyte concentration. Although reaction (3.11) is the slow step under typical steady state plating conditions [76, 87, 88], no assumption is made regarding the controlling step under the transient conditions during EIS experiments. Thus, the faradaic current density is related to the reaction rates as follows:

$$i_{\mathrm{f}} = -F(r_1 - r_{-1} + r_2 - r_{-2}). \tag{3.17}$$

The balance of sites on the electrode surface that are occupied by adsorbed $Cu(I)$ ions is given by:

$$\Gamma \frac{\partial \theta}{\partial t} = r_1 - r_{-1} - r_2 + r_{-2}, \tag{3.18}$$

where Γ denotes the maximum adsorption density of a monolayer of $Cu(I)$ on the surface.

Based on the solution thermodynamics of the system, the following dissolved species are considered: Cu^{2+} (species 1), H^+ (species 2), SO_4^{2-} (species 3), cupric sulfate ion–pair $CuSO_{4\mathrm{(aq)}}$ (species 4) and bisulfate ion HSO_4^- (species 5) [89]. Thus, the following two homogeneous reactions occur everywhere within the boundary layer and bulk regions

$$CuSO_{4\text{(aq)}} \overset{K'}{\rightleftharpoons} Cu^{2+}_{\text{(aq)}} + SO^{2-}_{4\text{(aq)}}, \tag{3.19}$$

$$HSO^{-}_{4\text{(aq)}} \overset{K"}{\rightleftharpoons} H^{+}_{\text{(aq)}} + SO^{2-}_{4\text{(aq)}}, \tag{3.20}$$

Reactions (3.19) and (3.20) are assumed to proceed much more rapidly than the electrode reactions and mass transport so that they are considered to be at pseudo-equilibrium and the following conditions to apply everywhere within the system

$$K' = \frac{C_1 C_3}{C_4}, \tag{3.21}$$

$$K" = \frac{C_2 C_3}{C_5}. \tag{3.22}$$

From reactions (3.19) and (3.20), the following stoichiometric relations between the homogeneous rates of generation R_i of species i are obtained:

$$R_1 = -R_4, \tag{3.23}$$

$$R_2 = -R_5, \tag{3.24}$$

$$R_3 = -(R_4 + R_5). \tag{3.25}$$

Since there are no explicit expressions for R_i, the transport equations for the five species in solution given by Eq. (3.2) are combined in order to eliminate the R_i terms. In this way, the five transport equations for the individual species are transformed into three combined expressions. Eqs. (3.21) and (3.22) are then used as the remaining two equations required to solve the system.

3.3.3 Linearization

The input signal E(t) in an EIS experiment in potentiostatic mode can be written as

$$E(t) = \overline{E} + E_a \sin(\omega t), \tag{3.26}$$

where $\overline{E}$ is the applied base potential, E_a is the perturbation amplitude and ω is the frequency. Eq. (3.26) can be converted to the exponential form

$$E(t) = \overline{E} + \text{Re}\left\{\widetilde{E} \exp(\text{j}\omega t)\right\}, \tag{3.27}$$

where j is the imaginary unit ($\sqrt{-1}$) and the phasor $\widetilde{E}$ of the input signal is related to the amplitude of the perturbation as follows:

$$\widetilde{E} = E_a \exp\left(-\mathrm{j}\pi/2\right). \tag{3.28}$$

Since a small amplitude sinusoidal wave is applied to the system during the EIS technique, the system behaves pseudo–linearly. This allows second and higher order terms in the solution for each time–dependent variable y(t) to be eliminated and the solution to have the following form:

$$y(t) = \overline{y} + \mathrm{Re}\left\{\widetilde{y}\exp\left(\mathrm{j}\omega t\right)\right\}. \tag{3.29}$$

The first term $\overline{y}$ on the right hand side of Eq. (3.29) is the steady state part of the response, while the second term accounts for its transient component. The phasor of a response variable depends on its amplitude y_a and phase shift φ_y as follows:

$$\widetilde{y} = y_a \exp\left(\mathrm{j}\varphi_y - \mathrm{j}\pi/2\right). \tag{3.30}$$

The procedure to linearize and obtain expressions to determine the impedance is similar to that used to solve regular perturbation problems. It begins with the substitution of Eqs. (3.27) and (3.29) into the system of equations defined by the mass balances, electroneutrality condition, equilibrium relations and boundary conditions, *i.e.*, Eqs. (3.2)–(3.10), (3.13)–(3.18), (3.21) and (3.22). After expansion and simplification, each term in the resulting equations contains the factor $\exp(\mathrm{nj}\omega t)$ where n can be $0, 1$ or 2. All higher order terms containing $\exp(2\mathrm{j}\omega t)$ are eliminated. This leaves the system as a set of differential and algebraic equations, each of which has the general form

$$f_0(z) + f_1(z,\omega)\exp(\mathrm{j}\omega t) = 0, \tag{3.31}$$

where all the zeroth and first order terms are combined together as $f_0(z)$ and $f_1(z,\omega)$, respectively. In order for the solution for Eq. (3.31) to be guaranteed for all values of z and t, both of the following conditions must hold:

$$f_0(z) = 0, \tag{3.32}$$

$$f_1(z,\omega) = 0. \tag{3.33}$$

An important consequence of this procedure is that the original problem has been transformed from the time to frequency domain and to a system of algebraic and ordinary differential equations with respect to the coordinate z. The zeroth order problem defined by the complete set of equations given by Eq. (3.32) is solved first. This set of equations is nonlinear and describes the system under steady state conditions. The problem comprised of the remaining first order terms is solved next. This set of equations describes the transient condition of the system and becomes linear once the steady state solution is known. The mathematical details of the derivation of the zeroth and first order problems for the $CuSO_4$-H_2SO_4 system are given in Appendix A.

The five individual zeroth order mass transport equations are combined to eliminate the R_i terms and yield

$$A_1 + A_4 = 0, \tag{3.34}$$

$$A_2 + A_5 = 0, \tag{3.35}$$

$$A_3 + A_4 + A_5 = 0, \tag{3.36}$$

where variable A_i is given by the following expression:

$$A_i = D_i \frac{\mathrm{d}^2 \overline{C}_i}{\mathrm{d}^2 z} - v_z \frac{\mathrm{d}\overline{C}_i}{\mathrm{d}z} + \frac{z_i D_i F}{RT} \frac{\mathrm{d}}{\mathrm{d}z}\left(\overline{C}_i \frac{\mathrm{d}\overline{\phi}_\mathrm{s}}{\mathrm{d}z}\right), \qquad i = 1, 2, .., 5. \tag{3.37}$$

The bar on top of the dependent variables denotes the steady state condition. Thus, the five individual mass transport equations are replaced by three combined mass transport equations. The remaining equations required to solve for the five $\overline{C}_i$ values and $\overline{\phi}_\mathrm{s}$ come from the electroneutrality condition and the equilibrium conditions for homogeneous reactions (3.19) and (3.20)

$$z_1\overline{C}_1 + z_2\overline{C}_2 + z_3\overline{C}_3 + z_5\overline{C}_5 = 0, \tag{3.38}$$

$$K' = \frac{\overline{C}_1\,\overline{C}_3}{\overline{C}_4}, \tag{3.39}$$

$$K" = \frac{\overline{C}_2\,\overline{C}_3}{\overline{C}_5}. \tag{3.40}$$

Eqs. (3.34)–(3.40) apply everywhere within the boundary layer region from $z = 0$ to $z = 3\delta$. Eqs. (3.38)–(3.40) also apply in the bulk solution. The conditions at the surface and bulk boundaries are:

$$\overline{C}_i = C_i^{\mathrm{b}} \qquad at \quad z = 3\delta, \tag{3.41}$$

$$\overline{\phi}_{\mathrm{s}} = 0 \qquad at \quad z = 3\delta, \tag{3.42}$$

$$\overline{N}_1^s + \overline{N}_4^s = \overline{r}_1 - \overline{r}_{-1} \qquad at \quad z = 0, \tag{3.43}$$

$$\overline{N}_2^s + \overline{N}_5^s = 0 \qquad at \quad z = 0, \tag{3.44}$$

$$\overline{N}_3^s + \overline{N}_4^s + \overline{N}_5^s = 0 \qquad at \quad z = 0, \tag{3.45}$$

where the bulk concentrations are calculated using Eqs. (3.38)–(3.40) and the surface flux $\overline{N}_i^s$ is given by the expression

$$\overline{N}_i^s = D_i \frac{\mathrm{d}\overline{C}_i}{\mathrm{d}z}\bigg|_{z=0} + \frac{z_i D_i F}{RT}\left(\overline{C}_i \frac{\mathrm{d}\overline{\phi}_{\mathrm{s}}}{\mathrm{d}z}\right)\bigg|_{z=0}, \qquad i = 1, 2, .., 5. \tag{3.46}$$

Note that υ_z is zero at z=0. Eq. (3.43) expresses the fact that dissolved copper is consumed at the electrode by the net rate of reaction (3.11), while Eqs. (3.44) and (3.45) indicate that no dissolved hydrogen- and sulphate-bearing species are consumed at the electrode. $\overline{r}_1$ and $\overline{r}_{-1}$ in Eq. (3.43) are calculated from (3.13) and (3.14) evaluated using $\overline{E}'$, $\overline{C}_1^s$, $\overline{i}$ and $\overline{\theta}_{Cu}$, *i.e.*,

$$\overline{E}' = E - \overline{i} R_{\mathrm{s}}, \tag{3.47}$$

$$\overline{i} = \overline{i}_{\mathrm{f}} = -2F\left(\overline{r}_1 - \overline{r}_{-1}\right), \tag{3.48}$$

$$\overline{\theta}_{Cu} = \frac{k_1' \overline{C}_1^{\mathrm{s}} + k_{-2}'}{k_1' \overline{C}_1^{\mathrm{s}} + k_{-1}' + k_2' + k_{-2}'}, \tag{3.49}$$

where

$$k_1' = k_1 \mathrm{exp}\left(-\beta_1 \frac{F\overline{E}'}{RT}\right), \tag{3.50}$$

$$k_{-1}' = k_{-1} \mathrm{exp}\left((1-\beta_1)\frac{F\overline{E}'}{RT}\right), \tag{3.51}$$

$$k_2' = k_2 \mathrm{exp}\left(-\beta_2 \frac{F\overline{E}'}{RT}\right), \tag{3.52}$$

$$k_{-2}' = k_{-2} \mathrm{exp}\left((1-\beta_2)\frac{F\overline{E}'}{RT}\right). \tag{3.53}$$

Eq. (3.49) is obtained by setting the left-hand sice of Eq. (3.18) to zero.

The first–order problem derived as Eqs. (A.12)–(A.14) and (A.18)–(A.20) in Appendix A is given below and solved to yield the transient response:

$$j\omega\widetilde{C}_1 + j\omega\widetilde{C}_4 = B_1 + B_4, \tag{3.54}$$

$$j\omega\widetilde{C}_2 + j\omega\widetilde{C}_5 = B_2 + B_5, \tag{3.55}$$

$$j\omega\widetilde{C}_3 + j\omega\widetilde{C}_4 + j\omega\widetilde{C}_5 = B_3 + B_4 + B_5, \tag{3.56}$$

$$z_1\widetilde{C}_1 + z_2\widetilde{C}_2 + z_3\widetilde{C}_3 + z_5\widetilde{C}_5 = 0, \tag{3.57}$$

$$K' = \frac{\overline{C}_1\widetilde{C}_3 + \widetilde{C}_1\overline{C}_3}{\widetilde{C}_4}, \tag{3.58}$$

$$K" = \frac{\overline{C}_2\widetilde{C}_3 + \widetilde{C}_2\overline{C}_3}{\widetilde{C}_5}. \tag{3.59}$$

The function B_i in Eqs. (3.54)–(3.56) is given by

$$B_i = D_i\frac{\mathrm{d}^2\widetilde{C}_i}{\mathrm{d}^2 z} - \upsilon_z\frac{\mathrm{d}\widetilde{C}_i}{\mathrm{d}z} + \frac{z_iD_iF}{RT}\frac{\mathrm{d}}{\mathrm{d}z}\left(\overline{C}_i\frac{\mathrm{d}\widetilde{\phi}_\mathrm{s}}{\mathrm{d}z} + \widetilde{C}_i\frac{\mathrm{d}\overline{\phi}_\mathrm{s}}{\mathrm{d}z}\right),\ i = 1, 2, .., 5. \tag{3.60}$$

The conditions at the surface and bulk boundaries obtained as Eqs. (A.31)–(A.35) in Appendix A are:

$$\widetilde{C}_i = 0 \qquad at \quad z = 3\delta, \tag{3.61}$$

$$\widetilde{\phi}_\mathrm{s} = 0 \qquad at \quad z = 3\delta, \tag{3.62}$$

$$\widetilde{N}_1^s + \widetilde{N}_4^s = \widetilde{r}_1 - \widetilde{r}_{-1} \qquad at \quad z = 0, \tag{3.63}$$

$$\widetilde{N}_2^s + \widetilde{N}_5^s = 0 \qquad at \quad z = 0, \tag{3.64}$$

$$\widetilde{N}_3^s + \widetilde{N}_4^s + \widetilde{N}_5^s = 0 \qquad at \quad z = 0, \tag{3.65}$$

where

$$\widetilde{N}_i^s = D_i\frac{\mathrm{d}\widetilde{C}_i}{\mathrm{d}z}\bigg|_{z=0} + \frac{z_iD_iF}{RT}\left(\overline{C}_i\frac{\mathrm{d}\widetilde{\phi}_\mathrm{s}}{\mathrm{d}z} + \widetilde{C}_i\frac{\mathrm{d}\overline{\phi}_\mathrm{s}}{\mathrm{d}z}\right)\bigg|_{z=0}, \quad i = 1, 2, .., 5, \tag{3.66}$$

$$\begin{aligned}\widetilde{r}_1 = &\left[-\beta_1\frac{F}{RT}k_1\exp\left(-\beta_1\frac{F\overline{E}'}{RT}\right)\overline{C}_1^\mathrm{s}(1-\overline{\theta}_{Cu})\right]\widetilde{E}'\\ &+\left[k_1\exp\left(-\beta_1\frac{F\overline{E}'}{RT}\right)(1-\overline{\theta}_{Cu})\right]\widetilde{C}_1^\mathrm{s}\\ &-\left[k_1\exp\left(-\beta_1\frac{F\overline{E}'}{RT}\right)\overline{C}_1^\mathrm{s}\right]\widetilde{\theta}_{Cu},\end{aligned} \tag{3.67}$$

$$
\begin{aligned}
\widetilde{r}_{-1} = {} & \left[(1-\beta_1)\frac{F}{RT}k_{-1}\exp\left((1-\beta_1)\frac{F\overline{E}'}{RT}\right)\overline{\theta}_{Cu}\right]\widetilde{E}' \\
& + \left[k_{-1}\exp\left((1-\beta_1)\frac{F\overline{E}'}{RT}\right)\right]\widetilde{\theta}_{Cu},
\end{aligned}
\tag{3.68}
$$

$$
\begin{aligned}
\widetilde{r}_{2} = {} & \left[-\beta_2\frac{F}{RT}k_{2}\exp\left(-\beta_2\frac{F\overline{E}'}{RT}\right)\overline{\theta}_{Cu}\right]\widetilde{E}' \\
& + \left[k_{2}\exp\left(-\beta_2\frac{F\overline{E}'}{RT}\right)\right]\widetilde{\theta}_{Cu},
\end{aligned}
\tag{3.69}
$$

$$
\begin{aligned}
\widetilde{r}_{-2} = {} & \left[(1-\beta_2)\frac{F}{RT}k_{-2}\exp\left((1-\beta_2)\frac{F\overline{E}'}{RT}\right)(1-\overline{\theta}_{Cu})\right]\widetilde{E}' \\
& - \left[k_{-2}\exp\left((1-\beta_2)\frac{F\overline{E}'}{RT}\right)\right]\widetilde{\theta}_{Cu},
\end{aligned}
\tag{3.70}
$$

and

$$\Gamma\, j\, \omega\, \widetilde{\theta}_{Cu} = \widetilde{r}_1 - \widetilde{r}_{-1} - \widetilde{r}_2 + \widetilde{r}_{-2}, \tag{3.71}$$

$$\widetilde{E}' = \widetilde{E} - \widetilde{i}R_{\mathrm{s}}, \tag{3.72}$$

$$\widetilde{i} = \widetilde{i}_{\mathrm{f}} + \widetilde{i}_{\mathrm{dl}} = -F(\widetilde{r}_1 - \widetilde{r}_{-1} + \widetilde{r}_2 - \widetilde{r}_{-2}) + C_{\mathrm{dl}}\, j\, \omega\, \widetilde{E}'. \tag{3.73}$$

The solution of Eqs. (3.54)–(3.73) obtained at a specific frequency yields the concentration and electrolyte potential phasor profiles as well as the surface coverage, electrode potential and current density phasors. Due to the presence of the imaginary term j in the governing equations, the solutions for the phasors are complex. Once $\widetilde{E}$ and $\widetilde{i}$ are determined, they are used to calculate the impedance as a function of frequency based on its definition:

$$Z = \frac{\widetilde{E}}{\widetilde{i}}. \tag{3.74}$$

The impedance also has real and imaginary components.

3.3.4 Computational Implementation

Numerical solution of the zeroth and first order equations were carried out using the *bvp4c MATLAB* routine [90]. An initial mesh of 100 points in the boundary layer was provided. Afterwards, the number of points is internally adjusted to obtain a more accurate solution.

The *bvp4c* routine utilizes the orthogonal collocation method [91] and is capable of handling problems defined in terms of complex variables.

The values of seven physicochemical parameters (β_1, β_2, k_1, k_{-1}, k_2, k_{-2} and C_{dl}) were determined by fitting the model to experimental open–circuit voltage measurements and steady state current-potential and EIS responses for Cu^{2+} reduction. Obviously, only the zeroth order solution (*i.e.*, steady state model) was used for fitting of the open–circuit voltage measurements and steady–state polarization data. The solution of the zeroth order problem first and then the first order problem was required to evaluate the impedance and fit to the EIS data. Parameter estimation was carried out using the routine *lsqnonlin*. This routine consists of finding the parameter values that minimize the error or residual sum of squares (RSS) for a model that is nonlinear with respect to the parameters [92]. The routine *lsqnonlin* requires the specification of initial guesses for the parameters. Values of 0.5 were used for the charge transfer coefficients and the values used for rate constants and the double layer capacitance were chosen based on literature data. Default tolerances of 1×10^{-6} in the change of the residual sum of squares and the parameter estimates from one iteration to the next were used as the convergence criterion for all the data. The RSS for the polarization data is defined as

$$RSS = \sum_{j=1}^{N_{ss}} \left(i_j^{exp} - i_j^{mod} \right)^2 . \tag{3.75}$$

where N_{ss} is the total number of current–potential data points and the indices *exp* and *mod* denote the experimental and model responses at the j^{th} data point. Best results were obtained in the case of impedance data if the error between each measured value and the corresponding model value was weighted with respect to the measured value (*i.e.*, normalized). The RSS value for these data is defined as

$$RSS = \sum_{j=1}^{N_{tr}} \left[\left(\frac{Re\left\{ Z_j^{exp} - Z_j^{mod} \right\}}{Re\left\{ Z_j^{exp} \right\}} \right)^2 + \left(\frac{Im\left\{ Z_j^{exp} - Z_j^{mod} \right\}}{Im\left\{ Z_j^{exp} \right\}} \right)^2 \right] , \tag{3.76}$$

where N_{tr} is the total number of impedance measurements. The parameter search was constrained by specifying lower and upper bounds requested by the routine. Bounds of 0.35 and 0.65 were used for the charge transfer coefficients, while those for the rate constants were taken to be two orders of magnitude smaller and higher than the initial guesses.

The predicted steady state current-potential responses were obtained following the algorithm sketched in Fig. 3.1:

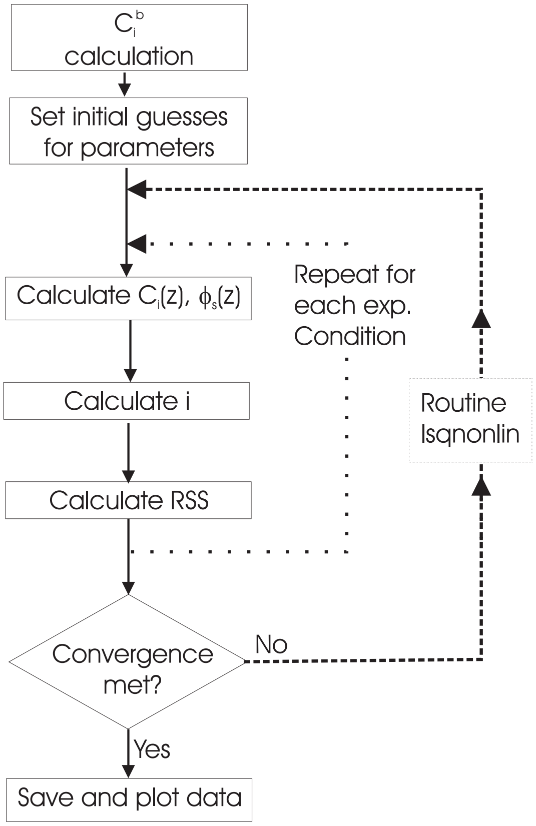

Figure 3.1: Algorithm used in the numerical solution and Matlab implementation of the model to fit to steady state data.

1. The bulk concentrations are calculated by solving Eqs. (3.38)–(3.40) simultaneously.
2. Parameters β_1, β_2, k_1, k_{-1}, k_2 and k_{-2} are set to their initial guesses.
3. For each potential, the concentrations and solution potential are obtained using Eqs. (3.13)–(3.16), (3.34)–(3.49) and the *bvp4c* routine.
4. The steady state current densities are obtained at each potential using the calculated concentrations and Eqs. (3.13)–(3.16), (3.48) and (3.49).
5. The residual sum of squares is calculated using Eq. (3.75).

6. Steps 3 to 5 are repeated for each experimental condition.

7. The *lsqnonlin* routine obtains a new set of parameter estimates and steps 3 to 6 are re–done. This procedure is repeated until the change in either the total error pooled over all the steady state measurements or the parameter values meets the convergence criterion. The procedure is also terminated when the maximum number of iterations is reached.

8. Finally, the experimental data and model–fitted values are plotted.

The algorithm in Fig. 3.2 illustrates the steps followed in the fitting of the model to the impedance spectra:

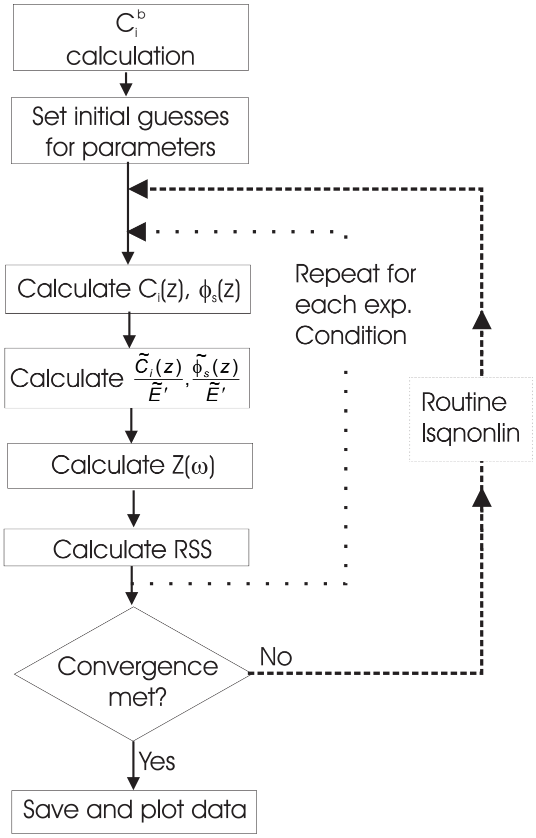

Figure 3.2: Algorithm used in the numerical solution and Matlab implementation of the model to fit to impedance data.

1. The bulk concentrations are calculated by solving Eqs. (3.38)–(3.40) simultaneously.

2. Parameters β_1, β_2, k_1, k_{-1}, k_2, k_{-2} and C_{dl} are set to their initial guesses.

3. The steady state equations are solved to obtain the concentrations and solution potential as in step 3 of the algorithm in Fig.3.1.

4. For each frequency, the concentration and solution potential phasors are obtained by solving the first order equations of the transient model and using the concentrations and solution potential calculated in step 3. In order to reduce the number of phasor variables to be solved, Eqs. (3.54)–(3.71) are divided by $\widetilde{E'}$ and solved to obtain the phasor ratios $\frac{\widetilde{C_i}}{\widetilde{E'}}$ and $\frac{\widetilde{\phi_{\mathrm{s}}}}{\widetilde{E'}}$ using the *bvp4c* routine.

5. After substitution of Eqs. (3.72) and (3.73) into (3.74), the following expression is obtained for the impedance

$$\begin{aligned} Z =& \frac{\widetilde{E}}{\widetilde{i}} = \frac{\widetilde{E'} + \widetilde{i} R_{\mathrm{s}}}{\widetilde{i}} = \frac{\widetilde{E'}}{-F(\widetilde{r}_1 - \widetilde{r}_{-1} + \widetilde{r}_2 - \widetilde{r}_{-2}) + C_{\mathrm{dl}}\, j\, \omega\, \widetilde{E'}} + R_{\mathrm{s}}, \\ =& \frac{1}{\frac{-F(\widetilde{r}_1 - \widetilde{r}_{-1} + \widetilde{r}_2 - \widetilde{r}_{-2})}{\widetilde{E'}} + C_{\mathrm{dl}}\, j\, \omega} + R_{\mathrm{s}} = \frac{1}{\frac{1}{Z_f} + C_{\mathrm{dl}}\, j\, \omega} + R_{\mathrm{s}}, \end{aligned} \tag{3.77}$$

   where Z_f is the faradaic impedance. Then, the impedance at each frequency is calculated from Eq. (3.77) and Eqs. (3.67)–(3.71) after they are divided by $\widetilde{E'}$.

6. The residual sum of squares is calculated using Eq. (3.76).

7. Steps 3 to 6 are repeated for each experimental condition.

8. The *lsqnonlin* routine obtains a new set of parameter estimates and steps 3 to 7 are re–done. This procedure is repeated until the change in either the total error pooled over all the impedance measurements or the parameter values meets the convergence criterion. The procedure is also terminated when the maximum number of iterations is reached.

9. Finally, the experimental data and model–fitted values are plotted.

Another aspect to be addressed was how to reconcile the fitting procedure and final parameter estimates obtained from the steady state polarization and impedance spectra. It turned out that this was dictated by their relative sensitivities to changes in parameter values, as discussed in the next section.

3.4 Results

3.4.1 Parameter Estimation

The parameters held constant throughout this analysis are given in Table 3.2. The diffusion coefficients for Cu^{2+} and $CuSO_4$ were assumed to be equal and obtained by fitting the mass transfer limiting current density from each of the five experiments shown in Table 3.1 to the Levich equation. This equation relates the limiting current density i_L to the metal ion diffusion coefficient D_i, rotation speed of the working electrode Ω, solution viscosity ν and bulk concentration of the metal ion C_i^b:

Table 3.2: Constant parameters used in the simulations.

Parameter	Value	Reference
D_1	4.8×10^{-6} cm^2 s^{-1}	this study
D_2	9.312×10^{-5} cm^2 s^{-1}	[93]
D_3	1.065×10^{-5} cm^2 s^{-1}	[93]
D_4	4.8×10^{-6} cm^2 s^{-1}	this study
D_5	1.33×10^{-5} cm^2 s^{-1}	[93]
ν	0.01 cm^2 s^{-1}	[35]
Γ	5.74×10^{-9} mol cm^{-2}	this study
R_s	0.47 ohm cm^2	this study
K'	4.3637×10^{-6} mol cm^{-3}	[89]
K"	1.05×10^{-5} mol cm^{-3}	[89]

$$i_L = 0.62nFD_i^{2/3}\Omega^{1/2}\nu^{-1/6}C_i^b, \tag{3.78}$$

where n is the number or electrons per mole of reduced species (n=2 for Cu^{2+} reduction reaction). The average value of $D_{Cu^{2+}}$ and D_{CuSO_4} determined from these experiments was 4.8×10^{-6} cm^2 s^{-1} and used in all subsequent modeling. The Γ value was estimated using the ionic radius of the cuprous ion [94]. The solution resistance was estimated to be 0.47 ohm cm^2 by extrapolating the high frequency loop of the Nyquist plot to the axis of the real impedance component. This value is in good agreement with that reported by Kelly and West [35] for a 0.24M $CuSO_4$ + 1.8M H_2SO_4 electrolyte.

As later explained in Section 3.4.3, it was found that the computed EIS response was more sensitive to changes in the parameters than was the steady state current–potential response. Hence, initial estimates of all parameters except the double layer capacitance were found by fitting the model first to the open–circuit potential measurements and steady state current–potential curves. The values of the two charge transfer coefficients and four rate constants so obtained were then used as the starting points for fitting the model to the impedance data.

The first approach was to attempt to reduce the number of fitting parameters by the additional constraint that the current density be zero at the equilibrium potential E_{eq} for Cu^{2+} reduction. This leads to an algebraic expression involving the four rate constants that allows one to be eliminated as a fitting parameter [72]. Unfortunately, this approach failed for two reasons. Firstly, after fitting the model to the data, a negative value is obtained for k_{-1} using the algebraic expression. Secondly and more fundamentally, it turns out that the key condition for the current density to be zero at E_{eq} for Cu^{2+} reduction is not met by this system. When the measurements are made, one observes that the open-circuit potential differs from E_{eq} for the Cu^{2+}/Cu reaction. A comparison of E_{eq} and the OCP measurements obtained from the experiments in this chapter is shown in Table 3.3.

Table 3.3: Comparison of experimental open circuit potentials and calculated equilibrium potentials using the model developed in Section 3.3.

Experiment	$[CuSO_4]$ mol L^{-1}	$[Cu^{2+}]$ mol L^{-1}	E_{eq} V(MSE)	OCP V(MSE)	OCP–E_{eq} V
1-3	0.25	0.070	-0.377	-0.406	-0.029
4	0.1	0.0289	-0.389	-0.417	-0.028
5	0.4	0.1087	-0.372	-0.402	-0.030

The values of $[Cu^{2+}]$ appearing in Table 3.3 are calculated from the model used in this chapter and are less than the $CuSO_4$ concentrations added to the solution since the presence of the $CuSO_4$ ion-pair in addition to Cu^{2+} is taken into account. In each case of Table 3.3, the measured OCP is 28-30 mV more negative than E_{eq}. This observation is not new for the $CuSO_4$-H_2SO_4 system and has been reported in the literature. Vereecken *et al.* [83] reported the OCP to be about 60 mV more negative than E_{eq}. In an earlier paper, Barkey *et al.* [85] conducted a detailed experimental and modeling study of this effect and found the OCP to always differ from E_{eq}. The conclusion from these studies is that in the presence of oxygen (as in this study) the copper electrode is not at equilibrium with respect to the Cu^{2+}/Cu reaction at the open-circuit potential. Barkey *et al.* [85] showed that their data could be fit by a model in which the OCP is given by a mixed potential between the Cu^{2+}/Cu^{+} redox couple and the Cu^{+}/Cu^{0} redox couple. Thus, the OCP is related more to the comproportionation reaction $Cu^0 + Cu^{2+} \rightleftarrows 2\ Cu^+$ than to the Cu^{2+}/Cu^0 reaction. However, once one begins to cathodically polarize the electrode and Cu^{2+} reduction occurs to any significant degree, the 2-step mechanism considered in this chapter (*i.e.*, reactions (3.11) and (3.12)) and numerous other studies is widely accepted. Since the primary interest of this study was the electrode response during Cu^{2+} reduction and the mathematical analysis and parameter estimation procedure was already difficult enough, a model combining the mixed potential mechanism proposed by Barkey *et al.* for conditions at or near the OCP with the standard 2-step mechanism for cathodic overpotentials was not considered. Instead, the 2-step mechanism was used and the constraint that the current go to zero when $E = E_{eq}$ for the Cu^{2+}/Cu^0 reaction was relaxed. Thus, the OCP was treated exactly as any other point on the current-potential and considered the four rate constants to be independent adjustable parameters [95].

When the *lsqnonlin* routine was then applied to the experimental data, it proceeded through the maximum number of iterations specified (500) without meeting the convergence criterion and obtaining an optimum solution. Examination of the confidence intervals of the individual parameters provided an explanation for the slow progress of the parameter estimation routine. The confidence intervals for k_{-1}, k_2 and k_{-2} were very large, indicating that the model was insensitive to these parameters. Such a result makes sense if one considers the previously reported behavior of Cu^{2+} reduction. All of the data under analysis were obtained from experiments conducted under cathodic conditions during Cu^{2+} reduction. At cathodic overpotentials, the rate of Cu^{2+} reduction is controlled by the forward direction of the first step only. Therefore, the rate constants associated with the other steps can vary over a relatively wide range and still not affect the predicted electrode response during cathodic polarization. One would expect the statistical analysis to lead to wide confidence intervals and insensitivity for k_{-1}, k_2 and k_{-2}. Thus, these statistical results are taken to be further confirmation of previous observations that the forward direction of reaction (3.11) is rate controlling. In order to obtain tighter estimates for k_{-1}, k_2 and k_{-2}, one would have to conduct EIS and chronoamperometry experiments under conditions where the electrode response is more strongly affected by them –for example, conditions of anodic polarization. However, this is beyond the scope of this study.

Consequently, the approach was changed to treat the insensitive parameters differently from the sensitive ones and use a two–stage fitting procedure for the impedance data. The first step was to fit for all seven parameters simultaneously to the EIS data using the parameter values obtained from the original fitting as the initial guesses, although the routine was now limited to only 10 iterations. Previous runs had shown that the RSS value no longer changed significantly after this number of iterations, although the convergence criterion was still not met. The second stage of the fitting involved keeping the insensitive parameters k_{-1}, k_2 and k_{-2} fixed at the values obtained from the first stage and then re–fitting the model to the EIS data for the remaining parameters β_1, β_2, k_1, and C_{dl}. This time the routine was found to converge to an optimum set of parameters. The final set of parameters so obtained is listed in Table 3.4. The model was also found to accurately fit the steady state current–potential data with this set of parameters.

Although the calculated impedance values were not sensitive to k_{-1}, k_2 and k_{-2}, they could not be eliminated altogether from the model since this would also lead to the elimi-

Table 3.4: Parameters obtained by least squares fitting of the model.

Parameter	Value [a]
β_1	0.475
β_2	0.423 ± 0.010
k_1	1.09×10^{-7} cm s^{-1}
k_{-1}	2.74×10^{-7} mol cm^{-2}s^{-1}
k_2	5.20×10^{-9} mol cm^{-2}s^{-1}
k_{-2}	6.08×10^{-2} mol cm^{-2}s^{-1}
C_{dl}	$(6.14\pm3.10)\times10^{-5}$ F cm^{-2}

[a] based on MSE scale

nation of β_2 which has a significant effect on both the impedance spectra and steady state current–potential curves. This was confirmed with simulations which showed the fit of the model to the experimental data suffered significantly when only the forward direction of the first step in Cu^{2+} reduction was considered. The confidence interval for k_2 obtained from the first fitting was found to include a value of zero, whereas the interval for k_{-2} did not include zero. However, it is physically impossible from the point of view of the reaction mechanism to include k_{-2} and the reverse direction of the second step without also including k_2 and the forward direction of the same step. Consequently, all terms in the reaction mechanism were included in subsequent calculations.

3.4.2 Statistical Analysis

The correlation coefficient ρ_{XY} for a pair of parameters X and Y is an indication of the linearity between them [96]. This coefficient was calculated for all parameter estimates using the residuals vector and Jacobian matrix generated from the output of the *lsqnonlin* routine as

$$\rho_{XY} = \frac{Cov(X,Y)}{\sqrt{Cov(X,X)\; Cov(Y,Y)}}. \tag{3.79}$$

The covariance matrix $Cov(X,Y)$ used in Eq. (3.79) was obtained as a linear approximation [96] from

$$Cov(X,Y) = (J'J)^{-1}\; s^2, \tag{3.80}$$

where J is the Jacobian matrix and s^2 is the variance defined as

$$s^2 = \frac{RSS}{N_{tr} - p}. \tag{3.81}$$

RSS is given by Eq. (3.76) and p is the total number of fitting parameters. The value of ρ_{XY} for β_1 and k_1 is close to 1.0, reflecting a high correlation between them. However, such behavior is not uncommon for parameters related by an exponential function such as that given by Eq. (3.13). The uncertainty in these parameters is represented by their joint confidence region (jcr) instead of an individual confidence interval for each parameter and can be obtained by a linear approximation of the inequality [96]:

$$(\alpha - \widehat{\alpha})'\; G^{-1}\; (\alpha - \widehat{\alpha}) \leq 2\; s^2 f_{2,N_{tr}-2,0.05}, \tag{3.82}$$

where α and $\widehat{\alpha}$ are the vectors containing the jcr contour points and the estimated parameters, respectively; G is a 2x2 matrix formed from elements of $(J'J)$ corresponding to the correlated parameters; $f_{2,N_{tr}-2,0.05}$ is a tabulated value for the f–distribution with 2 and N$_{tr}$-2 degrees of freedom at a 0.05 level of significance. This linear approximation can be considered to be exact in the neighborhood of the values estimated for the parameters. A plot of the joint confidence region is presented in Fig. 3.3. The individual confidence intervals for β_2 and $C_{\rm dl}$ which were not significantly correlated with other parameters are included in Table 3.4. Confidence intervals for k_{-1}, k_2 and k_{-2} were not obtained due to the insensitivity of the model to their values for the experimental conditions of this study.

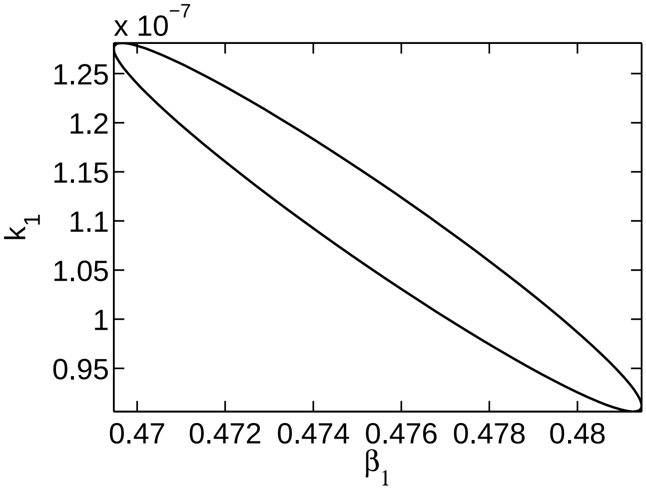

Figure 3.3: Linear approximation of the joint confidence region for the estimates of β_1 and k_1.

In Fig. 3.4, a comparison of the fitted current–potential curves and Nyquist plots to the measured ones is shown for the five experimental conditions in Table 3.1. The agreement is very good for the steady state current–potential data, but less so for the impedance measurements. There is some discrepancy in the diameter and/or height of either semi–circle in most of the cases. Another important observation regarding Figs. 3.4b, d, f, h and j is that the fitted values tend to lie above the measured values over consecutive frequencies in some regions of the spectra, and underestimate the experimental data over consecutive frequencies in other regions. This observation suggests the possibility of some correlation between model errors.

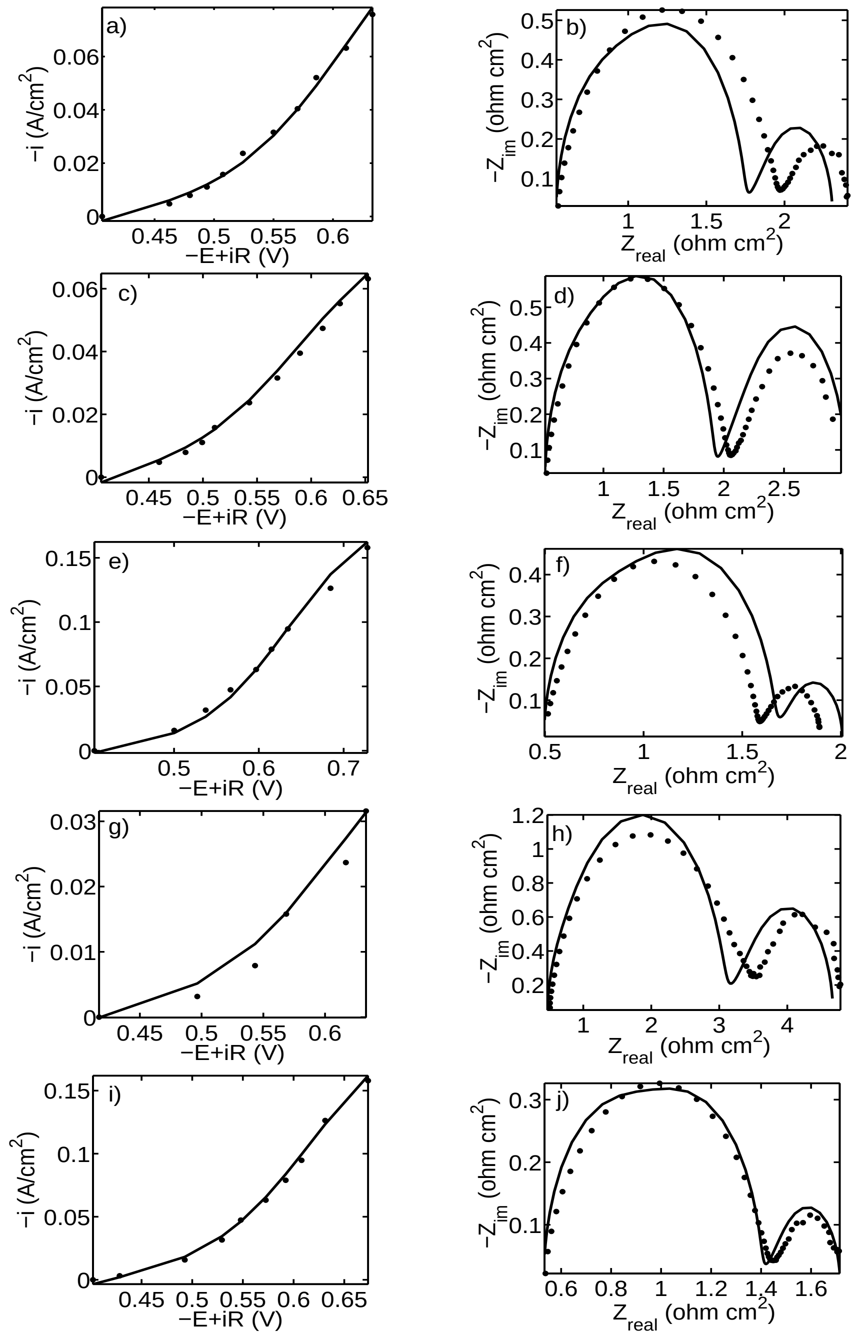

Figure 3.4: Least squares fit of the model (solid line) to steady state current–potential and EIS Nyquist plots (dotted lines) obtained for (a) and (b) Experiment 1, (c) and (d) Experiment 2, (e) and (f) Experiment 3, (g) and (h) Experiment 4, and (i) and (j) Experiment 5.

To investigate the possibility of residual correlation, an analysis of the model residuals was conducted. The residuals are plotted in two different ways in Figs. 3.5 and 3.6. The residuals of the real (Fig. 3.5*a*, *c*, *e*, *g* and *i*) and imaginary (Fig. 3.5*b*, *d*, *f*, *h* and *j*) components of the impedance are plotted first as a time series in the order n in which they were measured. Residuals are also plotted in lag plots where the error (z_{n-1}) at a given frequency is plotted versus the corresponding one (z_n) at the following frequency for the real (Fig. 3.6*a*, *c*, *e*, *g* and *i*) and imaginary (Fig. 3.6*b*, *d*, *f*, *h* and *j*) components. Both types of plots, especially the time series, show a non–scattered pattern, suggesting that the residuals could be correlated or the function used in the optimization is not adequate [97]. In order to determine if the residuals are correlated, their autocorrelation function f_k was evaluated as follows:

$$f_k = \sum_{n=k+1}^{N_{tr}} \frac{z_n z_{n-k}}{N s_e^2}, \tag{3.83}$$

where s_e^2 is given by

$$s_e^2 = \frac{1}{N_{tr}} \sum_{n=1}^{N_{tr}} z_n^2. \tag{3.84}$$

The residual autocorrelation functions for the real and imaginary components are plotted in Fig. 3.7. Also included in the plots are horizontal lines for the 95% confidence bounds on f_k, calculated as $\pm 2/\sqrt{N_{tr}}$. The autocorrelation functions for the real and imaginary component residuals do not lie within the bounds for $k > 2$ and tend to decay slowly, indicating that correlation between residuals exists. A previous study of the error structure of impedance data fitting provides some insights into possible causes for correlation [98–100]. The error between fitted and experimental data can be attributed to the use of an inadequate model, non-stationary behavior, instrumental influences, noise, *etc.* Non-stationary behavior due, for example, to changes to the electrode surface is commonly found in systems such as the one treated in this chapter, particularly in the regions of low frequencies. Non-stationary effects can be identified by using the Kramers-Kronig relations. The experimental results presented in this work were analyzed using the Kramers-Kronig test available on the commercial FRA module. However, the results of this analysis were inconclusive, particularly since the noise error was unknown.

An effort was made to determine if the fitting could be improved by removing the residual correlation. One approach to remove this correlation is to modify the model as a

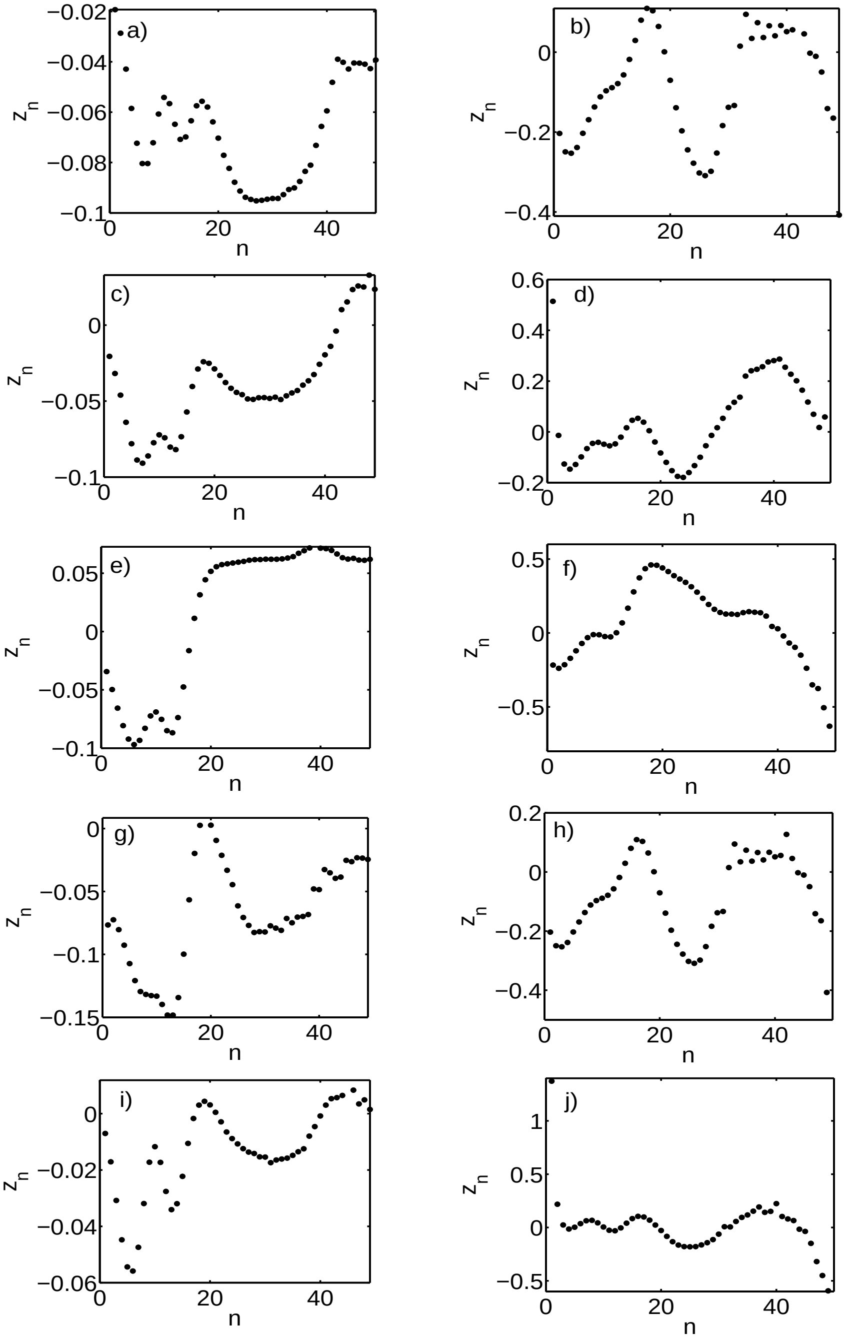

Figure 3.5: Time series plots of the residuals for the (a), (c), (e), (g) and (i) real and (b), (d), (f), (h) and (j) imaginary components of the impedance for (a) and (b) Experiment 1, (c) and (d) Experiment 2, (e) and (f) Experiment 3, (g) and (h) Experiment 4 and (i) and (j) Experiment 5.

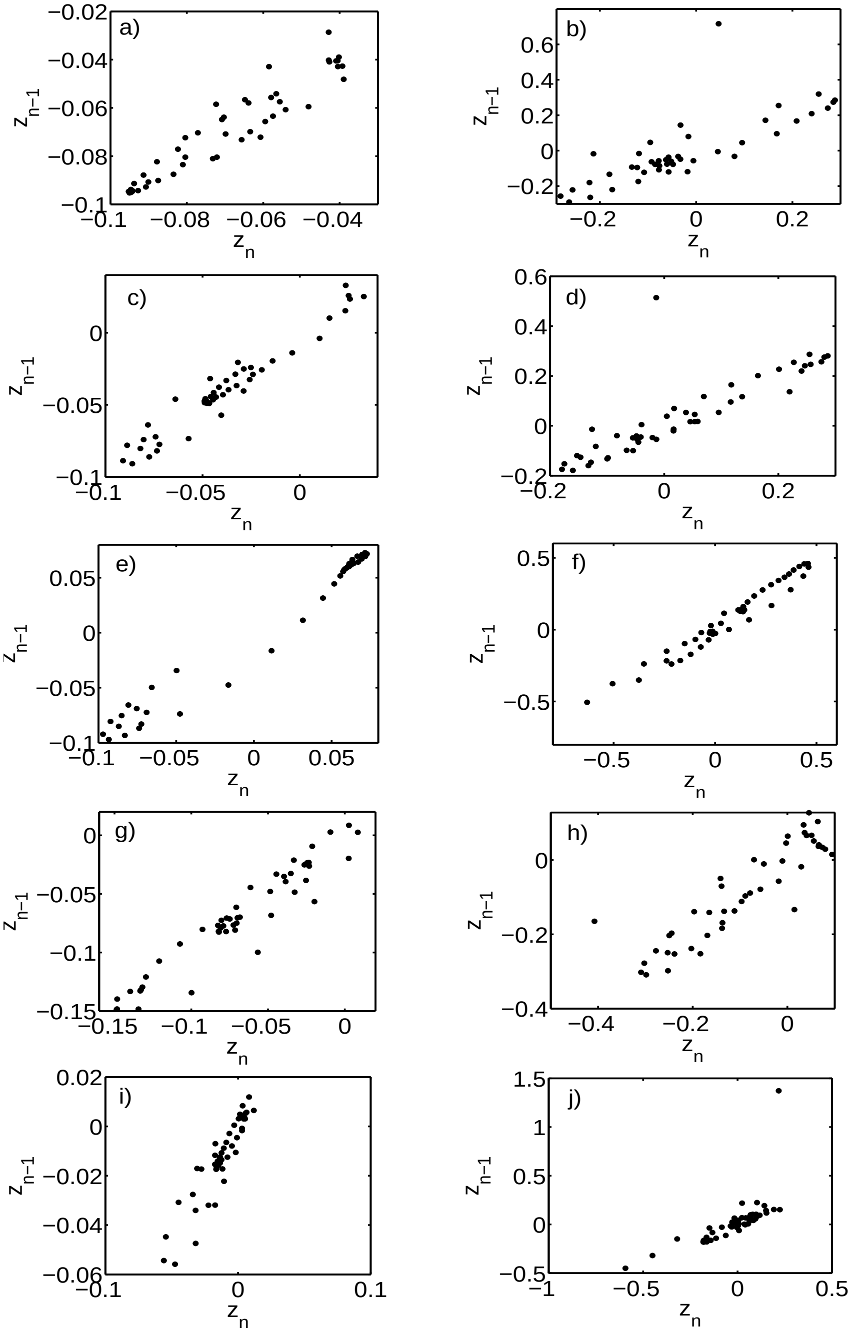

Figure 3.6: Lag plots of the residuals for the (a), (c), (e), (g) and (i) real and (b), (d), (f), (h) and (j) imaginary components of the impedance for (a) and (b) Experiment 1, (c) and (d) Experiment 2, (e) and (f) Experiment 3, (g) and (h) Experiment 4 and (i) and (j) Experiment 5.

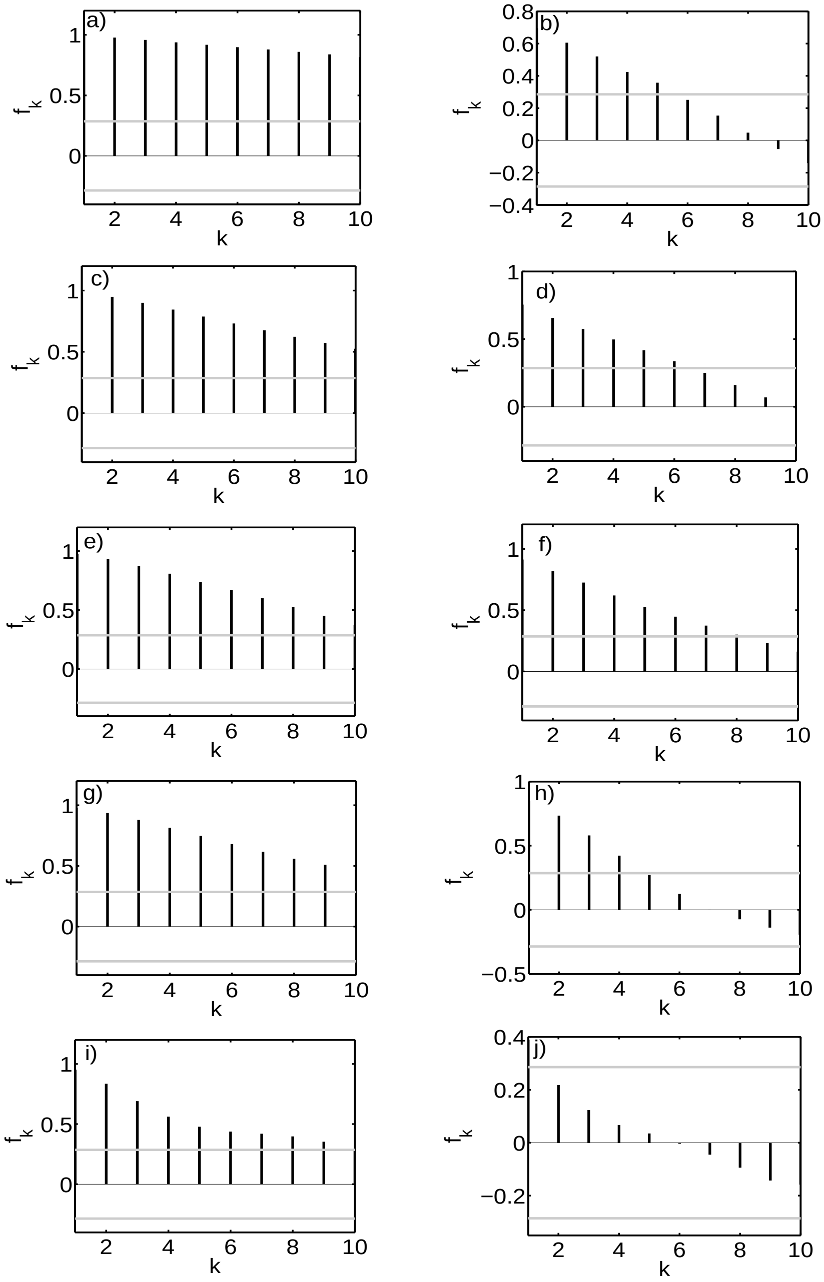

Figure 3.7: Residual autocorrelation function plotted for the (a), (c), (e), (g) and (i) real and (b), (d), (f), (h) and (j) imaginary components of the impedance for (a) and (b) Experiment 1, (c) and (d) Experiment 2, (e) and (f) Experiment 3, (g) and (h) Experiment 4 and (i) and (j) Experiment 5. Grey horizontal lines enclose the 95% confidence region for f_k.

first–order autoregressive process [97] and then re–fit this new model to the experimental data. The new model takes the form

$$Z_n^{mod}(\omega) = \widehat{Z}_n^{mod}(\omega) + \lambda z_{n-1}, \tag{3.85}$$

where $\widehat{Z}_n^{mod}$ denotes the impedance calculated for the n^{th} frequency using the original linearized model described previously (see § 3.3.3), λ is a constant parameter that accounts for the linear dependence between two consecutive residuals in the original model and z_{n-1} is the residual calculated from the original model at the $n-1^{th}$ frequency. The use of Eq. (3.85) involves the introduction of a new parameter λ to be estimated. The parameters obtained by the previous fitting procedure and given in Table 3.4 were used as initial guesses for the kinetic parameters and the fitting procedure was repeated using the measured impedance data. Values for the insensitive parameters were not allowed to vary in the re–fitting procedure. The new values estimated for the parameters in the least squares fitting to eliminate the residual dependency are shown in Table 3.5. Comparison of Tables 3.4 and 3.5 indicates that neither β_1, β_2 nor k_1 changed significantly, whereas C_{dl} increased by about 25%. The high correlation found with the original model for β_1 and k_1 still exists in this model. In this case, a nonlinear joint confidence region was calculated

Table 3.5: Parameters obtained by least squares fitting of the corrected model accounting for residual correlation.

Parameter	Value [a]
β_1	0.479
β_2	0.422±0.014
k_1	1.09×10^{-7} cm s^{-1}
k_{-1}	2.74×10^{-7} mol cm^{-2}s^{-1}
k_2	5.20×10^{-9} mol cm^{-2}s^{-1}
k_{-2}	6.08×10^{-2} mol cm^{-2}s^{-1}
C_{dl}	$(7.67\pm4.26)\times10^{-5}$ F cm^{-2}
λ	0.85±0.050

[a] based on MSE scale

for these two parameters [96] using the inequality

$$RSS \leq RSS_p \left(1 + \frac{2}{N_{tr} - 2} f_{2,N_{tr}-2,0.05}\right), \tag{3.86}$$

where RSS and RSS_p are the residual sum of squares calculated with Eq. (3.76) for the jcr contour points and the parameter estimates, respectively. The resulting nonlinear jcr for β_1 and k_1 shown in Fig. 3.8 was obtained by solving Eq. (3.86) to obtain the range of β_1 for prescribed values of k_1.

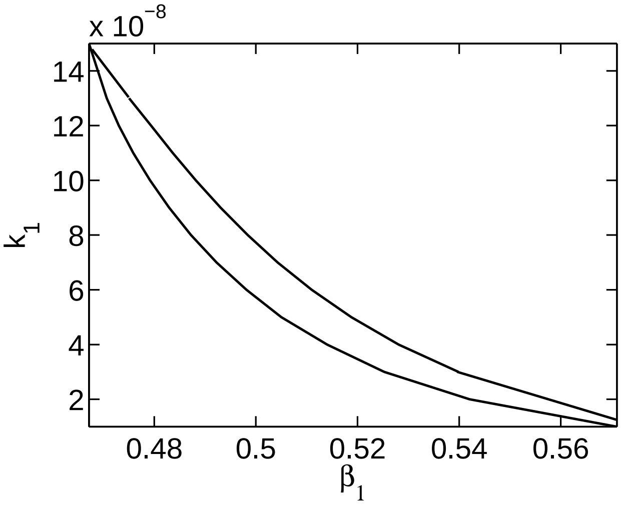

Figure 3.8: Joint confidence region for the estimates of β_1 and k_1 in the corrected model.

Very good agreement between the computed and the experimental data can be observed in Fig. 3.9. Comparison with Fig. 3.4 shows that the fit to the impedance spectra, particularly the low frequency loop, has improved significantly. Moreover, the residual sum of squares combined for all five experimental conditions decreased from 12 to 4 with the new model. A significant improvement is also observed in the autocorrelation function plot (Fig. 3.10) after accounting for the residual dependency, especially for the imaginary component. Some residual correlation in the real component of the impedance is still observed. To determine if the fitting could be further improved, the use of a second–order autoregressive process was also attempted:

$$Z_n^{mod}(\omega) = \widehat{Z}_n^{mod}(\omega) + \lambda_1 z_{n-1} + \lambda_2 z_{n-2}. \tag{3.87}$$

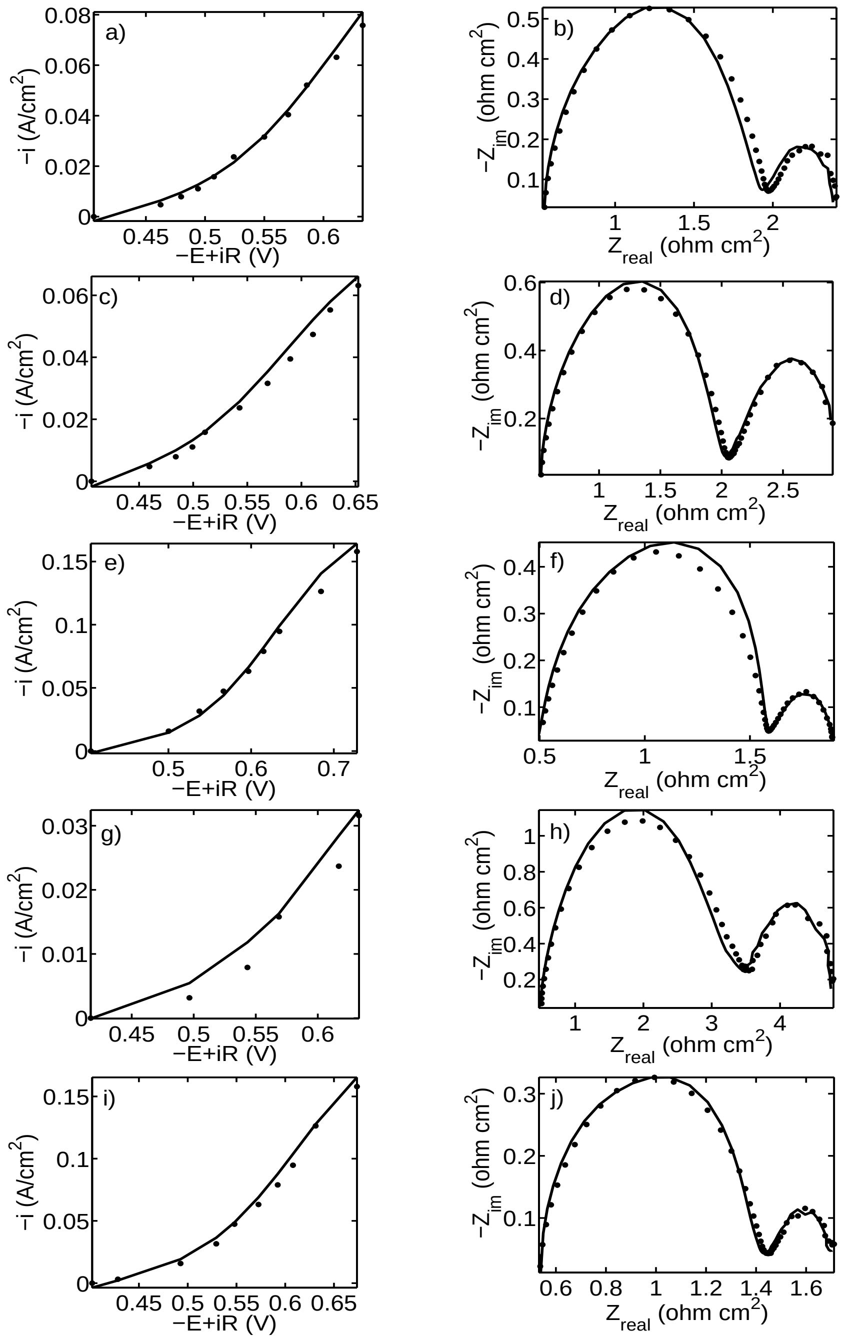

Figure 3.9: Least squares fit of the corrected model (solid line) to steady state current–potential and EIS Nyquist plots (dotted lines) obtained for (a) and (b) Experiment 1, (c) and (d) Experiment 2, (e) and (f) Experiment 3, (g) and (h) Experiment 4, and (i) and (j) Experiment 5.

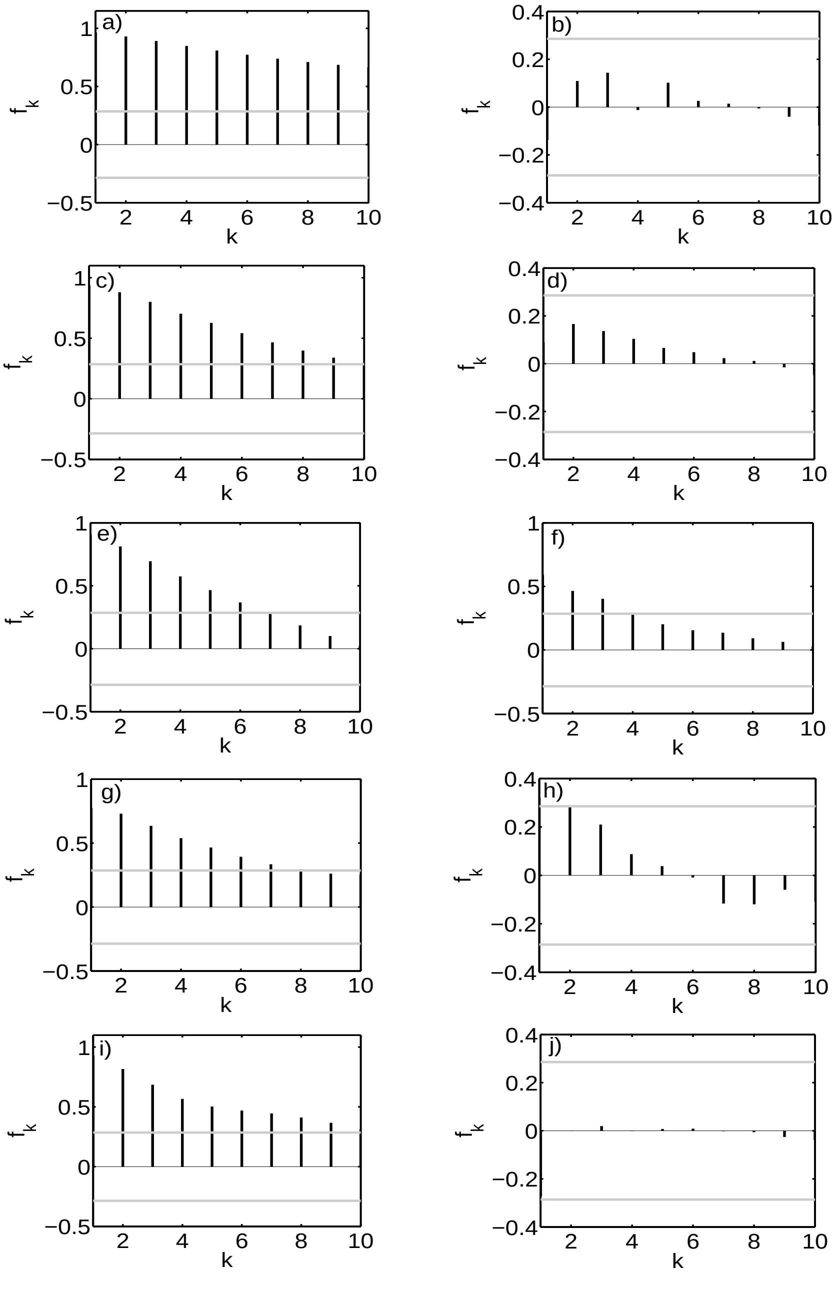

Figure 3.10: Residual autocorrelation function plotted for the (a), (c), (e), (g) and (i) real and (b), (d), (f), (h) and (j) imaginary components of the impedance for (a) and (b) Experiment 1, (c) and (d) Experiment 2, (e) and (f) Experiment 3, (g) and (h) Experiment 4 and (i) and (j) Experiment 5 obtained for λ=0.85. Grey horizontal lines enclose the 95% confidence region for f_k.

The regression parameters λ_1 and λ_2 in Eq. (3.87) incorporate a linear dependence of the residuals calculated using the original model at the nth frequency with the residuals at the $n-1^{th}$ and $n-2^{th}$ frequencies. However, the use of a second–order autoregressive process did not result in any significant reduction in residual correlation. Consequently, the model with the first–order autoregressive process and the parameters shown in Table 3.5 were accepted as the best fit to the experimental data.

3.4.3 Sensitivity Analysis

As shown previously, the fit of the model to the experimental data was found to be insensitive to the values of some kinetic parameters. To examine this more closely, sensitivity analyses were carried out for all the estimated parameters by varying each one separately. The objective was to search for minimum variations in the parameters that resulted in observable differences between the computed impedance electrode responses obtained with the least square–fit parameters. The results are shown in Fig. 3.11 for the conditions of Experiment 1. Although some effect is observed in impedance spectra for such perturbations, the effect on the steady state current–potential curves was insignificant and so is not included. This is an indication of the higher sensitivity of the EIS technique compared to steady state current–potential measurements. The results in Fig. 3.11 indicate that an approximately similar effect is obtained if β_1, β_2, k_1, k_2, k_{-2}, C_{dl} and λ are multiplied by factors of 1.02, 1.1, 1.25, 5, 2, 1.5 and 1.3, respectively, whereas k_{-1} has to be increased by six orders of magnitude. The larger the factor, the less sensitive the model is to the corresponding parameter. This analysis shows that k_{-1} has much less influence on the results compared to the other parameters. The fact that only small perturbations of 2 and 10% are required for β_1 and β_2, respectively, is not surprising since these parameters are found in the arguments of the exponential functions of Eqs. (3.67)–(3.70).

3.4.4 Model Comparison

Given the considerably extra mathematical effort involved in the EIS analysis of this model over what is typically required, it is important to determine if the inclusion of all the phenomena in the model is necessary and leads to significant differences in the results. Accordingly, the results from the previous sections were compared to those from simpler versions

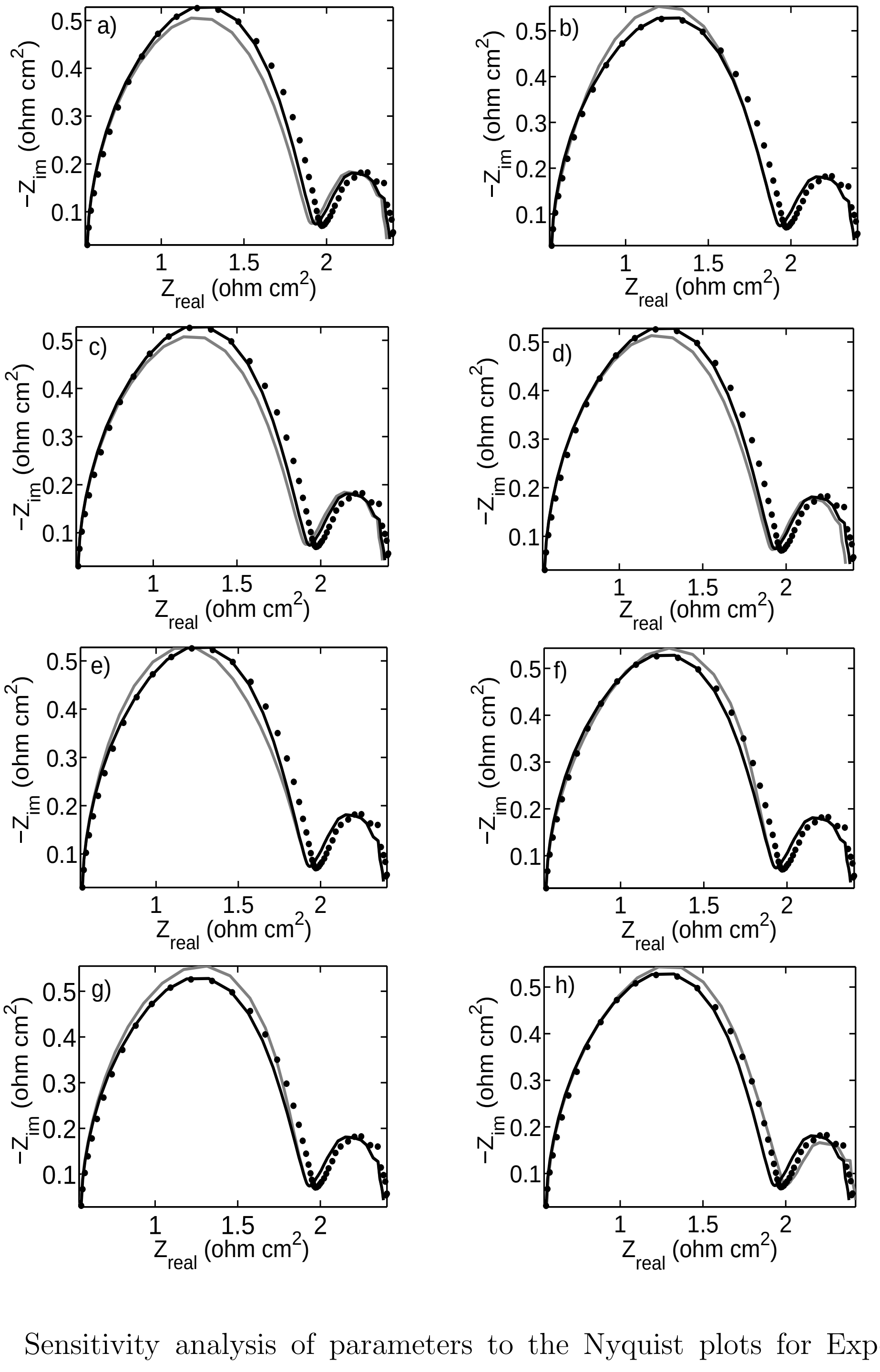

Figure 3.11: Sensitivity analysis of parameters to the Nyquist plots for Experiment 1. Experimental (dotted), original parameters (black), effect of (a) β_1, (b) β_2, (c) k_1, (d) k_{-1}, (e) k_2, (f) k_{-2}, (g) C_{dl} and (h) λ perturbations (grey). Factors by which each original parameter is multiplied is given in the text.

of the model, some of which are more typical of those considered in previous EIS analyses. The first model ($M1$) accounts for diffusion, convection and homogeneous reactions (3.19) and (3.20), but neglects migration. The second ($M2$) accounts for diffusion and homogeneous reactions, but neglects convection and migration. The third ($M3$) accounts for diffusion and convection, but no homogeneous reactions. The last one ($M4$) includes diffusion only. Although models $M2$ and $M4$ do not consider convection in the transport equations, the hydrodynamic conditions are included to some extent since Eq. (3.1) is used to define the boundary layer thickness. It should be noted that models $M2$ and $M4$ are similar to those used in previous EIS analyses not only for Cu^{2+} reduction but also many other systems [29, 30, 36, 37, 55, 64]. For purposes of comparison, Cu^{2+} reduction in all models is assumed to proceed by the same mechanism as in the original with the kinetic parameters given in Table 3.5.

As shown in Fig. 3.12, the current–potential curves according to models $M2$, $M3$ and $M4$ differ significantly from the measured values and those from the original full model. The neglect of migration in model $M1$ produces only a very small deviation from the results obtained using the full model. This result is not surprising since migration is not expected to be important for Cu^{2+} ions in solutions with compositions considered in this study. At high overpotentials where mass transport is important, models $M2$ and $M4$ seriously underestimate the measured current densities. This effect occurs either with the inclusion or exclusion of the homogeneous reactions as would be expected since convection is ignored in the transport equations (Figs. 3.12*b* and *d*). When homogeneous reactions are neglected in the model ($M3$), the computed current densities overestimate the experimental values considerably (Fig. 3.12*c*), reflecting a mismatch with the fitting procedure. The kinetic parameters used in these calculations were obtained from the original model where the total dissolved copper is split between Cu^{2+} and $CuSO_{4(aq)}$. Thus, the value of k_1 in particular so obtained is larger than it would be if it were determined by fitting model $M3$ to the experimental data. Consequently, when it is used in Eqs. (3.13) and (3.17) to compute the current density for the case when all of the dissolved copper is present as Cu^{2+} (*i.e.*, model $M3$), an overestimate of the experimental data results. This is a less serious problem than the neglect of convection since it can be rectified by being consistent with respect to the species considered in the model used to fit to the experimental data

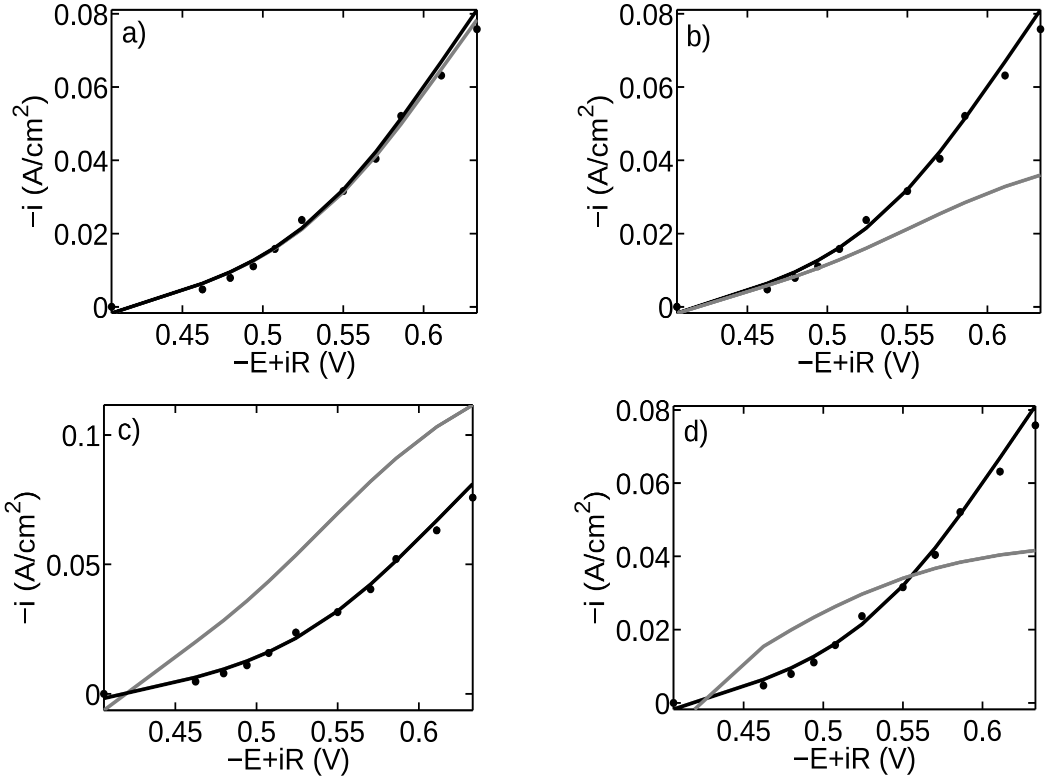

Figure 3.12: Comparison of current–potential curves plots obtained from the full and simplified models for Experiment 1. Experimental (dotted), full model (black), (a) $M1$, (b) $M2$, (c) $M3$ and (d) $M4$ (grey).

and the subsequent use of the model once the parameters are determined.

The effect of the use of the simplified models on the impedance spectra was also investigated. In these calculations, the steady state current density value used for each model was the measured one. A large deviation is observed in the case of $M2$ and $M4$, particularly for the low frequency loop of the impedance plot (Figs. 3.13*b* and *d*). This is not unexpected since this loop is sensitive to mass transfer effects and should be strongly influenced if convection is ignored. The neglect of the homogeneous reactions is reflected in deviations of both the high and low frequency loops from the measured ones (Fig. 3.13*c*).

It must be acknowledged that one could begin with each of the models $M1$–$M4$, fit it to the experimental data to obtain different parameters than those in Table 3.5 and likely achieve comparable agreement to that of the original full model or $M1$. The results in

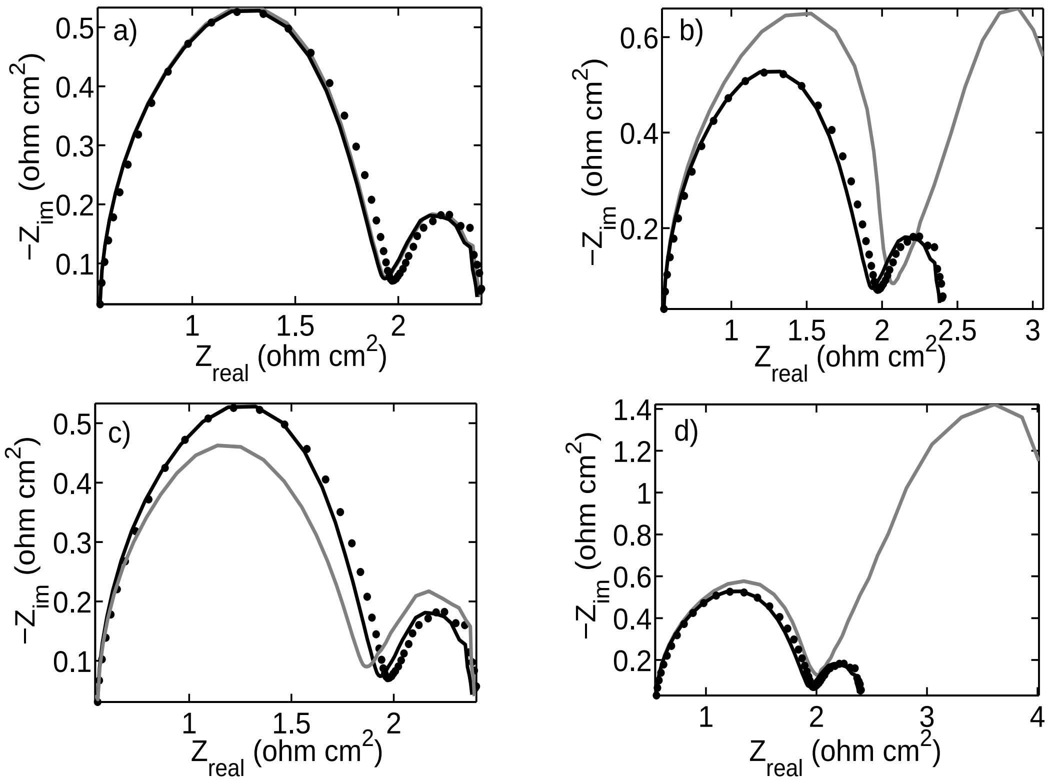

Figure 3.13: Comparison of impedance plots obtained from the full and simplified models for Experiment 1. Experimental (dotted), full model (black), (a) $M1$, (b) $M2$, (c) $M3$ and (d) $M4$ (grey).

Figs. 3.12 and 3.13 suggest that the parameters so obtained from the various models would differ significantly. However, the parameters obtained from the original full model and listed in Table 3.5 should better reflect the true behavior of the system since they are based on a more complete description of processes occurring during Cu^{2+} reduction. Moreover, the largest deviation between the measured computed responses in Figs. 3.12 and 3.13 is exhibited by models $M2$ and $M4$. This is noteworthy since these models are commonly used for the interpretation of EIS data.

Another important implication of these results is a general one concerning how parameter values reported in the literature should be used. As shown in Figs. 3.12 and 3.13, the predicted behavior deviates significantly from the observed behavior when phenomena incorporated in the original model are no longer included. Thus, when using parameters from the literature to do simulations, one should be careful that the model in which they will be used incorporates all the same phenomena as the original one used to determine their values in the first place. Otherwise, significant errors could result.

Chapter 4

Voltammetric Study of Cu Electrodeposition in the Presence of Cl^- and PEG

Chloride ions and polyethylene glycol (PEG) are common additives used in copper electrodeposition to improve the filling of recesses in microelectronic circuit fabrication. The inhibition of the reduction of Cu^{2+} by Cl^- and PEG has received considerable attention in recent years. However, some details of the action of these additives on Cu^{2+} reduction are not completely understood. In this chapter, mostly voltammetry is used to study the effect of the solution composition on the inhibition of Cu^{2+} reduction. The results from this chapter formed the basis for a paper that has been submitted for publication [101].

4.1 Background

4.1.1 Superfilling

A common mixture of additives used in the deposition of copper on patterned substrates includes Cl^-, PEG and SPS or MPS [4, 5, 7, 9, 10, 12, 14, 16]. Some mathematical models have been proposed to simulate the deposition of copper in trenches, vias and other kinds of features found in microelectronic circuits. One such model that has received considerable attention is the curvature enhanced accelerator coverage (CEAC) model [16, 47, 102–104].

The basis of the CEAC model is the preferential adsorption of the species that accelerates metal deposition, *i.e.*, a complex that involves SPS or MPS, at the bottom of the feature. In contrast to what occurs on flat surfaces, the deposition on patterned electrodes causes a continuous change in the shape and area of deposit surface. As long as deposition in a trench progresses, the curvature of the deposit varies over the surface and also changes with time. When superfilling conditions are met, the deposit surface has positive curvature (concave) at the bottom and negative curvature (convex) at the top. Fig. 4.1 shows the situation at two different times $t_1 < t_2$. As the deposit grows, the curvature at the bottom increases.

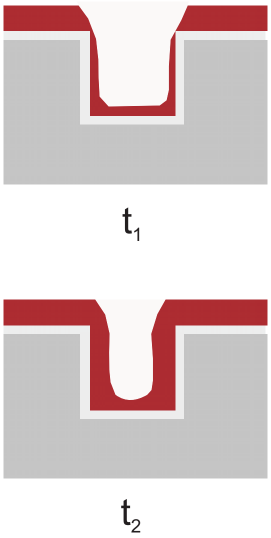

Figure 4.1: Curvature evolution in trench electrodeposition.

According to the CEAC model, the accelerator coverage at the feature bottom increases with time due to the positive curvature of the surface. This in turn enhances the reduction of Cu^{2+} in this part of the feature. On the other hand, the coverage of the accelerator at the top decreases with time due to the negative curvature of this portion of the surface. Although the CEAC model has been useful to predict superfilling for certain conditions, it tends to minimize the role that Cl^- and PEG play on the superfilling phenomenon. For example, superfilling has been shown to be possible in the presence of Cl^- and PEG alone [49, 54]; on the other hand, superfilling does not occur if SPS is present and PEG is not [14]. The CEAC model cannot address these two situations.

Other studies have relied on the competitive adsorption model that is based on differences on adsorption tendencies of the inhibitor PEG and accelerator SPS or MPS [5, 14, 53, 83, 105–108]. The adsorption of the inhibiting species has been found to occur rapidly and be mass transport limited [105]. On the other hand, the accelerator adsorbs instantaneously on free sites but slowly on inhibited sites where it displaces the inhibiting species [105, 109]. Furthermore, due to its bulky size, PEG has much smaller diffusion coefficient than SPS or MPS. Since diffusion is the predominant mode of transport within a trench or via, PEG is transported to the base of such a feature more slowly than the accelerator. As a result of these effects, the accelerator predominantly adsorbs on the bottom and the inhibitor at the top of trenches and vias. Thus, copper is deposited at different rates at the top and bottom of the feature and superfilling conditions can be met.

4.1.2 Nature of the Inhibiting Film

Cl^- and PEG interact with each other and the electrode surface, producing different electrode responses during Cu^{2+} reduction. On one hand, Cu^{2+} reduction is inhibited significantly if Cl^- and PEG are added together to the solution [31, 54, 65, 105, 110–113], but only inhibited slightly when PEG alone is added [54, 70, 105, 110, 113–115]. On the other hand, a strong accelerating effect on Cu^{2+} reduction is observed if only Cl^- is added [54, 114, 116, 117]. Experimental evidence from techniques such as ellipsometry, surface–enhanced Raman spectroscopy (SERS) and differential capacitance measurements has indicated that little or no PEG adsorbs on copper in the absence of Cl^- [116, 118–121].

The ability of Cl^- and PEG to inhibit Cu^{2+} reduction is affected by their concentrations, PEG molecular weight and electrode potential [7, 20, 21, 49, 54, 70, 108, 111, 113, 115, 116, 118, 122–124]. Inhibition increases with Cl^- concentration up to a limit at fixed PEG concentration [7, 20, 49, 111, 116]. If the Cl^- concentration becomes high enough, a decrease in inhibition has been observed, presumably due to precipitation of CuCl [108]. The extent of inhibition also increases to a limit as the PEG concentration rises at a given Cl^- concentration [54, 115, 124]. Similarly, the inhibitory effect increases as the molecular weight of PEG is increased up to a certain value [7, 70, 113]. This limiting condition is attributed to the PEG molecules located close to or adsorbed on the electrode surface reaching a saturated condition [123].

Cu^{2+} reduction is more strongly inhibited at potentials close to the open–circuit potential (OCP) than at more negative potentials. When the concentrations of both PEG and Cl^- are high enough, Cu^{2+} reduction is strongly inhibited until and overpotential of about -0.3 V is reached before the current begins to rise gradually. At intermediate PEG and Cl^- concentrations, almost complete inhibition is observed at potentials below the OCP until a critical value is reached, whereupon the electrode is rapidly re–activated and current abruptly rises to the level observed in PEG–free systems [113, 118]. Depending on the Cl^-, PEG and Cu^{2+} concentrations and the pH of the solution, the critical potential at which the current starts to increase varies between -0.550 and -0.650 V MSE [21, 54, 111, 113, 122]. This potential dependence leads to characteristic hysteresis in voltammograms with more current in the reverse direction of the scans than in the forward direction whenever the cathodic potential limit is more negative than the critical potential and the Cl^- concentration is low enough. The disappearance of the inhibiting film at large cathodic overpotentials re–activates the electrode and results in higher current for Cu^{2+} reduction during the reverse scan than during the forward scan, as reported in some studies [108, 111]. This behavior also indicates that the film is not rapidly restored once it is disrupted even when the electrode is at a potential where the film is intact during the forward scan. The amount of hysteresis is also observed to increase as the Cl^- concentration is reduced at a given PEG level.

Different structures have been proposed for the inhibiting complex adsorbed on the electrode surface. One proposed structure is a complex containing PEG, Cl^- and Cu^+ produced by the reduction of Cu^{2+} and/or the oxidation of substrate. The complex is attached to the copper surface through Cl^-. Cu^+ is bound to Cl^- on one side and to two ether oxygens of PEG on the other side. Evidence of the formation of Cu^+-Cl^- and Cu^+-O bonds was reported by Feng *et al.* [119] and Bozzini *et al.* [125]. Ding *et al.* [126] recently reported results from electrochemical quartz crystal microbalance (EQCM) experiments supporting the view that Cu^+ is a constituent of the inhibiting complex. They dissolved a small amount of copper from an electrode surface in Cu^{2+}–free solutions and subsequently re–deposited it onto the same surface. The mass change of the electrode surface due to deposition in the presence of PEG and Cl^- was found to be larger than when copper was re–deposited in the absence of these two additives, an indication of the adsorption of PEG and Cl^-. On the other hand, no mass change was observed if copper was not allowed to dissolve, suggesting that a PEG-Cl^- film did not readily form in the absence of dissolved copper. In addition to blocking sites on the electrode surface, another proposed role of the PEG-Cu^+-Cl^- complex is to reduce the concentration of free Cu^+ on the surface that can form copper metal [83, 113, 115].

A second proposed structure is a complex of PEG and Cl^- that does not contain copper. Evidence for this structure comes from EQCM measurements on a gold working electrode in a Cu^{2+}–free solution containing PEG and Cl^- [116]. Doblhofer *et al.* [127] came to the same conclusion on the basis of their observation that the degree of inhibition of copper dissolution in multiple CV scans is similar whether or not Cu^{2+} is present in solution. The presence of Cu^+ in this inhibiting film was ruled out since the scans were begun at a negative enough potential where Cu^+ formation was not favored. A similar conclusion was reached by Walker *et al.* [121] from ellipsometric studies in Cu^{2+}–free solutions, which showed that similar films were formed regardless whether copper, silver or gold working electrodes were used. It is important to note that although PEG-containing films have been detected through ellipsometry and EQCM analyses in the absence of Cu^{2+} [116, 121], this does not necessarily prove that these are the same films that are responsible for the inhibition of copper deposition. Obviously, an investigation concerned with the inhibition of copper deposition must involve solutions that contain Cu^{2+}. A third proposal, first made by Healy *et al.* [111] from SERS analyses in solutions containing Cl^- and PEG and small amounts of Cu^{2+}, involves the adsorption of neutral PEG molecules. They attributed the changes in SERS peaks obtained at different potentials to the existence of two adsorbed species: Cl^--Cu^+-PEG complex at potentials near the OCP and neutral PEG at potentials where copper deposition occurs.

This study is concerned with the use of voltammetry and multi-step experiments involving chronoamperometry and voltammetry to gain further insight into the nature of the inhibiting complex and the dynamics of its formation and breakdown. The effect of the solution composition on the inhibition of Cu^{2+} reduction is also studied. Based on recently presented ideas concerning the formation and desorption of PEG films, the relationship between the electrode responses during cathodic scans and structural changes in the film are discussed.

4.2 Experimental

Electrolyte solutions were prepared with cupric sulfate pentahydrate (99.5%, VWR), sulfuric acid (98%, Fisher Scientific) and distilled water. Chemical additives used were a standard hydrochloric acid solution (1.011 N, Aldrich) and polyethylene glycol (average molecular weight 3400, Aldrich). All experiments were conducted at room temperature. The three–electrode cell consisted of a 0.49 cm diameter polycrystalline copper rotating disk working electrode, a copper coil counter electrode and a mercury–mercurous sulfate reference electrode (MSE). All electrode potentials reported herein correspond to the MSE scale. Prior to each experiment, the working electrode was polished using SiC–type abrasive paper (600 and 1200 grade) and 0.3 μm alumina powder. In most cases, the working electrode was rotated at 500 rpm using a Radiometer rotator model EDI101. Voltammetry curves were obtained using an Autolab PGSTAT 30 potentiostat (Eco Chemie). In most experiments, a sweep rate of 2 mV/s was used. At the outset, experiments were conducted in deoxygenated solutions sparged with ultra–high purity nitrogen gas prior to and during the measurements. The electrode responses obtained in these solutions were found to be the same as those obtained in the presence of oxygen. Consequently, no steps were taken to deoxygenate the solution in any subsequent experiments of this study.

Three series of experiments were conducted:

1. *Series I.* These experiments involved scans proceeding from the OCP in the cathodic direction to -0.9 V. All solutions used in these experiments had a base composition of 0.25 M $CuSO_4$+1.8 M H_2SO_4 to which various amounts of HCl and PEG were added. The OCP measured in the base electrolyte or the base electrolyte containing either PEG or Cl^- alone was -0.406 ± 0.005 V, whereas it was measured to be -0.415±0.01 V in the solution containing both additives. This series of experiments served as a basis for comparison with the results of the series II and III experiments. These experiments were also conducted to study the effect of the HCl and PEG concentrations on copper deposition. Concentrations of 1 and 0.1 mM HCl were used in combination with PEG concentrations between 0.01 and 1000 μM.

2. *Series II.* In this series of experiments, scans proceeded cathodically from the OCP in solutions with different initial compositions. At a certain potential during the

cathodic–going sweep, the scan was paused and various amounts of solutions containing 1.8 M H_2SO_4, $CuSO_4$ and possibly HCl and PEG were added to the cell. The composition of the solution being added was adjusted to ensure that the final overall composition for the remainder of the scan was 0.25 M $CuSO_4$+1.8 M H_2SO_4+1 mM HCl+88 μM PEG or 0.25 M $CuSO_4$+1.8 M H_2SO_4+0.1 mM HCl+88 μM PEG. While the solution was added, the stirring speed of the working electrode was increased to 2000 rpm for a few seconds to homogenize the contents and then reduced back to 500 rpm. The current was monitored during the pause and the scan was not resumed until a total time of 10 minutes had elapsed. After the pause, the potential was swept cathodically to -0.9 V before being reversed and increased back to the OCP. The objective of these experiments was to determine whether the order in which the reagents were added affected the electrode response. The solution compositions at the start of the scans and the potentials at which the second solutions were introduced are given in Table 4.1. The potentials of -0.53 V and -0.8 V at which the scans were paused were chosen based on the results of the series I experiments. Copper deposition is completely inhibited at -0.53V and only partially inhibited at -0.8 V in solutions containing 0.25 M $CuSO_4$+1.8 M H_2SO_4+1 mM HCl+88 μM PEG. In solutions containing 0.25 M $CuSO_4$+1.8 M H_2SO_4+0.1 mM HCl+88 μM PEG, copper deposition is reactivated at -0.8 V. In some experiments, the change in current with time during the pause due to the addition of the reagents was monitored to investigate the dynamics of inhibiting film formation.

3. *Series III.* This series of experiments was carried out as follows:

   Step 1. The working electrode was immersed in a solution either at an applied potential or the open circuit potential for 10 minutes to allow a film to be formed and become well–established [16, 128]. The working electrode was then treated in two different ways –removed without rinsing (treatment 1) or removed and then thoroughly rinsed with distilled water (treatment 2)– before being transferred to a second solution.

   Step 2. For both treatments, the stirring speed of the electrode in the second solution was increased to 2000 rpm for a few seconds before being reduced back to 500 rpm prior to the subsequent voltammetric scans. Voltammetric curves

Table 4.1: Experimental conditions for series II experiments.

Experiment	Potential (V)	Initial composition ∗	Final composition ∗
A	-0.53	0.25/0/0	0.25/1/88
B	-0.53	0.25/1/0	0.25/1/88
C	-0.53	0.25/0/88	0.25/1/88
D	-0.53	0.25/0.1/88	0.25/1/88
E	-0.8	0/0/0	0.25/1/88
F	-0.8	0/1/0	0.25/1/88
G	-0.8	0/1.5/132	0.25/1/88
H	-0.8	0.25/0/0	0.25/1/88
I	-0.8	0.25/1/0	0.25/1/88
J	-0.8	0.25/0/88	0.25/1/88
K	-0.8	0.25/0.1/88	0.25/1/88
L	-0.8	0.25/0/0	0.25/0.1/88
M	-0.8	0.25/0/88	0.25/0.1/88

∗ Concentrations indicated correspond to $CuSO_4$/HCl/PEG,
where $CuSO_4$ concentration is given in mol/L, HCl in mmol/L and PEG in μmol/L

were obtained in the second solution by sweeping the potential from the OCP to -0.9 V and back to the OCP. All scans were continued for two complete cycles. The effect of the cathodic potential limit was also studied by carrying out some experiments in which the lower potential was restricted to -0.55 V instead of -0.9 V.

The potential values chosen for step 1 were based on the results of the series I experiments in a solution containing 0.25 M $CuSO_4$+1.8 M H_2SO_4+1 mM HCl+88 μM PEG. Once again, the concentration of H_2SO_4 was maintained at 1.8 M in all cases. These experiments helped determine whether the solution composition during the first step affects the adsorption of species on the electrode.

The two–step experiments reported previously by Yokoi *et al.* [113], Kelly *et al.* [116] and Willey and West [124] are somewhat similar to the series III experiments proposed here, but differ in some important respects. These researchers applied only a fixed potential during step 2 rather than the full scan in the current study. As will be discussed, the use of voltammetry allows us to distinguish between different degrees of inhibition of Cu^{2+} reduction depending on the conditions. Also, a larger number of compositions in the first and second solutions are used in this chapter.

4.3 Results

4.3.1 Series I experiments

Fig. 4.2 shows the current–potential curves obtained in the base $CuSO_4$–H_2SO_4 solution containing no additives (curve 1) and containing each of the following additives: 1 mM HCl (curve 2), 0.1 mM HCl (curve 3), 88 μM PEG (curve 4) and 1 mM HCl+88 μM PEG (curve 5). These curves confirm a number of previously reported observations [54, 114, 116, 117].

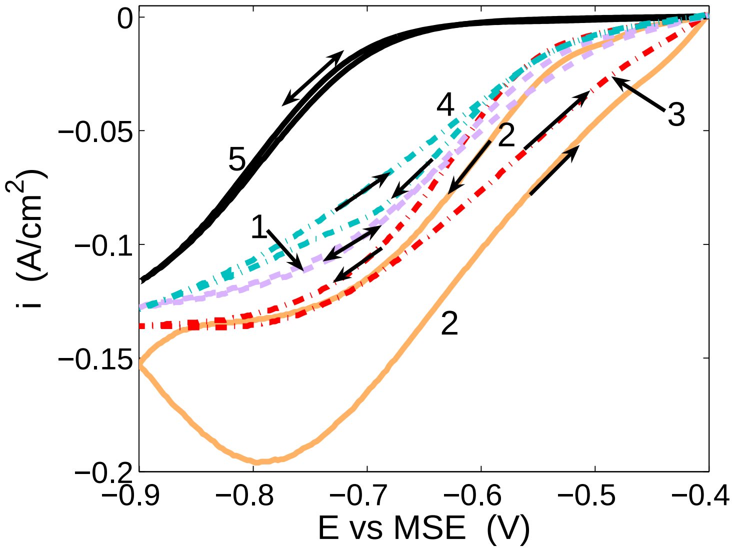

Figure 4.2: Current–potential curves for the following solutions: (1) 0.25M $CuSO_4$+1.8M H_2SO_4; (2) solution 1 + 1mM HCl; (3) solution 1 + 0.1mM HCl; (4) solution 1 + 88μM PEG; (5) solution 1 + 1mM HCl + 88μM PEG. Upper and lower figures correspond to deposition and dissolution of copper, respectively.

The presence of Cl$^-$ alone (curves 2 and 3) accelerates copper deposition. The enhancement of deposition is attributed to the Cu^{2+}-Cl$^-$ bridge at the electrode surface being shorter than the Cu^{2+}-H$_2$O bridges that form in the absence of Cl$^-$ [129]. If PEG alone is added (curve 4), a slight inhibition of copper deposition at all potentials is observed [54, 70, 105, 113–115]. On the other hand, curve 5 indicates that deposition of copper is strongly inhibited when Cl$^-$ and PEG are added together [31, 54, 65, 105, 111–113]. Small currents are observed in the potential region from -0.4 to -0.6 V of curve 5 followed by a gradual increase at more negative potentials.

Fig. 4.2 also shows that when large enough cathodic potentials are reached during the forward scan the current densities for all the curves approach the limiting current density estimated by the Levich equation to be -0.13 A/cm^2, indicating that Cu^{2+} is the soluble electroactive species involved in copper deposition in all cases. This observation was also reported by Eyraud *et al.* [118]. The cathodic current during the reverse scan in the presence of 1 mM HCl exceeds the limiting current density estimated by the Levich equation due to the significant roughening that occurs at large cathodic overpotentials at these higher Cl$^-$ concentrations.

The effect of PEG concentration in the presence of 1 mM HCl is shown in Fig. 4.3. A PEG concentration of 0.01 μM (curve 1) is not large enough to reduce the acceleration caused by the presence of 1 mM Cl$^-$. A similar effect has been reported by Moffat *et al.* [108]. In agreement with previous findings [54, 115], an increase in PEG concentration to 0.1 and 1 μM, causes strong inhibition until a critical potential is reached. Once this critical potential is reached, the current increases sharply and all inhibition is lost. The critical potential is observed to shift cathodically as the PEG concentration is increased at a fixed Cl$^-$ concentration. If the PEG concentration is increased to 50 μM, curve 4 in Fig. 4.3 shows that copper deposition remains strongly inhibited throughout most of the cathodic scan. Evidently, a PEG-Cl$^-$ complex covers the electrode surface throughout the cathodic scan in both directions. An increase in the PEG concentration from 50 μM to 88 μM has no further effect on the electrode response.

In most previous voltammetry studies on the effect of Cl$^-$ on the action of PEG, relatively high Cl$^-$ concentrations of 1 mM or more have been considered. Fig. 4.4 shows the current–potential curves corresponding to those in Fig. 4.3, but obtained at a 0.1 mM HCl

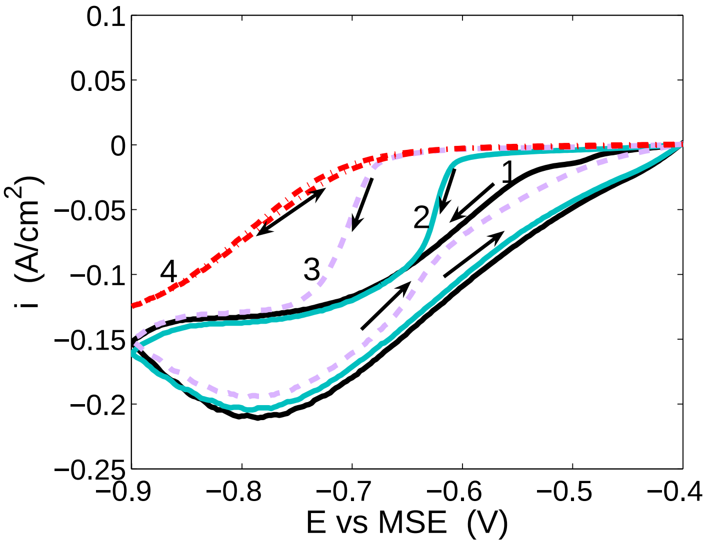

Figure 4.3: Effect of PEG concentration on the current–potential curves obtained in 0.25M $CuSO_4$+1.8M H_2SO_4+1mM HCl solutions. PEG concentrations are (1) 0.01, (2) 0.1, (3) 1 and (4) 50 μM.

concentration. Similar to the results for 1 mM HCl, a 0.01 μM PEG concentration does not impede the acceleration caused by Cl^- (curve 1). The extent of inhibition increases as more PEG is added, as indicated by curves 2 and 3. When the PEG concentration reaches 10 μM and above, the extent of inhibition shown in curve 4 reaches a maximum and no longer changes with further increase in PEG level. Larger current densities are observed in the reverse scan compared to those in the forward scan in all curves when 0.1 mM HCl is added, as shown in Fig. 4.4. This effect called hysteresis is consistent with what has been previously reported and attributed to the consumption of the inhibiting film and mass transport limitations of PEG to the electrode surface when present at a very low concentration [108, 111].

Unlike the situation at 1 mM HCl, the cathodic current never rises above the limiting value estimated from the Levich equation during the reverse scan, presumably due to less roughening during deposition in the presence of 0.1 mM HCl. Also, at the maximum extent of inhibition in the presence of PEG and 0.1 mM HCl (curve 4, Fig. 4.4), the current density for Cu^{2+} reduction does not exhibit the gradual increase during the scan evident at the higher HCl concentration. Instead, it shows a sharp increase at a critical potential to the

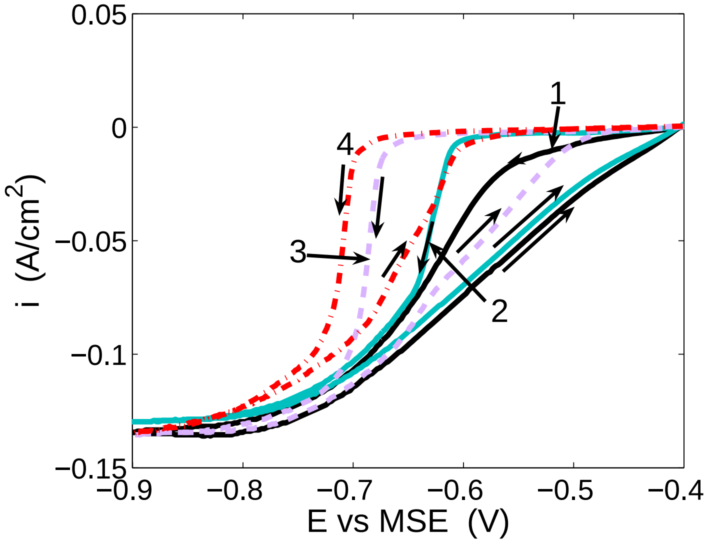

Figure 4.4: Effect of PEG concentration on the current–potential curves obtained in 0.25 M $CuSO_4$+1.8 M H_2SO_4+0.1 mM HCl solutions. PEG concentrations are (1) 0.01, (2) 0.1, (3) 1 and (4) 10 μM.

level observed in the absence of additives. The electrode responses in curves 3 and 4 in Fig. 4.4 also show that some inhibition of Cu^{2+} reduction still occurs during the reverse scan at PEG concentrations of 1 and 10 μM PEG in the presence of 0.1 mM HCl.

Comparison of curve 3 in Fig. 4.3 and curve 3 in Fig. 4.4 shows that for the same PEG concentration, less inhibition is observed as the Cl^- concentration declines, in agreement with previous findings [7, 20, 49, 111, 116]. Furthermore, results presented in Figs. 4.3 and 4.4 show that the PEG/Cl^- concentration ratio has an important effect on the inhibition of copper deposition. However, the PEG/Cl^- concentration ratio is not the only factor that controls inhibition. Comparison of curve 2 in Fig. 4.3 and curve 1 in 4.4 demonstrates that for the same PEG/Cl^- concentration ratio, inhibition is stronger when a larger concentration of HCl is used. The same conclusion is reached after comparing curve 3 in Fig. 4.3 and curve 2 in Fig. 4.4.

It is also worth noting that after the inhibiting film completely breaks down during the scan in curves 1, 2 and 3 in Figs. 4.3 and 4.4, the electrode response exhibits the acceleration of Cu^{2+} reduction relative to that of the additive-free case behavior characteristic of the Cl^-–only system. This is reasonable since there would be a considerable amount of Cl^-

at or near the electrode when all the PEG has detached. On the other hand, the current density in the case of curve 4 in Fig. 4.4 does not rise as sharply after the film is destroyed and appears to more closely follow the response for an additive-free solution. The difference may be related to the fact that the PEG/Cl^- concentration ratio is higher in the experiment associated with curve 4 than in the case of the other curves.

To more closely examine how rapidly the film breaks down at the critical potential, a series of scans were obtained over the range of sweep rates from 2 mV/s to 100 mV/s in a solution containing 0.25 M $CuSO_4$ + 1.8 M H_2SO_4 + 0.1 mM HCl + 88 μM PEG. The resulting curves shown in Fig. 4.5 show that the potential at which the film begins to breakdown remains at -0.71 V and the steep rise portion does not change as the sweep rate is increased from 2 to 20 mV/s. At 100mV/s (experiment S100) a peak is observed at -0.8 V. This peak is likely caused by the inability of Cu^{2+} to be transported to the electrode surface as fast as it is consumed by the electrode reaction at 100 mV/s. The steep rise portion shifts toward negative potentials at 50 mV/s and 100 mV/s, but the potential at which breakdown begins does not change significantly. This suggests that the current rise is associated with an electron transfer reaction. It is also interesting to note that the observed

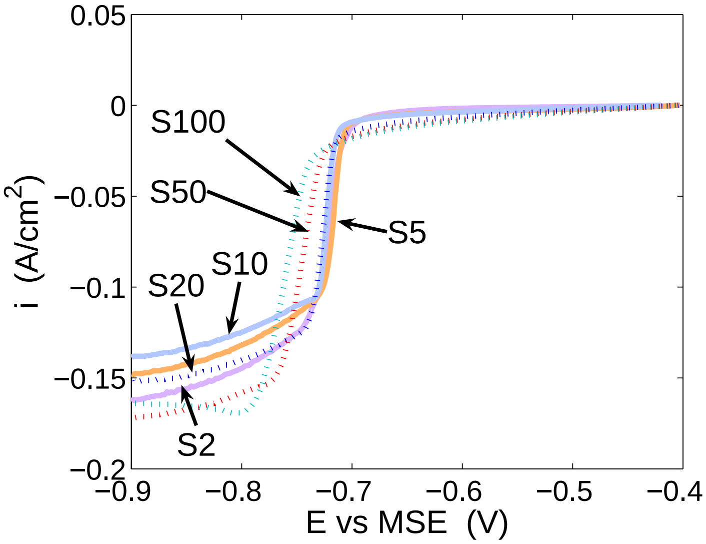

Figure 4.5: Current-potential curves obtained in the solution 0.25M $CuSO_4$+1.8M H_2SO_4+ 0.1mM HCl+88μM PEG at a sweep rate of (S2) 2mV/s, (S5) 5mV/s, (S10) 10mV/s, (S20) 20mV/s, (S50) 50mV/s and (S100) 100mV/s.

critical potential of -0.71 V agrees exactly with the value obtained using the thermodynamic relationship recently developed by Long *et al.* [21]. The kinetics of the film breakdown is obviously very rapid, although the shift in the curves at the highest scan rates reflects some kinetic limitations under these conditions. However, the process whereby the electrode is activated may not be so straightforward. Measurement of the slopes of the steep portions shows them to be much larger than that expected of a 1-electron or even 2-electron transfer reaction described by conventional Butler-Volmer kinetics given by the following expression

$$i = -i_0 \exp\left[-\frac{\beta n F}{RT}\eta\right] \tag{4.1}$$

where i_0 is the exchange current density, n is the number of electrons and η is the overpotential. This is discussed in more detail later.

The scans in Fig. 4.4 indicate that the inhibiting film is completely destroyed by the end of the forward scan. However, once the scan is reversed and reaches above the critical potential, the current in curves 3 and 4 declines to below that observed in additive-free solutions, suggesting that some inhibition has been restored. To investigate this more closely, scans were carried out in which the potential was paused above the critical potential during the reverse portion for a long enough time until steady state was reached. Fig. 4.6 shows the electrode response obtained in a 0.25 M $CuSO_4$ + 1.8 M H_2SO_4 + 0.1 mM HCl + 88 μM PEG solution when the scan is paused at -0.65V (LE1). This Cl^- concentration was chosen to minimize the amount of roughening that could occur during the forward scan at 1.0 mM HCl. Also included in Fig. 4.6 is the curve obtained when the cathodic limit during the forward scan is limited to -0.8 V (LE2). The results show that the original inhibition is completely restored if the potential is raised above the critical potential and enough time is provided regardless of the cathodic limit. Thus, the hysteresis observed in the CV scans at least in the vicinity of -0.65 V and at this solution composition is due more to the dynamics of film restoration than to electrode roughening. The dynamics of the film recovery during the pauses at -0.65 V in experiments LE1 and LE2 in Fig. 4.6 is shown in Fig. 4.7. In experiment LE1, the current decreases by about 60% over the first 10 seconds before declining more gradually. At least 400 seconds are required for inhibition to be completely restored. The response in experiment LE2 is somewhat different in that the current remains uninhibited for the first 20 seconds before decreasing to the inhibited level over the next 10 seconds. The difference in the initial stage of the two responses may

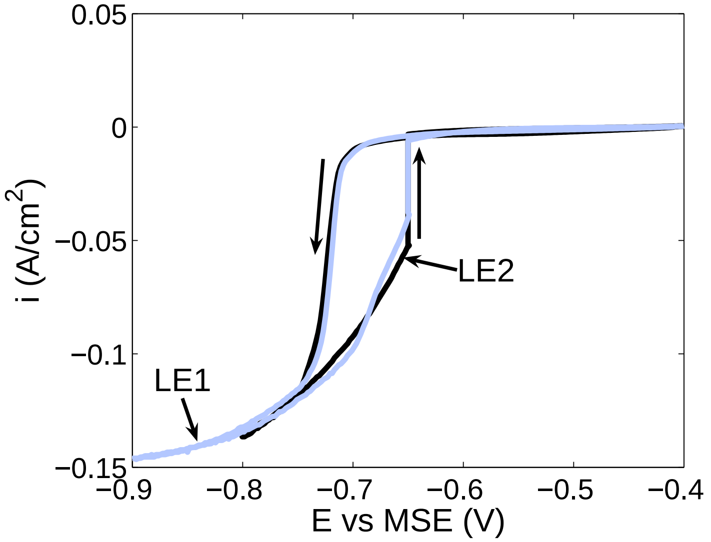

Figure 4.6: Current-potential curves obtained in the solution 0.25M $CuSO_4$+1.8M H_2SO_4+ 0.1mM HCl+88μM PEG after pausing the reverse scan at -0.65 V for 1200 seconds. The cathodic limits during the scan are -0.9V for LE1 and -0.8V for LE2.

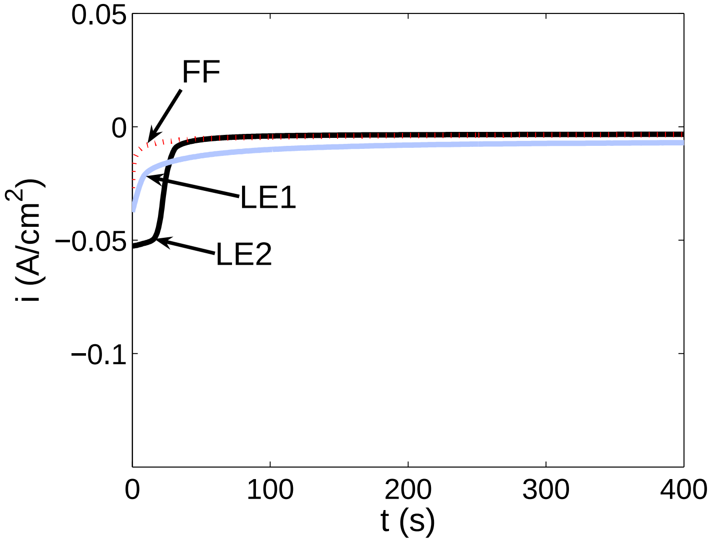

Figure 4.7: Current-time curves obtained in the solution 0.25M $CuSO_4$+1.8M H_2SO_4+ 0.1mM HCl+88μM PEG after pausing the reverse scan (LE1 and LE2) or applying a step potential (FF) at -0.65 V for 1200 seconds. The cathodic limits during the scan are -0.9V for LE1 and -0.8V for LE2.

be related to the fact that Cu^{2+} is likely more strongly depleted in the surface region when -0.65 V is reached during the reverse scan of experiment LE1 than during LE2. Regardless of this difference, the most significant aspect of both responses is that some delay is required for the film to be completely restored.

For comparison, a chronoamperometry experiment was carried out in which a potential of -0.65 V was applied to a fresh electrode in a solution of the same composition as in experiments LE1 and LE2. The resulting current shown as curve FF in Fig. 4.7 is initially the same as in the other two experiments, but decreases much more rapidly to the inhibited state. This may be due to the fact that the surface concentrations of Cu^{2+}, Cl^- and PEG are higher and the inhibiting film should form more rapidly at the outset of the scan than after the scan has been taken to higher overpotentials and then reversed back in the anodic direction. The relative slowness for the film to restore itself after being removed may play a role in the filling of trenches and vias in the Damascene process that normally requires only 40-60 seconds for completion. Most explanations for the success of this process focus on the competition between SPS and PEG for surface sites. The results in Fig. 4.7 indicate that PEG has some difficulty in re–adsorbing even in the absence of a competing additive.

4.3.2 Series II experiments

The resulting current–potential curves in Fig. 4.8 correspond to experiments A to D while those in Fig. 4.9 correspond to experiments E to K (see Table 4.1). As described previously, the solution composition differs from experiment to experiment at the beginning of each scan, but then is adjusted to bring it to 0.25 M $CuSO_4$+1.8 M H_2SO_4+1 mM HCl+88 μM PEG at either -0.53 or -0.8 V. The numbers next to the curves correspond to the designations given in Table 4.1. For comparison, the curves obtained for the series I experiments in 0.25 M $CuSO_4$+1.8 M H_2SO_4 and 0.25 M $CuSO_4$+1.8 M H_2SO_4+1 mM HCl+88 μM PEG solutions are also included as curves NA and SR, respectively. As noted previously, the scan was paused at -0.53 or -0.8 V for a long enough time to ensure that the electrode response to the change in solution composition had reached steady state.

Figs. 4.8 and 4.9 show that no matter the initial solution composition the electrode responses shift to eventually become the same as that of curve SR from the series I experiments once the reagents have been added to bring the solution composition to 0.25 M

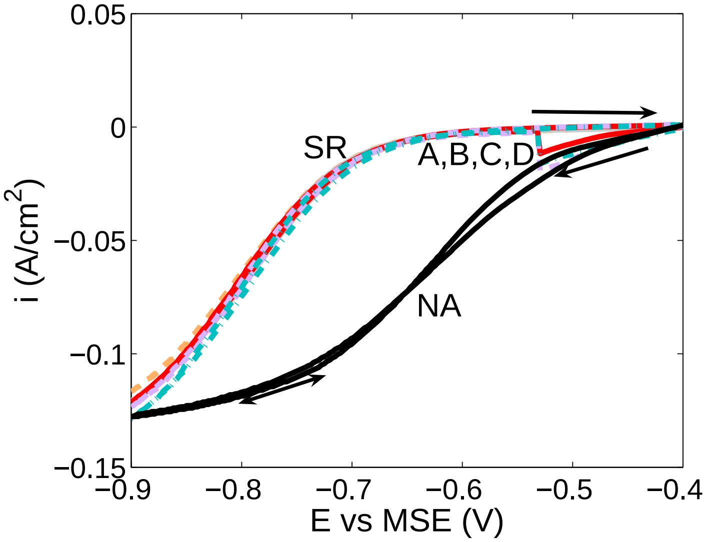

Figure 4.8: Current–potential curves obtained after pausing the scan at -0.53 V for the addition of reagents in series II experiments. The numbers next to the curves denote experiments listed in Table 4.1. The final solution is 0.25 M $CuSO_4$+1.8 M H_2SO_4+1 mM HCl+88 μM PEG.

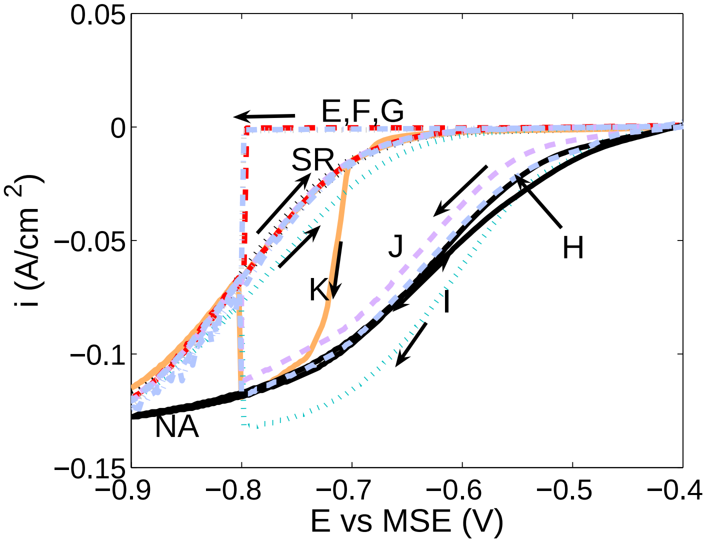

Figure 4.9: Current–potential curves obtained after pausing the scan at -0.8 V for the addition of reagents in series II experiments. The numbers next to the curves denote experiments listed in Table 4.1. The final solution is 0.25 M $CuSO_4$+1.8 M H_2SO_4+1 mM HCl+88 μM PEG.

$CuSO_4$+1.8 M H_2SO_4+1 mM HCl+88 μM PEG. Hence, the order in which additives are incorporated into the solution does not appear to affect their ultimate ability to inhibit copper deposition. Moreover, the potential at which additives are incorporated does not affect this conclusion. The response obtained in experiment J (Fig. 4.9) shows that PEG has a small inhibitory effect unless Cl^- is also present. The result from experiment K is also worth noting. During the first part of this scan until the pause at -0.8 V, the solution composition is 0.25 M $CuSO_4$+1.8 M H_2SO_4+0.1 mM HCl+88 μM PEG. Cu^{2+} reduction is suppressed until a potential of about -0.7 V is reached, whereupon it is rapidly activated. The subsequent addition of more Cl^- causes Cu^{2+} reduction to be inhibited once again. The response after the solution is changed shows that even after the electrode potential becomes negative enough for the inhibiting effect to be destroyed at the lower HCl concentration of 0.1 mM, its full inhibiting effect can be restored by the addition of more HCl to bring the overall concentration to 1 mM.

In order to determine how much of the effect observed in experiment K is due to the change in the composition and due to the elapsed time that the potential is held at -0.8 V, an experiment was conducted under the same conditions as above except that the potential scan was paused at -0.8 V without changing the composition from 0.25 M $CuSO_4$+1.8 M H_2SO_4+0.1 mM HCl+88 μM PEG (Fig. 4.10). In contrast to the result in experiment K, Fig. 4.10 shows that the current density increases when the potential is held at -0.8V. Thus, the reduction in current in experiment K can be attributed to the increase in HCl concentration that restores the inhibiting film. The rise in current during the pause at -0.8 V in the experiment shown in Fig. 4.10 is due to electrode roughening since the current is already at the mass transfer limiting value for a smooth electrode at the start of the pause.

In Fig. 4.11, the resulting current-potential curves are shown for experiments L and M (Table 4.1). The solution contains 0.25 M $CuSO_4$ but no additives at the start of experiment L and 0.25 M $CuSO_4$+88 μM PEG at the start of experiment M. Cl^- is not present in either case until the pause at -0.8 V. In both cases, the solution compositions were adjusted during the pause at -0.8 V during the forward scan to be 0.25 M $CuSO_4$+1.8 M H_2SO_4+0.1 mM HCl+88 μM PEG for the remainder of the experiment. Note that copper deposition is not inhibited at a potential of -0.8 V in a solution containing 0.25 M $CuSO_4$+1.8 M H_2SO_4+0.1 mM HCl+88 μM (experiment K in Fig. 4.9). The similarity of the current at

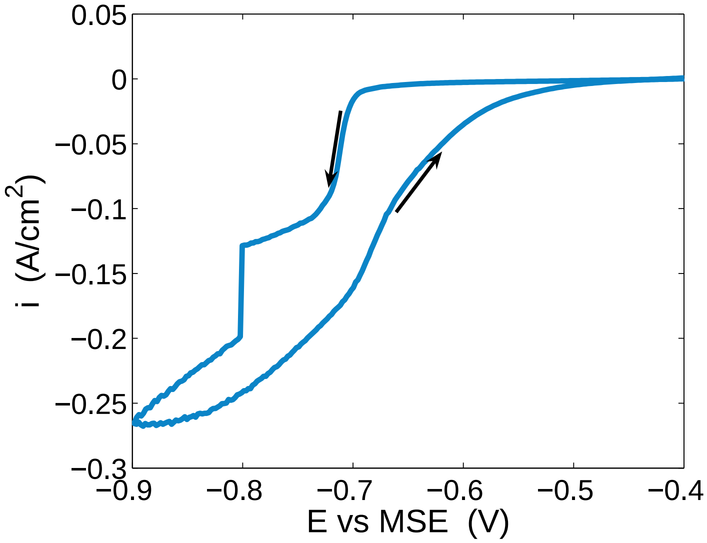

Figure 4.10: Current–potential curve obtained after pausing the forward scan at -0.8 V in the solution 0.25 M $CuSO_4$+1.8 M H_2SO_4+0.1 mM HCl+88 μM PEG.

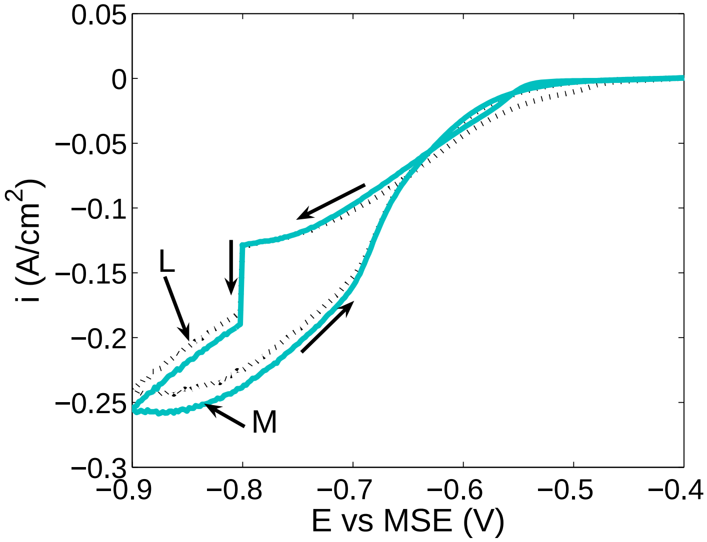

Figure 4.11: Current–potential curves obtained after pausing the scan at -0.8 V for the addition of reagents in series II experiments. The numbers next to the curves denote experiments listed in Table 4.1. The final solution is 0.25 M $CuSO_4$+1.8 M H_2SO_4+0.1 mM HCl+88 μM PEG.

the end of the pause in both cases with that in Fig. 4.10 shows once again that the order in which are incorporated into the solution does not affect the ultimate response. More importantly, the fact that no decrease in current is observed during the pause signifies that none of the PEG present in solution from the start of the experiment is able to adsorb even with the addition of Cl^-. This is contrasted with the behavior observed during a similar experiment in which the scan is paused and Cl^- is introduced at a potential above the critical potential. In this case, the current becomes suppressed upon addition of Cl^-. Thus, the ability of PEG to completely cover the electrode with an inhibiting film depends on potential at a Cl^- concentration of 0.1 mM. However, when the Cl^- concentration is 1.0 mM, an inhibiting film can form and cover the electrode at all potentials between -0.4 V and -0.9 V.

The results in Figs. 4.8–4.11 show the final current densities reached once the reagents are added. However, information concerning the dynamics of the electrode response in some of these cases could provide further insight into film formation. As discussed in section 4.1.2, a question of some debate has been whether or not Cu(I) forms part of the inhibiting PEG-Cl^- film. The results of experiments E and G are worth noting in this regard. The solution in experiment E contains only 1.8 M H_2SO_4 until a potential of -0.8 V is reached during the forward scan, whereupon Cu^{2+}, PEG and Cl^- are added for the first time. The initial solution in experiment G also contains 1.5 mM HCl and 132 μM PEG but no Cu^{2+} until the pause. As with all experiments A-K in series II, small volumes of the appropriate solutions were added during the pause to bring the final composition to 0.25 M $CuSO_4$+1.8 M H_2SO_4+1 mM HCl+88 μM PEG. If Cu(I) is not a component of the inhibiting film, the film should still have been able to form on the electrode in the first part of experiment G before Cu^{2+} was added at the pause. In contrast, the film could only begin to form during the pause in experiment E. Consequently, one might expect to observe some difference in the electrode responses during the pause period of experiments E and G. As shown in Fig. 4.12, the transient curves in the two cases are very similar. The current reaches the level characteristic of the inhibited state within 35 seconds and remains unchanged thereafter. Thus, it is not possible to conclude from these experiments if Cu(I) forms part of the PEG-Cl^- film or if the film has a different inhibiting effect depending on whether or not it contains Cu(I). For comparison purposes, the curve labeled NA shows

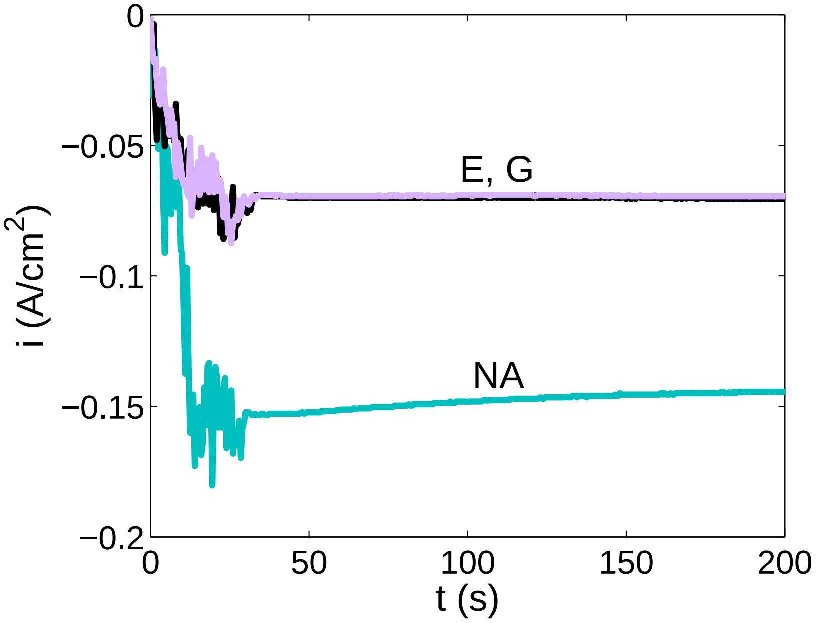

Figure 4.12: Current-time curves obtained after the addition of $CuSO_4$ solutions in experiments E and G. The solution compositions prior to the pause are listed in Table 4.1. Curve NA corresponds to the transient obtained after the addition of $CuSO_4$ in the additive–free case.

the response when Cu^{2+} is added to a solution containing only H_2SO_4 in the absence of Cl^- and PEG to bring the composition to 0.25 M $CuSO_4$+1.8 M H_2SO_4.

Fig. 4.13 shows how the current changes with time during the pause period of experiment H due to changes in the stirring speed and the addition of PEG and Cl^- to a solution initially containing Cu^{2+}, but no additives. The formation of the inhibiting film upon additional PEG and Cl^- at t=100 s is extremely rapid and steady state is reached within 6 seconds.

To follow the effects of PEG and Cl^- more closely, an experiment similar to that shown in Fig. 4.13 was conducted, but with the reagents added in stages rather than all at once. In this experiment, the scan was paused at -0.7 V to add small volumes of the appropriate solution rather than at -0.8 V to minimize complications due to electrode roughening that might otherwise arise. The first four reagent additions raised the HCl concentration in increments of 0.05 mM. As with experiment H, the solution contained no PEG and Cl^-

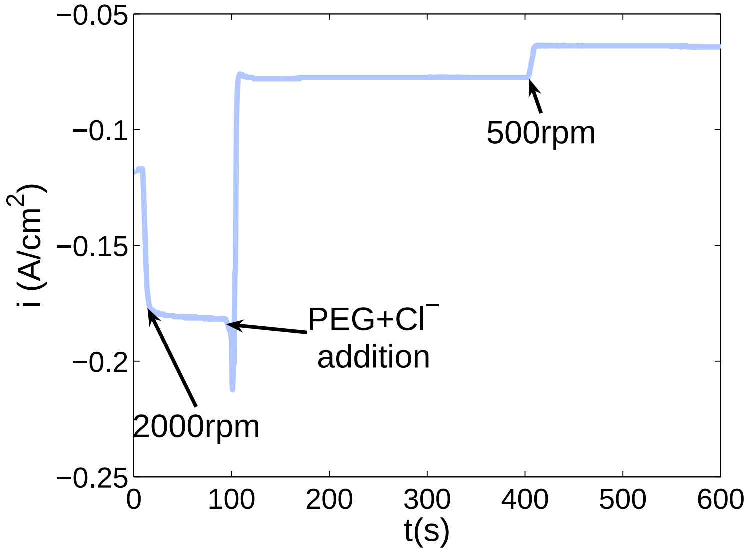

Figure 4.13: Current–time transient obtained after the addition of Cl$^-$ and PEG to a solution at -0.8 V to bring final composition to 0.25 M $CuSO_4$+1.8 M H_2SO_4+1 mM HCl+88 μM PEG (experiment H). The arrows indicate the points at which a change in rotation speed or the reagent addition is made.

prior to the pause, but 1.0 mM HCl+88 μM PEG after all the additions were made and the potential scan resumed.

The resulting electrode response is shown in Fig. 4.14. The current density rises to ~0.145 A cm^{-2} with the increase in rotation speed to 2000 rpm before PEG and Cl$^-$ are added. The first addition of Cl$^-$ and PEG (P1) which brings their concentrations to 0.05 mM and 4.42 μM, respectively, causes the current to decrease immediately by a small amount to -0.12 A cm^{-2}. This is followed by a slow relaxation period of ~140 seconds where some, but not all, of the current is recovered. The second addition (P2) raising the Cl$^-$ and PEG concentrations to 0.1 mM and 8.84 μM, respectively, has a similar effect, although a longer period of about 300 seconds is required before steady state is reached. The electrode response to the third addition (P3) which increases the additive levels to 0.15 mM HCl and 13.3 μM PEG is dramatically different. The current density drops immediately and rapidly reaches steady state at -0.01 A cm^{-2} within a few seconds. Subsequent additions of Cl$^-$ and PEG have no further effect on the current. The reduction of rotation speed back to 500 rpm after about 1000 seconds of the pause period has no effect on the current.

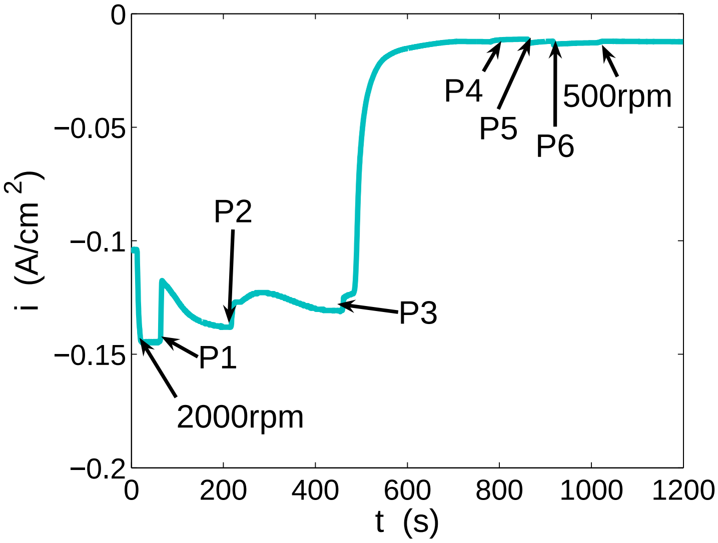

Figure 4.14: Current–time transients obtained after the addition of Cl^- and PEG to a solution with initial composition 0.25 M $CuSO_4$+1.8 M H_2SO_4 at -0.7V. The arrows indicate the point at which the change in rotation speed or the reagent addition is made. The solution after the addition of Cl^- and PEG contains (P1) 0.05 mM HCl+4.42 μM PEG, (P2) 0.1 mM HCl+8.84 μM PEG, (P3) 0.15 mM HCl+13.3 μM PEG, (P4) 0.2 mM HCl+17.7 μM PEG, (P5) 0.6 mM HCl+52.8 μM PEG and (P6) 1 mM HCl+88 μM PEG.

The small amount of Cu^{2+} reduction that occurs now presumably depends on processes occurring within the inhibiting film and no longer on transport within the solution.

Another experiment of this type was carried out, but with the objective to measure the electrode response when the Cl^- concentration alone was raised in a solution initially containing PEG but no Cl^-. Thus, the solution contained 0.25 M $CuSO_4$+1.8 M H_2SO_4+88 μM PEG at the beginning of the scan until the pause at -0.7 V, whereupon small volumes of an appropriate Cl^-–containing solution were added in stages. A comparison of the electrode response in Fig. 4.15 with the previous one in Fig. 4.14 over the initial period of the pause before any Cl^- is introduced shows that the presence of 88 μM PEG alone causes some inhibition of Cu^{2+} reduction. The first addition (P1) to bring the Cl^- concentration to 0.05 mM has an interesting effect in that the rate of Cu^{2+} reduction eventually rises above that observed in the presence of PEG alone after about 150 seconds, although it is still inhibited relative to the level attained in an additive-free solution (see additive-free portion

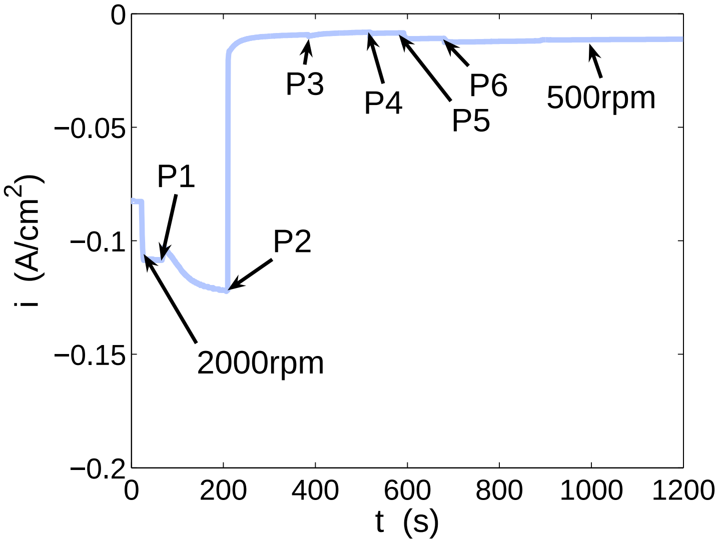

Figure 4.15: Current–time transients obtained after the addition of Cl^- to a solution with initial composition 0.25 M $CuSO_4$+1.8 M H_2SO_4+88 μM PEG at -0.7V. The arrows indicate the point at which the change in rotation speed or the reagent addition is made. The solution after the addition contains (P1) 0.05 mM HCl, (P2) 0.1 mM HCl, (P3) 0.15 mM HCl, (P4) 0.2 mM HCl, (P5) 0.6 mM HCl and (P6) 1 mM HCl.

of response in Fig. 4.14). With the subsequent Cl^- addition (P2), a strongly inhibiting film instantaneously forms, causing an immediate and permanent drop in current density to about -0.01 A cm^{-2}. No further change in current is observed over the remainder of the pause period. The onset of strong inhibition has occurred when the Cl^- concentration reaches 0.10 mM in this experiment, but 0.15 mM in the previous one (Fig. 4.14). This difference is presumably due to the higher PEG concentration in the former case than in the latter.

Taken together, the results in Figs. 4.14 and 4.15 suggest that at lower Cl^- and PEG concentrations, some adsorption of the additives occurs, but not to completely cover the substrate. The effect on the electrode is slow acting and variable depending on the additive concentrations. However, once a critical Cl^- concentration of about 0.1 mM is present (exact level depends on PEG concentration), a sudden change occurs whereby an inhibiting film rapidly forms to cover the substrate and strongly suppress Cu^{2+} reduction.

4.3.3 Series III experiments

For the purposes of the discussion of these experiments, the resulting electrode responses were grouped as shown in Fig. 4.16. The responses showing acceleration of Cu^{2+} reduction at all potentials are represented by the letter A. This is typical of the response for Cu^{2+} reduction in the presence of Cl^-, but not PEG. The letter N denotes those cases where the current–potential curve does not show inhibition for Cu^{2+} reduction at any potential. A first type of moderate inhibition, denoted as M1, applies for the cases where the current density is negligible at potentials more positive than -0.53 V. A second type of moderate inhibition, denoted as M2, corresponds to those cases where the current density is negligible at potentials more positive than -0.55 V. The inhibitory effects in the case of M1 and M2 are lost once they are disrupted at the critical potential. After this disruption, M1 becomes similar to that observed in the absence of additives, whereas the current in M2 increases to the level observed in response A when Cl^- is the only additive present. The third type of moderate inhibition M3 occurs when the current shows slight inhibition at all potentials characteristic of that observed in the presence of PEG alone. The strongest inhibition is

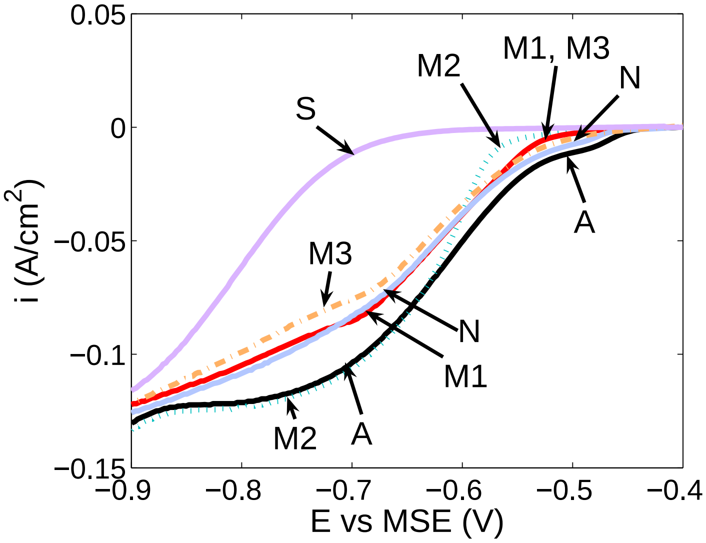

Figure 4.16: Current–potential curves representing the different degrees of inhibition during copper deposition: (A) acceleration, (N) no–inhibition, (M1, M2 and M3) moderate and (S) strong inhibition.

denoted as S and is characterized by complete inhibition at potentials as negative as -0.6 V followed by a gradual rise in current.

The results for the series III experiments are summarized in Tables 4.2 to 4.4. Each row in these tables corresponds to a different solution or applied potential used in step 1 of these experiments, while each column corresponds to a different solution or cathodic potential limit of the scan applied in step 2. Each entry in these tables appears as a pair of designations of Cu^{2+} reduction response corresponding to the first and second scan during step 2. The number designation of the experiment is indicated in parenthesis next to each table entry. All results in Tables 4.2 and 4.3 were obtained for a cathodic potential limit of -0.9 V during step 2.

The data in Table 4.2 were obtained using treatment 1 (no rinsing) during step 1 and a copper working electrode. Thus, liquid clinging to the electrode as it is removed during step 1 is carried over into solution 2. As indicated in the second column, a moderate M1 inhibition during the first scan of step 2 is observed even when PEG and Cl^- are not contained in solution 2, presumably due to some PEG and Cl^- being carried over from step

Table 4.2: Effect of treatment 1 on the degree of inhibition in series III experiments.

Solution 1*, applied E	Cathodic potential limit=-0.9V	
	Solution 2*	
	0.25/0/0	0.25/1/0
0.25/1/88 OCP	M1/N (1’)	M2/A (2’)
0.25/1/88 -0.7V	M1/N (3’)	M2/A (4’)
0/1/88 OCP	M1/N (5’)	M2/A (6’)
0/1/88 -0.7V	M1/N (7’)	M2/A (8’)
0/0/88 -0.7V	N/N (9’)	M2/A (10’)

∗ Concentrations indicated correspond to $CuSO_4$/HCl/PEG,
where $CuSO_4$ concentration is given in mol/L, HCl in mmol/L and PEG in μmol/L

1. Only when Cl^- is absent from both solutions is Cu^{2+} reduction uninhibited (experiment 9'). When the second solution contains Cl^-, moderate M2 inhibition is observed in the first scan for all compositions of solution 1 (third column). In all cases in Table 4.2, no evidence for inhibition appears in the second scan during step 2, indicating that any film has been destroyed at the high cathodic overpotentials of the first scan. One cannot be certain whether the film is irreversibly removed or cannot be restored quickly enough in the time during which the scan is above the critical potential at the end of the first cycle and beginning of the second cycle.

The moderate inhibition observed in experiments 1'-8' in Table 4.2 indicates that some PEG and Cl^- are carried over in the liquid clinging to the electrode or adsorb on the electrode during step 1. Even in experiment 10' when only PEG is present in solution 1, it also appears to be carried over into step 2 since it is known that little or no PEG adsorbs on copper in the absence of Cl^- [116, 118–121]. If Cl^- and PEG are carried over in the liquid clinging to the electrode, enough could be present to inhibit Cu^{2+} reduction even when the second solution contains no PEG and Cl^-. The series I experiments showed that some inhibition of Cu^{2+} reduction is still possible at additive levels as low as 0.1 μM PEG and 0.1 mM Cl^- (curve 2 in Fig. 4.4). However, it should be emphasized that the degree of inhibition observed in all the experiments in Table 4.2 never attains the strongest category.

Most of the series III experiments were conducted using treatment 2 where the electrode was well–rinsed at the end of step 1 prior to being transferred to solution 2. Consequently, any carry-over of PEG and/or Cl^- from step 1 to step 2 could be ascribed to adsorption onto the substrate. Several conclusions can be reached from the results of these experiments shown in Table 4.3. Firstly, strong inhibition during step 2 occurs only when Cu^{2+}, Cl^- and PEG are added together in that step (*i.e.*, experiments 4, 8, 12, 16, 20, 24, 28 and 32). Moreover, this effect is observed regardless of the solution composition and applied potential in step 1. Secondly, the moderate inhibition observed in experiments 1', 3', 5' and 7' when the electrode is not rinsed between steps can be attributed to PEG and Cl^- being carried over in the solution adhering to the electrode during step 1 since no inhibition is observed in any of the corresponding experiments in which the electrode is well rinsed during step 1 (*i.e.*, experiments 13, 17, 25 and 29). Thirdly, the moderate inhibition M2 during step 2 of experiments 14, 18, 22, 26 and 30 when solution 2 contains no PEG

Table 4.3: Effect of treatment 2 on the degree of inhibition in series III experiments.

Solution 1*, applied E	Cathodic potential limit=-0.9V			
	Solution 2*			
	0.25/0/0	0.25/1/0	0.25/0/88	0.25/1/88
0.25/1/0 OCP	N/N (1)	A/A (2)	M3/M3 (3)	S/S (4)
0.25/0/88 OCP	N/N (5)	A/A (6)	M3/M3 (7)	S/S (8)
0.25/0/88 -0.7V	N/N (9)	A/A (10)	M3/M3 (11)	S/S (12)
0.25/1/88 OCP	N/N (13)	M2/A (14)	M3/M3 (15)	S/S (16)
0.25/1/88 -0.7V	N/N (17)	M2/A (18)	M3/M3 (19)	S/S (20)
0.25/0.1/88 OCP	N/N (21)	M2/A (22)	M3/M3 (23)	S/S (24)
0/1/88 OCP	N/N (25)	M2/A (26)	M3/M3 (27)	S/S (28)
0/1/88 -0.7V	N/N (29)	M2/A (30)	M3/M3 (31)	S/S (32)
0/0/88 -0.7V	N/N (33)	A/A (34)		

$*$ Concentrations indicated correspond to $CuSO_4$/HCl/PEG,
where $CuSO_4$ concentration is given in mol/L, HCl in mmol/L and PEG in μmol/L

provides evidence of the adsorption of PEG and Cl^- onto copper during step 1 of these experiments. However, the fact that no inhibition is observed in experiments 13, 17, 21, 25 and 29 signifies that the adsorption of PEG and Cl^- in step 1 does not guarantee inhibition in step 2. A necessary requirement for moderate M2 inhibition is the presence of Cl^- in solution 2. This observation suggests that any PEG adsorbed on the substrate during step 1 subsequently desorbs in solution 2 if it does not contain Cl^-. It is worth noting that the moderate inhibition M3 observed in experiments 15, 19, 23, 27 and 31 is not as significant at potentials between -0.5 and -0.6 V as the moderate inhibition M2 in experiments 14, 18, 22, 26 and 30 (see Fig. 4.16). The small inhibition in the experiments of the fourth column of Table 4.3 is presumably caused by the presence of PEG alone in solution 2 since the same response is observed regardless of the composition of solution 1 and is characteristic of the response in a PEG-only solution.

It should be noted that the responses in experiments 13, 14, 17 and 18 are consistent with the observations made by Yokoi *et al.* [113], Kelly *et al.* [116] and Willey and West [124], although their studies were based on chronoamperometry experiments rather than linear potential scans. Kelly *et al.* carried out an experiment with solution 1 containing Cu^{2+}, Cl^- and PEG, and solution 2 containing Cu^{2+} and Cl^-. They found that in solution 2, Cu^{2+} reduction was always inhibited if the electrode was held for 20 minutes at a potential more positive than that required for film disruption; Yokoi *et al.* also observed this effect. Willey and West found that the period of time over which Cu^{2+} reduction remained inhibited decreased as potential became more negative. In a second experiment with Cu^{2+}, Cl^- and PEG in solution 1 and Cu^{2+} in solution 2, Kelly *et al.* found that Cu^{2+} reduction at -0.5, -0.55 and -0.6 V in solution 2 was inhibited for only a few seconds before being restored to the levels of the additive–free case.

Acceleration is observed in experiments 6, 10 and 34, indicating that no adsorbed PEG was present during step 2. On the other hand, the observation of some inhibition of Cu^{2+} reduction in experiments 26 and 30 where only PEG and Cl^- are present in solution 1 clearly shows that the presence of Cl^-, but not Cu^{2+}, in solution is required for adsorption of PEG onto the substrate at both the OCP and -0.7 V. However, it is important to emphasize that the degree of inhibition observed during step 2 is only moderate when PEG and Cl^- are added and presumably adsorb during step 1, but are not added again at the start of step 2. As defined in Fig. 4.16, moderate inhibition M2 corresponds to suppression of Cu^{2+} reduction only at potentials above about -0.55 V followed by a rapid current increase to the same level observed when Cl^- is the only additive and has an accelerating effect. Presumably, the PEG-Cl^- film present at the start of step 2 is disrupted after only a small overpotential during the cathodic scan and is never re–established. Comparison of the results of experiments 10' (Table 4.2) and 34 indicates that the moderate inhibition in the former case arises only because PEG is carried over in the solution adhering to the electrode during step 1 and not because it adsorbed onto the substrate.

Inhibition is not observed during the second scan of the experiments shown in Tables 4.2 and 4.3 except for those corresponding to the last two columns of Table 4.3. However, the degree of inhibition in the second scan of the experiments in the fourth column of Table 4.3 is much less than that observed in the last column since solution 2 contains PEG, but not Cl^-. The fact that strong inhibition during the second scan is observed only for those experiments in the fifth column suggests that the inhibiting film is irreversibly disrupted at large cathodic potentials unless the second solution contains Cu^{2+}, Cl^- and PEG. To test this idea, the cathodic potential limit during step 2 was changed from -0.9 V to -0.55 V and experiments repeated to yield the results shown in Table 4.4. Comparison of the results of experiments 29 and 30 presented previously with experiments 35 and 36, respectively, shows that inhibition persists in the second scan if the cathodic limit of the scan is not more negative than the critical potential. Thus, the large cathodic potentials applied during the first scan in experiment 30 would appear to be responsible for the loss of inhibition in the second scan. The disruption of the inhibiting film at large cathodic potentials caused by Cl^- desorption has been previously reported [111, 119, 125]. However, the shorter scan time in experiment 36 could also be partly responsible for restoration of the inhibiting film. Thus, a scan was conducted in which the potential was swept to -0.55 V and then held fixed at this potential for 350 seconds which is the additional elapsed time required to reach the start of the second scan in experiment 30 compared to that in experiment 36. Fig. 4.17 shows the dynamics of the resulting electrode response over the 350 seconds the

Table 4.4: Effect of cathodic potential limit on the degree of inhibition in series III experiments.

Solution 1*, applied E	Solution 2*			
	0.25/0/0		0.25/1/0	
	Cathodic potential limit			
	-0.9V	-0.55V	-0.9V	-0.55V
0/1/88 -0.7V	N/N (29)	N/N (35)	M2/A (30)	M2/M2 (36)
0/0/88 -0.7V	N/N (33)	N/N (37)	A/A (34)	A/A (38)

* Concentrations indicated correspond to $CuSO_4$/HCl/PEG, where $CuSO_4$ concentration is given in mol/L, HCl in mmol/L and PEG in μmol/L

potential is held at -0.55 V. Over the first 50 seconds or so, the current remains inhibited, but thereafter the current begins to rise toward the uninhibited level. Thus, the difference observed in experiments 30 and 36 cannot be attributed to differences in cathodic limit alone.

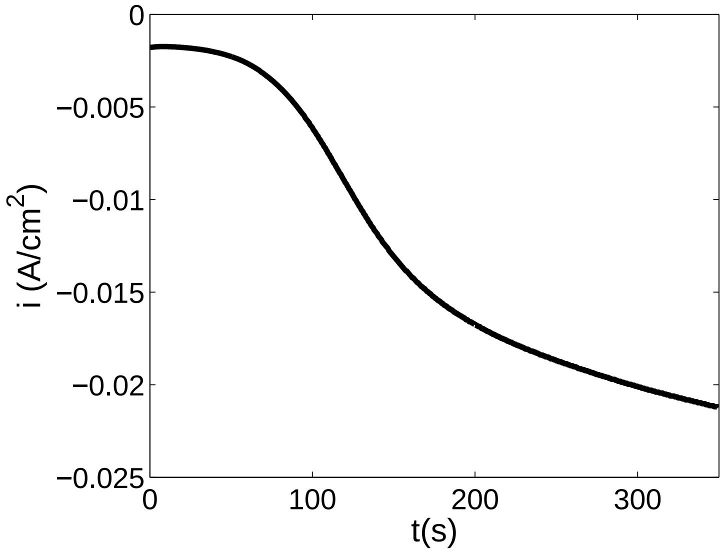

Figure 4.17: Current-time curve obtained after holding the potential at -0.55 V in a series III experiment on which the compositions of solutions 1 and 2 are 1.8 M H_2SO_4+1 mM HCl+88 μM PEG and 0.25 M $CuSO_4$+1.8 M H_2SO_4+1 mM HCl, respectively.

4.4 Discussion

Broadly speaking, the cathodic scans obtained in the presence of PEG and Cl^- fall into one of three categories: *i)* responses similar to those observed in additive-free or Cl^-–only solutions when the PEG concentration is very low, *ii)* strong inhibition at lower overpotentials followed by gradual activation at higher overpotentials when both the PEG and Cl^- concentrations are high and *iii)* strong inhibition at lower overpotentials followed by almost instantaneous activation at a critical overpotential when the PEG and Cl^- concentrations are intermediate. Since the scans were begun at the OCP where the inhibiting film forms, the main process involved can be viewed being the net desorption of the film that automatically re-activates the electrode. Thus, the qualitative differences between the three types of responses described above may be explained in terms of inhibitor desorption.

One of the structures proposed for the inhibiting complex [83, 119, 125, 126] is sketched in Fig. 4.18. Cu^+ is connected to Cl^- on one side and to two ether oxygens in PEG on the other. Regardless of whether or not Cu^+ is considered to be a constituent of the film, it is generally accepted that PEG is tethered to the copper substrate by Cl^-. PEG is formed by a series of repeating monomers -$(CH_2)_2$-O-. The estimated number of these monomers is 77 for the average PEG molecular weight of 3400 used in the experiments of this study. Since more than one pair of oxygens are available from PEG, each PEG can attach to the substrate through more than one Cl^- linkage. Furthermore, the flexibility of a chain should enable its conformation on the surface to change depending on the number of Cl^- linkages, available area on the surface and proximity of other chains. Consequently, the breakage of the links between PEG and the substrate during desorption does not necessarily detach a polymer chain all at once. The conformation of chains remaining on the surface will also change in response to the detachment of other chains. Some of these factors must therefore be considered to explain the differences in electrode responses observed during the scans.

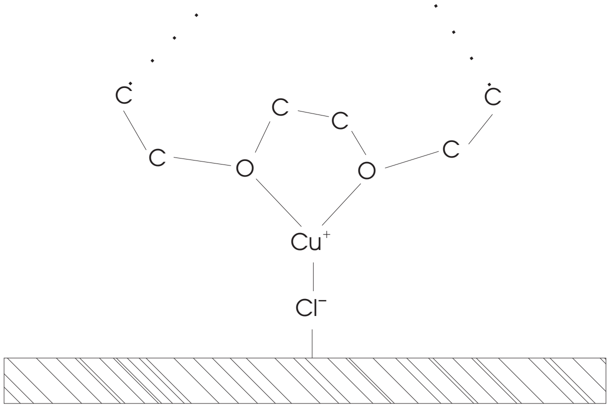

Figure 4.18: Structure for the strongly inhibiting complex formed by PEG, Cl^- and Cu^+ proposed in [83, 119, 125, 126].

Recently, Willey and West [124] presented a qualitative description of PEG desorption from copper as the basis for semi–empirical rate expressions applied to data obtained from the operation of a microfluidic cell under potentiostatic or galvanostatic conditions.

Although their dynamic model is not directly applicable to the experimental conditions of this study, the qualitative picture presented by Willey and West may be quite useful for understanding the various electrode responses observed during the cathodic scans. When PEG saturates the electrode surface, the chains lie neither flat nor on edge, but form a relatively thick layer that completely covers the substrate. When chains begin to detach from the surface, adjacent PEG strands remaining on the surface rearrange themselves so as to cover the sites that have just become exposed. This rearrangement causes the chains to lie flatter over the surface and increase the number of attachment sites. Thus, this stage of desorption is marked by a film that continually grows thinner, but still manages to completely cover the substrate. However, eventually there are no longer enough chains remaining on the surface to completely cover all underlying copper sites. Thus, in the final stage of desorption, more and more metal sites become exposed until all the adsorbed PEG has disappeared.

Each type of electrode response observed during the cathodic scans presumably is marked by a different part of the desorption process. At very low PEG concentrations, the surface is likely not completely covered even at the start of the scan at the OCP. The concentration of Cl^- present also likely plays a particularly important role in promoting inhibition in this situation since a sufficient amount of attachment sites must be available to make most effective use of the inhibitor. The results in Figs. 4.14 and 4.15 suggest that the electrode is not completely saturated at the start of the scan if the Cl^- concentration is below about 0.1 mM when the PEG concentration is between 10 and 100 μM. Also, one might expect that the higher the Cl^- concentration, the flatter the adsorbed PEG would lie over the surface due to more attachment points. In this situation where some underlying copper is exposed, the ratio of the current to that obtained in the absence of PEG will be equal to the fraction of sites not covered by the inhibitor. As the scan and PEG desorption continues, the current will approach the level obtained in a PEG–free system. This approach will be more gradual if the Cl^- concentration and number of attachment sites are high and more rapid at lower Cl^- concentrations.

At high PEG and Cl^- concentrations, the surface is completely saturated and covered at the outset of the scan. The layer is initially thick enough that the electrode is still completely covered by PEG at the end of the scan even after some desorption has occurred.

The gradual increase in current at higher overpotentials occurs because the rate of Cu^{2+} reduction which can still occur across the film to some extent progressively rises as the overpotential increases.

The case of intermediate PEG and Cl^- concentration is interesting because the transition from a completely covered surface (but presumably not saturated) to a partially covered one likely occurs during the scan at the critical potential. Particularly striking is how rapidly and completely the remaining inhibition is lost once the critical potential is passed during the scan. The results in Fig. 4.5 show that the critical potential is not strongly affected by the scan rate, suggesting that an electron transfer process plays a role in the re-activation of the electrode. Two possibilities to explain this behavior are: *i)* detachment of the film occurs directly as an electron transfer reaction and *ii)* detachment is driven by another process that involves electron transfer. If detachment proceeds by the first alternative, this provides indirect support for the contention that Cu^+ is a constituent of the film since it is not obvious how a reduction reaction could break down the complex containing only PEG and Cl^-. Since an inhibiting complex may not be detached by a single reduction event, the first alternative can be expressed by a reaction such as the following

$$PEG(CuCl)_{x(\mathrm{ads})} + e^- \rightarrow Cu^0 + PEG(CuCl)_{x-1(\mathrm{ads})} + Cl^-_{(\mathrm{aq})}. \tag{4.2}$$

where x is the number of linkages to each PEG molecule. Each reaction breaks a linkage of PEG to the electrode and produces copper metal. However, this alternative is less likely than the second one for at least two reasons. Firstly, the slope of the steep rise portions of the curves in Fig. 4.5 are much larger than that expected of a 1-electron or even a 2-electron process described by conventional Butler-Volmer kinetics. Secondly, if desorption begins as soon as the scan begins at the OCP, then this would imply that detachment of PEG can occur by two different processes. A more straightforward and likely scenario is that copper deposition which occurs to some extent throughout the scan has a destabilizing effect on the film. Since this destabilization will allow more metal to deposit, this process has a natural feedback effect that continually reinforces itself and accelerates the disruption of the film.

This type of effect was first recognized by Hebert [130] who proposed a model with the appropriate non–linear mathematical characteristics to describe the transitions between the different types of electrode responses of steady–state current-potential curves. Hebert made a number of simplifying assumptions that effectively de–coupled the material balances for the two additives and allowed him to focus on the effect of Cl^- on the current–potential curves at a fixed PEG concentration. In this model, the metal deposit destabilizes the film by incorporating adsorbed Cl^- as it grows, thereby consuming attachment sites for PEG and causing inhibitor detachment. A key aspect is the competition between the rate at which Cl^- adsorbs on surface sites and the rates at which it desorbs and is incorporated by the growing deposit. A drawback of this model is that it does not include the effects of PEG on the electrode responses. Furthermore, there is not universal agreement from SIMS measurements that Cl^- is actually incorporated within copper deposits [49, 56]. Also, the model was unable to predict the observed responses under transient conditions. A possible modification of this model would be for the depositing metal to displace the inhibiting complex from the surface. Such a model that also explicitly accounts for the effect of PEG and is applicable for transient conditions is presented in Chapter 5.

Although the focus in this section has been on PEG desorption, the ideas presented apply to film formation as well. An interesting observation from Figs. 4.14 and 4.15 of the series II experiments is the change in dynamics of the electrode response as the additives are continually introduced to the solution at fixed potential. The response is relatively slow at lower PEG and Cl^- concentrations, but becomes rapid and dramatic when the point is reached where the film completely covers the electrode and begins to strongly inhibit Cu^{2+} reduction. Such behavior appears to be the reverse of the process that occurs when the critical potential is crossed during the cathodic scans and is likely associated with structural changes in the film as it forms. In the earlier stages of adsorption when the additive concentrations and the number of attached PEG chains are relatively low, the polymer will have some flexibility to its conformation on the surface and so more time may be required before it stabilizes its response to subsequent additions and adsorption of the reagents. However, as more chains become attached to the substrate, they will have fewer degrees of freedom and more rapidly attain a stable response to changes in solution composition. Also, attractive hydrophobic interactions between polymer chains on the surface will begin to play an important role, thereby inducing other chains to attach and accelerating film formation to a rapid conclusion.

The restoration of the inhibiting film during cathodic polarization can occur by the step–by–step re–establishment of the linkages of PEG to the surface. The restoration of the film, as its formation on fresh electrodes, depends on the concentrations of Cl^- and PEG. The results in Fig. 4.7 show that the rate of restoration is slower than that of its formation for the first time presumably since the surface concentrations of Cu^{2+}, Cl^- and PEG after the electrode has been activated have been depleted relative to the bulk levels to some extent. As shown in Fig. 4.11, film restoration will not occur when the concentration of Cl^- is low even in the presence of a sufficient amount of PEG due to the limited number of linkages to re–establish the inhibited film.

Many of the trends shown in Tables 4.3 and 4.4 for series III experiments can also be explained in terms of the relative rates of adsorption and desorption of the film and changes in conformation of the adsorbed PEG chains. After the scan in step 2 begins, any PEG that has been carried over from step 1 will tend to detach. If solution 2 contains no Cl^- (as in the experiments of the second and fourth columns of Table 4.3 and the second and third columns of Table 4.4), inhibition cannot be sustained. If Cl^- and PEG are present in solution 1, but only Cl^- in solution 2, as in experiments 14, 18, 22, 26, 30 and 36, the inhibiting complex can remain adsorbed at the start of the scan. However, since solution 2 contains no PEG, desorption will quickly become dominant and the amount carried over from step 1 will not be large enough to sustain its influence long into the scan. This is presumably due to a point being reached where the PEG molecules adsorbed on the electrode during step 1 cannot further expand and cover the substrate. So, at a potential of about -0.6 V during step 2, any inhibition of Cu^{2+} reduction has disappeared. Only if solution 2 contains sufficient amounts of both PEG and Cl^-, as in the case of experiments 4, 8, 12, 16, 20, 24, 28 and 32, can Cu^{2+} reduction be continually inhibited throughout the scan. Although there would be a net desorption of PEG throughout the scan, the adsorption rate would remain sufficiently high that the electrode remains covered throughout the experiment.

Section 4.1.2 of this chapter included a discussion of the various proposed structures of the inhibiting film and whether Cu^+ is a constituent of this film. The results of these experiments do not provide any direct and unequivocal conclusion on this question. Evidence that PEG and Cl^- can adsorb onto copper in the absence of Cu^{2+} comes from experiments 26, 30 and 36 (Tables 4.3 and 4.4). Although the current study did not obtain direct evidence that a film can form with Cu^+ as a constituent, it is clear that strong inhibition is possible only when copper deposition is occurring in a solution containing PEG and Cl^- as well. This difference suggests that the nature of the film formed in the presence of Cu^{2+} may differ from that formed in its absence. The results of the previous section suggest that an important difference in the films that may form is the ability to inhibit copper deposition. However, the loss of inhibition at large overpotentials in solution 2 of experiments 26 and 30 occurs in the presence of only Cl^- and presumably reflects that there is an insufficient amount of PEG to cover the substrate. Any PEG present during the scan in solution 2 would have come from solution 1 since solution 2 in experiments 26, 30 and 36 did not contain PEG. Thus, it is not possible to conclude definitively whether the difference in inhibition observed in experiments 4, 8, 12, 16, 20, 24, 28 and 32 from that in experiments 26, 30 and 36 is due to an inherent difference in the nature of the adsorbed films formed whether or not is Cu^{2+} is present or simply due to the fact that there is not enough PEG remaining in solution during step 2 in the latter experiments.

Chapter 5

Modeling of Cu Electrodeposition in the Presence of Cl^- and PEG

Previous modeling studies of the kinetics of copper electrodeposition in solutions containing Cl^- and PEG have considered the effect of one of these additives while keeping the concentration of the other additive constant [35, 107]. As discussed in the previous chapter and a number of other studies, the shape of the voltammograms depends strongly on both the PEG and Cl^- concentrations. Current is low at potentials close to the OCP and gradually rises with overpotential in the presence of high PEG and Cl^- concentrations. On the other hand, inhibition of Cu^{2+} reduction is strong at low overpotentials, but then rapidly lost at a critical potential when the additive levels are intermediate. Most previous modeling studies have tended to focus on predicting the electrode responses at high additive concentrations. The only study that has considered the transition between the electrode responses at intermediate and high reagent levels was reported by Hebert [107]. As discussed in the previous chapter, his model includes the effect of Cl^-, but not PEG. It applies only for steady–state conditions and is based on the incorporation of Cl^- by the growing deposit as the crucial factor that destabilizes the film. An objective of this chapter is to relax these restrictions and fit the resulting model to data obtained when both additive concentrations are allowed to vary. A model including mass transfer and kinetics is developed and compared to data obtained from voltammetry and EIS experiments. Also, as with the modeling of additive-free Cu^{2+} reduction, some phenomena are considered that have not been considered in models normally applied to EIS data.

5.1 Background

Although some question has arisen concerning the constituents of the inhibiting complex, Cu^+ has been assumed to be a component of the complex for the purposes of the model development. It turns out that this factor is probably not crucial to the qualitative behavior of the system and that the model could be successfully modified to consider a complex that does not contain Cu^+.

Some mechanisms for the formation of the $\mathrm{Cl^-}$-$\mathrm{Cu^+}$-PEG complex have been previously reported. One of the first proposals was that the formation of a dissolved PEG-$\mathrm{Cu^+}$ complex precedes its attachment to adsorbed $\mathrm{Cl^-}$ [113]. Other researchers suggest that $\mathrm{Cu^+}$-$\mathrm{Cl^-}$ is formed first on the surface before PEG attaches to it [31, 83], *i.e.*,

$$CuCl_{\mathrm{(ads)}} + PEG_{\mathrm{(aq)}} \rightarrow CuClPEG_{\mathrm{(ads)}}. \tag{5.1}$$

The formation of the $\mathrm{CuCl_{(ads)}}$ species in reaction (5.1) has been proposed to occur via the following consecutive reactions [110]:

$$Cu^{2+}_{\mathrm{(aq)}} + e^- \rightarrow Cu(I)_{\mathrm{(ads)}}, \tag{5.2}$$

$$Cl^-_{\mathrm{(aq)}} + Cu(I)_{\mathrm{(ads)}} \rightarrow CuCl_{\mathrm{(ads)}}. \tag{5.3}$$

This mechanism can explain the loss of inhibition at high overpotentials by including the reaction

$$Cu(I)_{\mathrm{(ads)}} + e^- \rightarrow Cu^0_{\mathrm{(s)}}. \tag{5.4}$$

which occurs preferentially to (5.3) under these conditions. A different study suggests that Cu(I) participating in reaction (5.3) can be formed at OCP via the comproportionation reaction [5]

$$Cu^{2+}_{\mathrm{(aq)}} + Cu^0_{\mathrm{(s)}} \rightarrow 2Cu(I). \tag{5.5}$$

However, this proposal does not explain the formation of the inhibiting complex at cathodic potentials. As shown in Figs. 4.8 and 4.9 of the previous chapter, the inhibiting complex can form over a wide range of overpotentials at high PEG and $\mathrm{Cl^-}$ concentrations and at overpotentials above the critical potentials at lower reagent levels. An alternative reaction for the formation of $\mathrm{CuCl}_{(\mathrm{ads})}$ involved in the formation of the Cl^--Cu^+-PEG complex at cathodic potentials that has been proposed is [31]

$$Cu^{2+}_{(\mathrm{aq})} + Cl^{-}_{(\mathrm{aq})} + e^- \rightarrow CuCl_{(\mathrm{ads})}. \tag{5.6}$$

Once reaction (5.6) proceeds, PEG attaches to $\mathrm{CuCl}_{(\mathrm{ads})}$ by means of reaction (5.1) to form the inhibiting complex.

Two different roles have been assigned to the inhibiting complex during copper electrodeposition: *i)* blockage of the sites available for the reduction of Cu^{2+} and *ii)* intermediate for the deposition of copper. The second role implies that Cu^+ necessarily forms part of the inhibiting complex. Some researchers have suggested that the inhibiting complex only blocks the substrate and does not participate as an intermediate in the Cu^{2+} reduction mechanism [35, 107, 108, 130, 131]. Other researchers propose that the complex fulfills both inhibiting and intermediate roles since it can be continually re–formed during cathodic polarization [31].

In various models, the fractional coverage of PEG on the surface has been obtained taking into account its adsorption, desorption and incorporation into the deposit [105, 107, 131]. Also, the coverage of PEG has been estimated from its value at equilibrium or steady state conditions [35, 107]. In another study, the coverage of PEG was estimated from the fractional coverage of Cl^- [130].

Some of the mechanisms described above have been used in physicochemical models that have been fitted to data obtained at steady state conditions or from voltammetry and impedance measurements [31, 35, 107, 130, 131]. Most of these studies apply to cases where high concentrations of Cl^- and PEG are used. At these conditions, the inhibition is strong over a wide range of potentials as explained in Chapter 4. Only the model proposed by Hebert [130] has been able to predict the sudden loss of inhibition observed when the concentration of Cl^- decreases. However, as mentioned in section 4.4, this model assumes incorporation of Cl^- which is not generally accepted in previous studies [49, 56]. Also, this model was successful when steady state polarization was considered, but could not be extended to transient conditions that would apply during voltammetry and EIS experiments.

The model presented in this chapter relies on the idea that the deposition of copper displaces the adsorbed complex from the surface. Also, as mentioned at the outset of this chapter, the model presented here explicitly accounts for the effects of Cl^- and PEG, considers transient conditions and builds upon the model presented in Chapter 3.

5.2 Experimental

The reagents, materials and preparation of the working electrode for these experiments are unchanged from that described in section 4.2. In all the solutions tested, the $CuSO_4$ and H_2SO_4 concentrations were maintained at 0.25 M and 1.8 M, respectively. The concentrations of Cl^- and PEG present in the solutions used for the purposes of fitting for the model parameters are given in the second and third columns of Table 5.1. The current–potential data were obtained from voltammetry scans from the OCP to -0.9 V at a sweep rate of 2 mV/s. Only scans proceeding in the cathodic direction are used for the purposes of obtaining the kinetic parameters. These conditions were chosen to ensure that the three types of electrode responses discussed in Chapter 4 were used. The potentiostatic electrochemical impedance spectra were obtained at the base potentials given in the last column of Table 5.1. EIS experiments were conducted for solution compositions of 0.01 mM HCl+50 μM PEG and 0.1 mM HCl+10 μM PEG at potentials negative with respect to the critical potential. For the solution containing 1 mM HCl+ 50 μM PEG, the EIS experiment was conducted at -0.7 V where Cu^{2+} reduction is partially inhibited. In each experiment, sinusoidal oscillations with amplitude 1% of the value of the base potential were applied over a frequency range from 65000 to 0.05Hz.

Table 5.1: Experimental conditions.

Experiment	[HCl], mM	[PEG], μM,	$\overline{E}$, V vs MSE
1	0.001	10	-0.65
2	0.01	50	-0.65
3	0.1	10	-0.75
4	1	50	-0.7

5.3 Model Development

In this section, the mass transport equations of the model are presented first, followed by the rate expressions for kinetics at the electrode surface during Cu^{2+} reduction. The kinetics of Cu^{2+} reduction is assumed to be different depending on the coverage of the electrode by PEG: *i)* mechanism when the surface is completely covered with the inhibiting complex and *ii)* mechanism when there is only partial coverage. As discussed below, the first condition tends to hold at high additive concentrations or intermediate concentrations and low overpotentials. The second condition applies for low and intermediate additive concentrations and high overpotentials.

5.3.1 Mass Transport Equations

Since migration was found to have little effect on the results in Section 3.4.4 and the additive concentrations are very low, it is not considered in the mass balance equations for Cu^{2+}, Cl^- and PEG. The model was further simplified by neglecting the homogeneous reactions

$$CuSO_{4\mathrm{(aq)}} \overset{K'}{\rightleftharpoons} Cu^{2+}_{\mathrm{(aq)}} + SO^{2-}_{4\mathrm{(aq)}}, \tag{5.7}$$

$$HSO^{-}_{4\mathrm{(aq)}} \overset{K''}{\rightleftharpoons} H^{+}_{\mathrm{(aq)}} + SO^{2-}_{4\mathrm{(aq)}}. \tag{5.8}$$

With the latter change, the portion of the model not involving additives was re–fit to the additive–free data of Chapter 3 to obtain a new set of parameters for this portion of the mechanism, as discussed later in Section 5.3.4. Thus, the mass balance equations for species Cu^{2+}, Cl^- and PEG take the following form:

$$\frac{\partial C_i}{\partial t} = D_i \frac{\partial^2 C_i}{\partial z^2} - \upsilon_z \frac{\partial C_i}{\partial z} \qquad on \quad 0 < z < 3\delta, \tag{5.9}$$

where δ is given by Eq. (3.1) and υ_z is given by the expression

$$\upsilon_z = -0.51023\,\Omega^{\frac{3}{2}} \nu^{-\frac{1}{2}} z^2. \tag{5.10}$$

The boundary conditions are written as follows

$$C_i = C_i^{\mathrm{b}} \qquad\qquad at \quad z = 3\delta. \tag{5.11}$$

$$D_i \frac{\partial C_i}{\partial z} = r_{net} \qquad\qquad at \quad z = 0. \tag{5.12}$$

where r_{net} is the net rate at which the species i is consumed at the surface. The total current density and electrode potential corrected for the solution resistance are given by the following expressions

$$i = i_{\mathrm{f}} + C_{\mathrm{dl}}\frac{\partial E'}{\partial t}, \tag{5.13}$$

$$E' = E - iR_{\mathrm{s}}. \tag{5.14}$$

The potential E in Eq. (5.14) is calculated for voltammetry conditions from the applied sweep rate ϑ and the initial potential E_0 as follows

$$E = E_0 - \vartheta t. \tag{5.15}$$

The initial conditions for the voltammetry experiments are:

$$C_i(z,0) = C_i^{\mathrm{b}}, \qquad \qquad on \quad 0 < z < 3\delta. \tag{5.16}$$

5.3.2 Kinetics of Cu^{2+} Reduction in the Presence of Cl^{-}+PEG

As discussed in section 4.4, the concentrations of Cl^- and PEG and the applied potential determine the extent of Cu^{2+} reduction inhibition. To describe the different extents of inhibition observed in the voltammetry scans, the model must account for the various adsorbed species and the conditions corresponding to complete or incomplete coverage by the inhibiting film. Three adsorbed species are envisaged to exist: $Cu(I)_{(ads)}$, $CuCl_{(ads)}$ and $ClCuPEG_{(ads)}$. Due to its size and flexibility, $ClCuPEG_{(ads)}$ generally extends out from the surface and can change the electrode area it covers during the process. Consequently, the extent of adsorption of this species is described differently than the other two. The coverage of the electrode by PEG is defined in terms of the adsorption density Γ_p expressed as moles per unit area of the substrate. The coverages of other adsorbed species $Cu(I)_{(ads)}$ and $CuCl_{(ads)}$ are expressed in terms of the fraction of the electrode surface area they occupy beneath the adsorbed PEG layer and are denoted as θ_{Cu} and θ_{Clc}, respectively. The adsorption density of PEG is marked by two critical values. Since each adsorbed PEG is attached to the surface by at least one Cl^-, the saturated adsorption density Γ_s represents the maximum possible amount of inhibitor on the surface. The minimum adsorption density of ClCuPEG to completely cover the surface is denoted by Γ_0. The surface will remain completely covered at adsorption densities between Γ_0 and Γ_s due to the ability of PEG to change its conformation on the surface as discussed in Chapter 4 and proposed by Willey and West [124]. At high concentrations of Cl^- and PEG, the strong suppression of Cu^{2+} reduction at low overpotentials followed by a gradual current rise at higher overpotentials suggests that the substrate is completely covered throughout the scan. When the substrate is completely covered, copper still is able to deposit across the film. Under this condition, the deposition of copper is assumed to proceed at a low rate proportional to that obtained under PEG-free conditions. At lower additive concentrations, a point will be reached during a cathodic scan where Γ_p falls below Γ_0 and bare metal sites will become exposed. Since copper will preferentially deposit on these sites, the overall rate of copper deposition will be proportional to the fraction of bare sites when $\Gamma_p < \Gamma_0$.

The model is intended to be robust and describe the conditions for a wide range of PEG and Cl^- concentrations, including the acceleration of Cu^{2+} reduction in the presence of Cl^- alone. Thus, copper electrodeposition is envisaged to proceed via two pathways: one involving $Cu(I)_{(ads)}$ as the intermediate, similar to the situation of the additive–free case and the second one with $CuCl_{(ads)}$ as the intermediate, *i.e.*,

$$1. \qquad Cu^{2+}_{(\mathrm{aq})} + e^- \xrightarrow{k_1} Cu(I)_{(\mathrm{ads})}, \tag{5.17}$$

$$Cu(I)_{(\mathrm{ads})} + e^- \underset{k_{-2}}{\overset{k_2}{\rightleftharpoons}} Cu^0_{(\mathrm{s})}, \tag{5.18}$$

and

$$2. \qquad Cu^{2+}_{(\mathrm{aq})} + Cl^-_{(\mathrm{aq})} + e^- \xrightarrow{k_3} CuCl_{(\mathrm{ads})}, \tag{5.19}$$

$$CuCl_{(\mathrm{ads})} + e^- \xrightarrow{k_4} Cu^0 + Cl^-_{(\mathrm{aq})}. \tag{5.20}$$

In the absence of PEG and Cl^- the mechanism simplifies to that of additive–free deposition. When the solution contains Cl^-, but little or no PEG, pathway 2 becomes dominant and so the mechanism may be capable of predicting acceleration of Cu^{2+} reduction. The backward rate of reaction (5.17) is neglected based on the results of section 3.4.3 that showed it has no effect on the electrode response under conditions of cathodic polarization. The backward rate of reaction (5.20) is also neglected based on observations from SIMS analysis that little Cl^- is present on the surface of copper deposits produced in Cl^-–containing solutions [56].

The inhibiting complex is formed from PEG combining with $CuCl_{(ads)}$ according to the following chemical process:

$$PEG_{\text{(aq)}} + CuCl_{\text{(ads)}} \rightarrow ClCuPEG_{\text{(ads)}}, \tag{5.21}$$

If reaction (5.19) is combined with reaction (5.21), the overall process by which ClCuPEG is formed involves electron transfer.

A key aspect of the proposed model is that deposited metal can displace ClCuPEG$_{(ads)}$ from the surface. Furthermore, for simplicity, the products generated by the desorption of the inhibiting complex are assumed to have no effect on the process. Thus, there is no need to identify the products and so the desorption reaction can be written as:

$$ClCuPEG_{\text{(ads)}} \xrightarrow{k_6} Products. \tag{5.22}$$

The complex is therefore considered to be primarily a barrier to Cu^{2+} reduction rather than an intermediate.

When $\Gamma_p < \Gamma_0$, Cu^{2+} reduction occurs preferentially on metal sites directly exposed to the solution. Under this condition, the conformation of PEG no longer changes since it has stretched to its limit and the maximum adsorption density of ClCuPEG on the surface is given by Γ_0. The fraction of surface sites covered by the complex is then Γ_p/Γ_0. Thus, the fraction of empty sites is $(1 - \theta_{Cu} - \theta_{Clc} - \Gamma_p/\Gamma_0)$ and reactions (5.17)–(5.20) have the following rates:

$$\Gamma_p < \Gamma_0 :$$

$$r_1 = k_1 \text{exp}\left(-\beta_1 \frac{FE'}{RT}\right) C^{\text{s}}_{Cu} \left(1 - \theta_{Cu} - \theta_{Clc} - \frac{\Gamma_p}{\Gamma_0}\right), \tag{5.23}$$

$$r_2 = k_2 \text{exp}\left(-\beta_2 \frac{FE'}{RT}\right) \theta_{Cu} - k_{-2} \text{exp}\left((1-\beta_2) \frac{FE'}{RT}\right) \left(1 - \theta_{Cu} - \theta_{Clc} - \frac{\Gamma_p}{\Gamma_0}\right), \tag{5.24}$$

$$r_3 = k_3 \text{exp}\left(-\beta_3 \frac{FE'}{RT}\right) C^{\text{s}}_{Cu} C^{\text{s}}_{Cl} \left(1 - \theta_{Cu} - \theta_{Clc} - \frac{\Gamma_p}{\Gamma_0}\right), \tag{5.25}$$

$$r_4 = k_4 \text{exp}\left(-\beta_4 \frac{FE'}{RT}\right) \theta_{Clc}, \tag{5.26}$$

where β_1, β_2, β_3 and β_4 are charge transfer coefficients, k_1, k_2, k_{-2}, k_3 and k_4 are rate constants and C^s_{Cu} and C^s_{Cl} are the surface concentrations of Cu^{2+} and Cl$^-$, respectively. The adsorption rate of PEG via reaction (5.21) is proportional to θ_{Clc} since PEG can adsorb only on CuCl$_{\text{(ads)}}$ sites. It should be noted that once PEG adsorbs by reaction (5.21), the

$\mathrm{CuCl_{(ads)}}$ involved no longer contributes to θ_{Clc}. The rate of reaction (5.21) describing the rate of PEG adsorption is given by:

$$\Gamma_p < \Gamma_0 : \qquad r_5 = k_5 C_P^{\mathrm{s}} \theta_{Clc}, \tag{5.27}$$

where k_5 is a rate constant. The desorption of PEG is considered to occur by the action of copper metal formation by reactions (5.18) and (5.20). Furthermore, the very steep rise in current due to inhibiting film breakdown in cathodic scans such as those shown in Figs. 4.3 and 4.4 suggest that the complex offers little resistance to the displacing action of copper metal formation. Thus, the desorption is assumed to be driven by metal formation and so its rate is proportional to the term $r_2 + r_4$ scaled to the amount of adsorbed PEG present. The rate of reaction (5.22) is then given by the following expression:

$$\Gamma_p < \Gamma_0 : \qquad r_6 = k_6 (r_2 + r_4) \Gamma_p, \tag{5.28}$$

where k_6 is a rate constant.

If the surface is completely covered by the inhibiting film ($\Gamma_p \geq \Gamma_0$), the rate of reduction of $\mathrm{Cu^{2+}}$ is considered to be retarded from that observed under PEG–free conditions by a factor k_7. k_7 represents a fraction of the electrode area that is occupied by holes in the PEG film. $(1 - \theta_{Cu} - \theta_{Clc})$ is the fraction of bare sites underneath the PEG layer. The following expressions for reactions (5.17)–(5.20) result:

$$\Gamma_p \geq \Gamma_0 :$$

$$r_1 = k_7\, k_1 \exp\left(-\beta_1 \frac{FE'}{RT}\right) C_{Cu}^{\mathrm{s}} (1 - \theta_{Cu} - \theta_{Clc}), \tag{5.29}$$

$$r_2 = k_7\, k_2 \exp\left(-\beta_2 \frac{FE'}{RT}\right) \theta_{Cu} - k_7\, k_{-2} \exp\left((1 - \beta_2) \frac{FE'}{RT}\right) (1 - \theta_{Cu} - \theta_{Clc}), \tag{5.30}$$

$$r_3 = k_7\, k_3 \exp\left(-\beta_3 \frac{FE'}{RT}\right) C_{Cu}^{\mathrm{s}} C_{Cl}^{\mathrm{s}} (1 - \theta_{Cu} - \theta_{Clc}), \tag{5.31}$$

$$r_4 = k_7\, k_4 \exp\left(-\beta_4 \frac{FE'}{RT}\right) \theta_{Clc}, \tag{5.32}$$

The rate constants k_1, k_2, k_{-2}, k_3 and k_4 and transfer coefficients β_1, β_2, β_3 and β_4 are the same as those that apply when $\Gamma_p < \Gamma_0$. Each of Eqs. (5.29)–(5.32) corresponds to the rate for one of the reaction steps (5.17)–(5.20) in a PEG–free solution multiplied by the retardation factor k_7. Eqs. (5.29) and (5.31) express that $\mathrm{Cu^{2+}}$ reacts on bare metal sites beneath the adsorbed inhibitor layer at a rate retarded by the factor k_7.

The adsorption rate of PEG via the reaction (5.21) depends on the fraction of available sites given by $\theta_{Clc}(\Gamma_s - \Gamma_p)$. The $\Gamma_s - \Gamma_p$ term gives the number of additional PEG that can adsorb until saturation is reached. The rates of reactions (5.21) and (5.22) are given by the following expressions:

$$\Gamma_p \geq \Gamma_0 :$$

$$r_5 = k_8 C_P^{\mathrm{s}} \theta_{Clc}(\Gamma_s - \Gamma_p), \tag{5.33}$$

$$r_6 = k_6(r_2 + r_4)\Gamma_p, \tag{5.34}$$

where k_8 is a rate constant.

The faradaic current density is related to the reaction rates for both conditions $\Gamma_p < \Gamma_0$ and $\Gamma_p \geq \Gamma_0$:

$$i_{\mathrm{f}} = -F(r_1 + r_2 + r_3 + r_4). \tag{5.35}$$

Molar balances for the adsorbed species are given by:

$$\Gamma_{Cu}\frac{\partial \theta_{Cu}}{\partial t} = r_1 - r_2, \tag{5.36}$$

$$\Gamma_{Clc}\frac{\partial \theta_{Clc}}{\partial t} = r_3 - r_4 - r_5, \tag{5.37}$$

$$\frac{\partial \Gamma_p}{\partial t} = r_5 - r_6, \tag{5.38}$$

where Γ_{Cu} and Γ_{Clc} denote the maximum adsorption densities of a monolayer of Cu(I) and CuCl on the surface, respectively.

As discussed in Chapter 4, the ability of the model to predict both the smooth rise in current at low and high additive concentrations and the abrupt activation of the electrode response at intermediate additive levels is tied closely to the mathematical structure of the rate expressions describing electrode kinetics. Although they must be non–linear and account for the competition between adsorption and desorption of the inhibiting complex, a key aspect is the mathematical form of the desorption rate (*i.e.*, Eqs. (5.28) and (5.34)). By involving the product of $r_2 + r_4$ by Γ_P, it provides a mechanism by which a feedback effect operates on film destabilization that continually reinforces itself and accelerates film desorption, *i.e.*, film disruption leads to an increase in metal deposition which in turn speeds up desorption. A number of alternative models were formulated with mechanisms in which the desorption rate did not involve a product of the metal deposition rate and Γ_P. None of these was able to successfully predict the types of electrode responses observed at low, intermediate and high PEG and Cl$^-$ concentrations. Another key aspect is that the model accounts for a distinction between the conditions corresponding to a complete and incomplete coverage of the electrode surface by the inhibiting film.

5.3.3 Linearization

The linearized expressions to determine the impedance are presented in this section.

Zeroth Order Solution

As shown in Chapter 3, the zeroth order problem corresponds to steady state conditions. The individual zeroth order mass transport equations are obtained from Eq. (5.9) using the same approach presented in section 3.3.3:

$$D_i \frac{\partial^2 \overline{C}_i}{\partial z^2} - \upsilon_z \frac{\partial \overline{C}_i}{\partial z} = 0 \qquad on \quad 0 < z < 3\delta, \tag{5.39}$$

where i is either Cu^{2+}, Cl^- or PEG. The boundary conditions at the outer edge of the transport layer are:

$$\overline{C}_i = C_i^{\mathrm{b}} \qquad at \quad z = 3\delta, \tag{5.40}$$

The boundary conditions at the electrode surface are given by the following set of equations:

$$D_{Cu} \frac{\partial \overline{C}_{Cu}}{\partial z} = \overline{r}_1 + \overline{r}_3 \qquad at \quad z = 0. \tag{5.41}$$

$$D_{Cl} \frac{\partial \overline{C}_{Cl}}{\partial z} = \overline{r}_3 - \overline{r}_4 \qquad at \quad z = 0. \tag{5.42}$$

$$D_P \frac{\partial \overline{C}_P}{\partial z} = \overline{r}_5 \qquad at \quad z = 0. \tag{5.43}$$

$\overline{r}_1$, $\overline{r}_3$, $\overline{r}_4$ and $\overline{r}_5$ are calculated from Eqs. (5.23) and (5.25)–(5.27) if $\Gamma_p < \Gamma_0$ or Eqs. (5.29) and (5.31)–(5.33) if $\Gamma_p \geq \Gamma_0$, and the following expressions:

$$\overline{i} = -F(\overline{r}_1 + \overline{r}_2 + \overline{r}_3 + \overline{r}_4), \tag{5.44}$$

$$\overline{r}_1 - \overline{r}_2 = 0, \tag{5.45}$$

$$\overline{r}_3 - \overline{r}_4 - \overline{r}_5 = 0, \tag{5.46}$$

$$\overline{r}_5 - \overline{r}_6 = 0, \tag{5.47}$$

Eqs. (5.45)–(5.47) are obtained by setting the transient balance equations (5.36)–(5.38) for the adsorbed species to steady state conditions.

First Order Solution

The first–order mass balance for each species Cu^{2+}, Cl^{-} and PEG is obtained from Eq. A.5 after neglecting the migration and homogeneous reaction terms, *i.e.*,

$$\mathrm{j}\omega\widetilde{C}_i = D_i\frac{\mathrm{d}^2\widetilde{C}_i}{\mathrm{d}z^2} - v_z\frac{\mathrm{d}\widetilde{C}_i}{\mathrm{d}z} \qquad \textit{on} \quad 0 < z < 3\delta. \tag{5.48}$$

The conditions at the outer edge of the transport layer are:

$$\widetilde{C}_i = 0 \qquad\qquad \textit{at} \quad z = 3\delta. \tag{5.49}$$

The conditions at the electrode surface are:

$$D_{Cu}\frac{\partial\widetilde{C}_{Cu}}{\partial z} = \widetilde{r}_1 + \widetilde{r}_3 \qquad\qquad \textit{at} \quad z = 0. \tag{5.50}$$

$$D_{Cl}\frac{\partial\widetilde{C}_{Cl}}{\partial z} = \widetilde{r}_3 - \widetilde{r}_4 \qquad\qquad \textit{at} \quad z = 0. \tag{5.51}$$

$$D_{P}\frac{\partial\widetilde{C}_{P}}{\partial z} = \widetilde{r}_5 \qquad\qquad \textit{at} \quad z = 0. \tag{5.52}$$

Expressions for $\widetilde{r}_1$, $\widetilde{r}_2$, $\widetilde{r}_3$, $\widetilde{r}_4$, $\widetilde{r}_5$ and $\widetilde{r}_6$ obtained as Eqs. (A.62)–(A.72) in Appendix A are:

For the condition $\Gamma_p < \Gamma_0$:

$$\begin{aligned}
\widetilde{r}_1 = {} & \left[-\beta_1\frac{F}{RT}k_1\exp\left(-\beta_1\frac{F\overline{E}'}{RT}\right)\overline{C}^{\mathrm{s}}_{Cu}\left(1-\overline{\theta}_{Cu}-\overline{\theta}_{Clc}-\frac{\overline{\Gamma}_p}{\Gamma_0}\right)\right]\widetilde{E}' \\
& + \left[k_1\exp\left(-\beta_1\frac{F\overline{E}'}{RT}\right)\left(1-\overline{\theta}_{Cu}-\overline{\theta}_{Clc}-\frac{\overline{\Gamma}_p}{\Gamma_0}\right)\right]\widetilde{C}^{\mathrm{s}}_{Cu} \\
& - \left[k_1\exp\left(-\beta_1\frac{F\overline{E}'}{RT}\right)\overline{C}^{\mathrm{s}}_{Cu}\right]\left(\widetilde{\theta}_{Cu}+\widetilde{\theta}_{Clc}+\frac{1}{\Gamma_0}\widetilde{\Gamma}_p\right),
\end{aligned} \tag{5.53}$$

$$\begin{aligned}
\widetilde{r}_2 = {} & \left[-\beta_2\frac{F}{RT}k_2\exp\left(-\beta_2\frac{F\overline{E}'}{RT}\right)\overline{\theta}_{Cu}\right]\widetilde{E}' \\
& - \left[(1-\beta_2)\frac{F}{RT}k_{-2}\exp\left((1-\beta_2)\frac{F\overline{E}'}{RT}\right)\left(1-\overline{\theta}_{Cu}-\overline{\theta}_{Clc}-\frac{\overline{\Gamma}_p}{\Gamma_0}\right)\right]\widetilde{E}'
\end{aligned}$$

$$\begin{aligned}
&+\left[k_2 \exp\left(-\beta_2 \frac{F\overline{E}'}{RT}\right) + k_{-2} \exp\left((1-\beta_2)\frac{F\overline{E}'}{RT}\right)\right] \widetilde{\theta}_{Cu} \\
&+\left[k_{-2} \exp\left((1-\beta_2)\frac{F\overline{E}'}{RT}\right)\right] \left(\widetilde{\theta}_{Clc} + \frac{1}{\Gamma_0}\widetilde{\Gamma}_p\right),
\end{aligned} \tag{5.54}$$

$$\begin{aligned}
\widetilde{r}_3 = &\left[-\beta_3 \frac{F}{RT} k_3 \exp\left(-\beta_3 \frac{F\overline{E}'}{RT}\right) \overline{C}^{s}_{Cu} \overline{C}^{s}_{Cl} \left(1 - \overline{\theta}_{Cu} - \overline{\theta}_{Clc} - \frac{\overline{\Gamma}_p}{\Gamma_0}\right)\right] \widetilde{E}' \\
&+\left[k_3 \exp\left(-\beta_3 \frac{F\overline{E}'}{RT}\right) \left(1 - \overline{\theta}_{Cu} - \overline{\theta}_{Clc} - \frac{\overline{\Gamma}_p}{\Gamma_0}\right)\right] \left(\overline{C}^{s}_{Cl} \widetilde{C}^{s}_{Cu} + \overline{C}^{s}_{Cu} \widetilde{C}^{s}_{Cl}\right) \\
&-\left[k_3 \exp\left(-\beta_3 \frac{F\overline{E}'}{RT}\right) \overline{C}^{s}_{Cu} \overline{C}^{s}_{Cl}\right] \left(\widetilde{\theta}_{Cu} + \widetilde{\theta}_{Clc} + \frac{1}{\Gamma_0}\widetilde{\Gamma}_p\right),
\end{aligned} \tag{5.55}$$

$$\begin{aligned}
\widetilde{r}_4 = &\left[-\beta_4 \frac{F}{RT} k_4 \exp\left(-\beta_4 \frac{F\overline{E}'}{RT}\right) \overline{\theta}_{Clc}\right] \widetilde{E}' \\
&+\left[k_4 \exp\left(-\beta_4 \frac{F\overline{E}'}{RT}\right)\right] \widetilde{\theta}_{Clc},
\end{aligned} \tag{5.56}$$

$$\widetilde{r}_5 = \left[k_5 \overline{\theta}_{Clc}\right] \widetilde{C}^{s}_{P} + \left[k_5 \overline{C}^{s}_{P}\right] \widetilde{\theta}_{Clc}, \tag{5.57}$$

$$\widetilde{r}_6 = \left[k_6 \overline{\Gamma}_p\right] \left(\widetilde{r}_2 + \widetilde{r}_4\right) + \left[k_6 \left(\overline{r}_2 + \overline{r}_4\right)\right] \widetilde{\Gamma}_p. \tag{5.58}$$

For the condition $\Gamma_p \geq \Gamma_0$:

$$\begin{aligned}
\widetilde{r}_1 = &\left[-\beta_1 \frac{F}{RT} k_7\ k_1 \exp\left(-\beta_1 \frac{F\overline{E}'}{RT}\right) \overline{C}^{s}_{Cu} (1 - \overline{\theta}_{Cu} - \overline{\theta}_{Clc})\right] \widetilde{E}' \\
&+\left[k_7\ k_1 \exp\left(-\beta_1 \frac{F\overline{E}'}{RT}\right) (1 - \overline{\theta}_{Cu} - \overline{\theta}_{Clc})\right] \widetilde{C}^{s}_{Cu} \\
&-\left[k_7\ k_1 \exp\left(-\beta_1 \frac{F\overline{E}'}{RT}\right) \overline{C}^{s}_{Cu}\right] \left(\widetilde{\theta}_{Cu} + \widetilde{\theta}_{Clc}\right),
\end{aligned} \tag{5.59}$$

$$\begin{aligned}
\widetilde{r}_2 = &\left[-\beta_2 \frac{F}{RT} k_7\ k_2 \exp\left(-\beta_2 \frac{F\overline{E}'}{RT}\right) \overline{\theta}_{Cu}\right] \widetilde{E}' \\
&-\left[(1-\beta_2) \frac{F}{RT} k_7\ k_{-2} \exp\left((1-\beta_2) \frac{F\overline{E}'}{RT}\right) (1 - \overline{\theta}_{Cu} - \overline{\theta}_{Clc})\right] \widetilde{E}'
\end{aligned}$$

$$
\begin{aligned}
&+ \left[k_7\, k_2 \exp\left(-\beta_2 \frac{F\overline{E}'}{RT}\right) + k_7\, k_{-2} \exp\left((1-\beta_2)\frac{F\overline{E}'}{RT}\right)\right] \widetilde{\theta}_{Cu} \\
&+ \left[k_7\, k_{-2} \exp\left((1-\beta_2)\frac{F\overline{E}'}{RT}\right)\right] \widetilde{\theta}_{Clc},
\end{aligned}
\tag{5.60}
$$

$$
\begin{aligned}
\widetilde{r}_3 = {} & \left[-\beta_3 \frac{F}{RT} k_7\, k_3 \exp\left(-\beta_3 \frac{F\overline{E}'}{RT}\right) \overline{C}^{\mathrm{s}}_{Cu} \overline{C}^{\mathrm{s}}_{Cl} (1-\overline{\theta}_{Cu}-\overline{\theta}_{Clc})\right] \widetilde{E}' \\
&+ \left[k_7\, k_3 \exp\left(-\beta_3 \frac{F\overline{E}'}{RT}\right)(1-\overline{\theta}_{Cu}-\overline{\theta}_{Clc})\right] \left(\overline{C}^{\mathrm{s}}_{Cl}\widetilde{C}^{\mathrm{s}}_{Cu} + \overline{C}^{\mathrm{s}}_{Cu}\widetilde{C}^{\mathrm{s}}_{Cl}\right) \\
&- \left[k_7\, k_3 \exp\left(-\beta_3 \frac{F\overline{E}'}{RT}\right) \overline{C}^{\mathrm{s}}_{Cu}\overline{C}^{\mathrm{s}}_{Cl}\right] \left(\widetilde{\theta}_{Cu} + \widetilde{\theta}_{Clc}\right),
\end{aligned}
\tag{5.61}
$$

$$
\begin{aligned}
\widetilde{r}_4 = {} & \left[-\beta_4 \frac{F}{RT} k_7\, k_4 \exp\left(-\beta_4 \frac{F\overline{E}'}{RT}\right) \overline{\theta}_{Clc}\right] \widetilde{E}' \\
&+ \left[k_7\, k_4 \exp\left(-\beta_4 \frac{F\overline{E}'}{RT}\right)\right] \widetilde{\theta}_{Clc},
\end{aligned}
\tag{5.62}
$$

$$
\widetilde{r}_5 = \left[k_8 \overline{\theta}_{Clc}(\Gamma_s - \overline{\Gamma}_p)\right] \widetilde{C}^{\mathrm{s}}_P + \left[k_8 \overline{C}^{\mathrm{s}}_P (\Gamma_s - \overline{\Gamma}_p)\right] \widetilde{\theta}_{Clc} - \left[k_8 \overline{C}^{\mathrm{s}}_P \overline{\theta}_{Clc}\right] \widetilde{\Gamma}_p,
\tag{5.63}
$$

$$
\widetilde{r}_6 = \left[k_6 \overline{\Gamma}_p\right] (\widetilde{r}_2 + \widetilde{r}_4) + \left[k_6\,(\overline{r}_2 + \overline{r}_4)\right] \widetilde{\Gamma}_p.
\tag{5.64}
$$

where

$$
\widetilde{E}' = \widetilde{E} - \widetilde{i} R_{\mathrm{s}},
\tag{5.65}
$$

$$
\Gamma_{Cu} \mathrm{j}\omega \widetilde{\theta}_{Cu} = \widetilde{r}_1 - \widetilde{r}_2,
\tag{5.66}
$$

$$
\Gamma_{Clc} \mathrm{j}\omega \widetilde{\theta}_{Clc} = \widetilde{r}_3 - \widetilde{r}_4 - \widetilde{r}_5,
\tag{5.67}
$$

$$
\mathrm{j}\omega \widetilde{\Gamma}_P = \widetilde{r}_5 - \widetilde{r}_6,
\tag{5.68}
$$

$$
\widetilde{i} = \widetilde{i}_{\mathrm{f}} + \widetilde{i}_{\mathrm{dl}} = -F(\widetilde{r}_1 + \widetilde{r}_2 + \widetilde{r}_3 + \widetilde{r}_4) + C_{\mathrm{dl}}\, j\, \omega\, \widetilde{E}'.
\tag{5.69}
$$

The impedance is calculated with the following equation

$$
Z = \frac{\widetilde{E}}{\widetilde{i}}.
\tag{5.70}
$$

5.3.4 Computational Implementation

Similar to the procedure used in Chapter 3, the *bvp4c MATLAB* routine was used to solve the zeroth and first order problems and obtain the impedance data. The voltammetry data was obtained by discretizing the derivatives with respect to the spatial variable z. The discretization was performed by using a mesh with 49 interior node points within the boundary layer and the following finite difference formulas [132]:

$$\left.\frac{\partial^2 y}{\partial z^2}\right|_{z=z_d} = \frac{y(t, z_{d+1}) - 2y(t, z_d) + y(t, z_{d-1})}{h^2} \qquad for\ 2 < d < 50, \tag{5.71}$$

$$\left.\frac{\partial y}{\partial z}\right|_{z=z_d} = \frac{y(t, z_{d+1}) - y(t, z_{d-1})}{2h} \qquad for\ 2 < d < 50, \tag{5.72}$$

$$\left.\frac{\partial y}{\partial z}\right|_{z=0} = \frac{-3y(t, z_1) + 4y(t, z_2) - y(t, z_3)}{2h} \qquad for\ d = 1, \tag{5.73}$$

$$\left.\frac{\partial y}{\partial z}\right|_{z=3\delta} = \frac{3y(t, z_{51}) - 4y(t, z_{50}) + y(t, z_{49})}{2h} \qquad for\ d = 51, \tag{5.74}$$

where y is any spatial-dependent variable, d is the node point position (d=1 defines the point at the electrode surface) and h is the distance between two consecutive node points, *i.e.*, h=$z_d - z_{d-1}$. This discretization procedure leaves a system of ordinary differential equations with respect to t that is solved using the *MATLAB ode15s* routine. The *ode15s* routine uses a method of backward differentiation suitable for a system of stiff algebraic–differential equations [92].

The values of the parameters were determined in two steps. The first step involved the determination of the parameters β_1, β_2, k_1, k_2 and k_{-2} by fitting to the additive–free impedance and steady current–voltage data presented previously in Chapter 3. As noted previously, the values of these parameters determined in Chapter 3 were not used since the form of the model was changed. The *MATLAB lsqnonlin* routine was used in the same manner as in Chapter 3. The additive model presented in the previous section was simplified by setting $C_P = 0$ and $C_{Cl} = 0$ to fit to the additive–free data. It is assumed that the numerical values of β_1, β_2, k_1, k_2 and k_{-2} remain unchanged when PEG and Cl^- are added to the system. Thus, once these values were determined, they were held fixed during step 2 of the fitting procedure that was followed to estimate the remaining parameters from the full version of the model and the experimental data obtained in the presence of PEG and Cl^-. Initially, attempts were made to estimate the values of the parameters β_3, β_4, k_3, k_4, k_5, k_6, k_7, k_8 and C_{dl} using the least–square regression method. However, after going through a number of iterations, the values of the parameters and residual sum of squares did not change. The reason that this was not successful could be due to the steep slopes of some of the experimental current–potential curves or that, as discussed later, each parameter affects only some of the voltammetry scans or a section of them and consequently some of the impedance spectra. Therefore, the approach followed was to estimate the values of β_3, β_4, k_3, k_4, k_5, k_6, k_7, k_8 and C_{dl} by a qualitative comparison between the predicted and measured voltammetry data. The experimental impedance data were not used for fitting purposes.

The algorithm used to fit the model to the experimental current-potential curves is outlined as follows:

1. Parameters β_3, β_4, k_3, k_4, k_5, k_6, k_7, k_8 and C_{dl} are set to their initial guesses.

2. Eqs. (5.9) and (5.12) are discretized using Eqs. (5.71)–(5.74) and solved together with Eqs. (5.10), (5.11), (5.13)–(5.16) and (5.23)–(5.38) using the *ode15s* routine to obtain the concentrations.

3. The current densities are obtained at each potential using the calculated concentrations and Eqs. (5.13)–(5.15) and (5.23)–(5.38). At each potential during the scan, the computed value of Γ_p is checked to determine whether $\Gamma_p \geq \Gamma_0$ or $\Gamma_p < \Gamma_0$. Eqs. (5.23)–(5.28) are used if $\Gamma_p < \Gamma_0$, while Eqs. (5.29)–(5.34) are used if $\Gamma_p \geq \Gamma_0$.

4. Steps 2 and 3 are repeated for each experimental condition.

5. The experimental data and model values are plotted.

6. The parameters in step 1 are modified one by one and steps 2 to 5 are repeated until a small deviation between the predicted current-potential curves and the measured ones is observed.

As noted previously, only the data from the cathodic scans were used for fitting purposes and estimating the kinetic parameters. Once they were determined, they were used to predict the impedance spectra and compare with the experimental data as follows:

1. Parameters β_3, β_4, k_3, k_4, k_5, k_6, k_7, k_8 and C_{dl} are set to the values obtained from the voltammetry data.

2. The zeroth order equations (5.39)–(5.47) are solved to obtain the zeroth order concentrations.

3. For each frequency, the concentration phasors are obtained by solving the first order equations (5.48)–(5.69) and using the concentrations and solution potential calculated in the previous step using the *bvp4c* routine.

4. The impedance is calculated at each frequency point using the following equation

$$Z = \frac{1}{\frac{-F(\tilde{r}_1+\tilde{r}_2+\tilde{r}_4+\tilde{r}_5)}{\tilde{E}'} + C_{\mathrm{dl}}\, j\, \omega} + R_{\mathrm{s}}. \tag{5.75}$$

5. Steps 2 to 4 are repeated for each experimental condition.

6. Finally, the experimental data and model values are plotted.

The conditions for EIS measurements were chosen so that the transition from a state where the electrode is completely covered by PEG to a partially covered state would not occur during the course of a single experiment.

5.4 Results

5.4.1 Parameter Estimation

The measured current-potential curves obtained for the series of experiments in Table 5.1 are shown in Fig. 5.1. The experimental conditions were chosen to span a wide range of electrode responses. In agreement with the findings in Chapter 4, Cu^{2+} reduction is more inhibited as the concentration of HCl is increased while the PEG concentration is held constant. Also, when the solution contains 1 mM HCl+50 μM PEG (curve 4), a gradual loss of inhibition with potential is observed. On the other hand, when the solution contains 0.001 mM HCl+10 μM PEG (curve 1) the current–potential curve is only inhibited at very small overpotentials and only slightly different from the one obtained in the absence of additives. Curves 2 and 3 show two intermediate cases of inhibition where the current densities are small until a critical potential of about -0.71 or -0.61 V is reached, whereupon the current density rapidly increases up to the level obtained in the absence of additives.

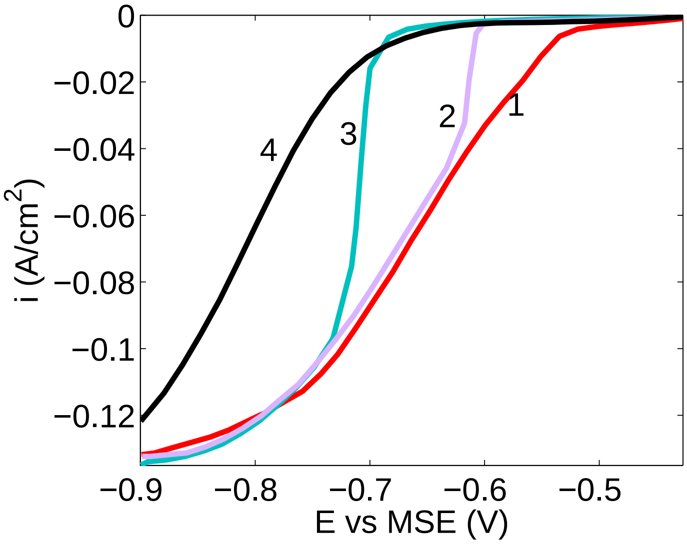

Figure 5.1: Experimental current–potential plots obtained in solutions containing 0.25 M $CuSO_4$+1.8 M H_2SO_4 and (1) 0.001 mM HCl+10 μM PEG, (2) 0.01 mM HCl+50 μM PEG, (3) 0.1 mM HCl+10 μM PEG, (4) 1 mM HCl+50 μM PEG.

Some of the parameters held constant throughout the fitting procedure are given in Table 3.2. The remaining constant parameters are given in Table 5.2. The values of D_{Cl}, D_P, Γ_s and Γ_0 were obtained from the literature, while the value of Γ_{Clc} was estimated using the ionic radius of the chloride ion [94]. The values of R_s estimated by extrapolating the high frequency loop of the Nyquist plot to the axis of the real impedance component

Table 5.2: Constant parameters used in the simulations.

Parameter	Value	Reference
D_{Cl}	2.032×10^{-5} cm^2 s^{-1}	[93]
D_P	9.916×10^{-7} cm^2 s^{-1}	[133]
Γ_{Clc}	1.61×10^{-9} mol cm^{-2}	this study
Γ_s	2.1×10^{-11} mol cm^{-2}	[124]
Γ_0	7.2×10^{-12} mol cm^{-2}	[124]
R_s	0.3 ohm cm^2	this study

were close to 0.3 ohm cm^2 for all the experimental conditions.

The parameter estimates for the additive–free model with the migration and homogeneous reaction terms neglected are given in Table 5.3. Similar to the procedure followed in Chapter 3, these parameters were obtained by fitting the model to the EIS data after obtaining initial guesses from fitting to the current–voltage data. The model fitted to obtain this data is similar to the model $M3$ presented in Section 3.4.4. Although not included here, the quality of the fit of the model to the experimental data is comparable to that obtained previously in Chapter 3. As previously discussed, if homogeneous reactions are neglected and the model is re–fitted to the experimental data, the value of k_1 in particular is affected since this rate constant is linked directly to the Cu^{2+} concentration through the forward direction of the first step. Dissolved copper is split between Cu^{2+} and $CuSO_{(aq)}$ when the homogeneous reactions are considered, whereas it is solely in the form of Cu^{2+} when homogeneous reactions are neglected. Comparison of Tables 3.5 and 5.3 shows that, as expected, k_1 is reduced by one order of magnitude while the other parameters change much less or not at all.

Table 5.3: Parameters obtained by least squares fitting of the model to additive–free data.

Parameter	Value [a]
β_1	0.479
β_2	0.422
k_1	1.307×10^{-8} cm s^{-1}
k_2	2.276×10^{-9} mol $cm^{-2}s^{-1}$
k_{-2}	6.091×10^{-2} mol $cm^{-2}s^{-1}$

[a] based on MSE scale

The values of the remaining parameters estimated in this analysis are given in Table 5.4. The value of the double layer capacitance C_{dl} is similar to the value obtained in the absence of additives (see Table 3.5). The current–potential curves shown in Fig. 5.2 were predicted using the parameters in Tables 5.3 and 5.4. These results exhibit the same trend observed in Fig. 5.1, *i.e.*, the inhibition of Cu^{2+} reduction increases as the additive concentrations are changed from experiment 1 to 4. Also, in agreement with the experimental results,

Table 5.4: Parameters obtained by fitting of the model.

Parameter	Value [a]
β_3	0.479
β_4	0.422
k_3	1.0×10^{-4} cm^4 (s mol)$^{-1}$
k_4	1.0×10^{-10} mol cm^{-2}s^{-1}
k_5	4.8 cm s^{-1} cm s^{-1}
k_6	6.0×10^{6}
k_7	7.0×10^{-2}
k_8	2.6×10^{11} cm^3 (s mol)$^{-1}$
C_{dl}	7.7×10^{-5} F cm^{-2}

[a] based on MSE scale

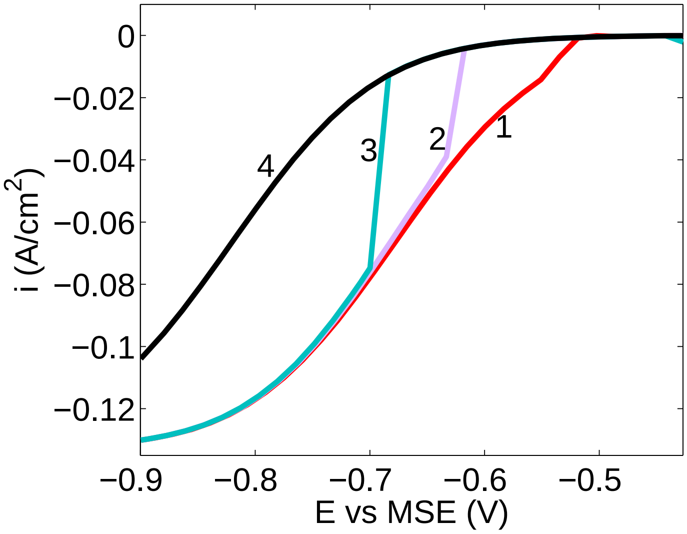

Figure 5.2: Current–potential plots obtained from fitting the model to the data measured in solutions with composition 0.25 M $CuSO_4$+1.8 M H_2SO_4 and (1) 0.001 mM HCl+10 μM PEG, (2) 0.01 mM HCl+50 μM PEG, (3) 0.1 mM HCl+10 μM PEG, (4) 1 mM HCl+50 μM PEG.

the calculated current density gradually rises with increasing overpotential in experiment 4 and abruptly increases at the critical potential in experiments 2 and 3. After the inhibition is lost, the electrode responses of experiments 1, 2 and 3 become identical to that of the uninhibited response.

A comparison of the fitted and measured data is shown in Fig. 5.3. Good agreement between the predicted and measured data is observed for all experiments. The abrupt loss of inhibition is predicted to occur at a critical potential slightly more negative than the observed value for experiment 2 and slightly more positive for experiment 3. On the other hand, the current densities in experiment 4 are to some extent underestimated at large overpotentials. A decrease in the value of the factor k_7 from that given in Table 5.4 improves the fitting at large overpotentials, but tends to overestimate the current densities at lower overpotentials.

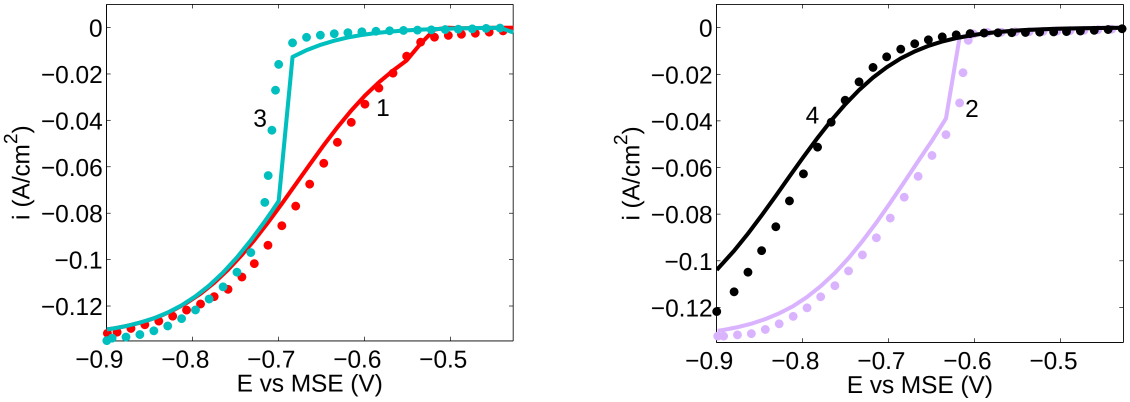

Figure 5.3: Comparison of the model fit (solid line) to measured current–potential plots (dotted lines) obtained for Experiments 1 and 3 (left) and Experiments 2 and 4 (right).

The values of θ_{Cu} and θ_{Clc} corresponding to the curves in Fig. 5.3 are plotted as a function of potential in Fig. 5.4. At the OCP, θ_{Cu} has a value of about 0.7 for all conditions. Thereafter, θ_{Cu} decreases rapidly with potential since copper starts to deposit and becomes negligible at a potential of -0.6 V. θ_{Clc} remains very small at all potentials and solution compositions.

The corresponding values of Γ_p are plotted as a function of the applied potential for all experimental conditions in Fig. 5.5. It is worth noting that the electrode was held at the

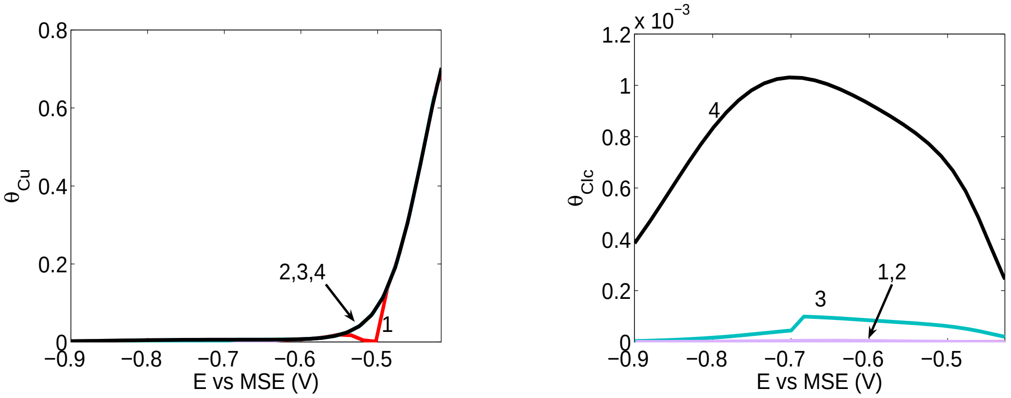

Figure 5.4: Evolution of θ_{Cu} (left) and θ_{Clc} (right) with potential in Experiments 1 to 4.

OCP for about 10 seconds prior to the start of each scan experiment. By the end of this period, the OCP was almost constant. To account for this in the model, the value of Γ_p at the outset of each scan was set to the steady state value calculated at OCP, except for the case of experiment 1 where the value was set to a value somewhat higher than the computed steady state value. This was found to be necessary to obtain the very small inhibition observed close to the OCP. The slopes of the curves in Fig. 5.5 not surprisingly bear a resemblance to the corresponding current–potential curves. These results show that at the

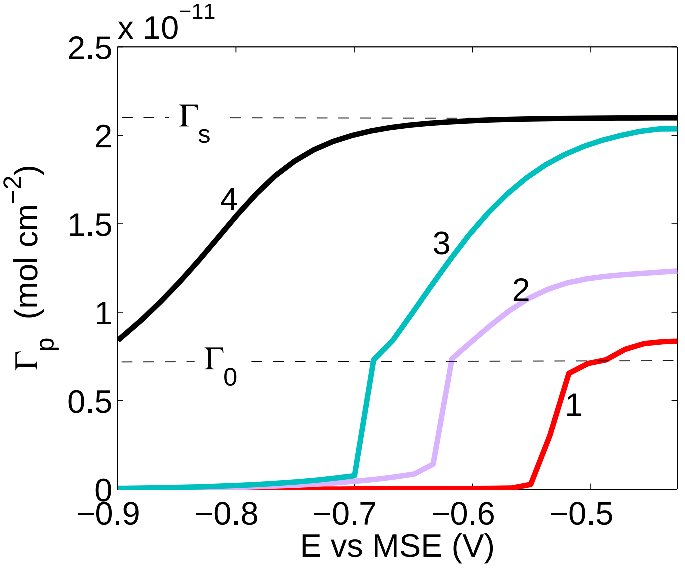

Figure 5.5: Evolution of Γ_p with potential in Experiments 1 to 4. Dashed horizontal lines indicate the levels of Γ_0 and Γ_s.

outset of the scan the coverage of the inhibiting film is saturated when the concentrations of both HCl and PEG are high (curve 4). Furthermore, Γ_p remains greater than Γ_0 throughout the scan, signifying that the electrode always remains completely covered. The coverage decreases slowly early in the scan, but then more rapidly below about -0.7 V. On the other hand, Γ_p initially lies between Γ_0 and Γ_s in curves 1, 2 and 3, which indicates that the surface is completely covered, but not saturated, by the inhibiting film. Curves 1, 2 and 3 are similar in that the PEG coverage is reduced in three stages: *i)* relatively gradual decrease from the initial value to Γ_0, *ii)* sharp decrease from Γ_0 to low values and *iii)* very slow and linear decrease to negligible coverage at large overpotentials. The potential where the coverage reaches Γ_0 and is abruptly reduced corresponds to the critical potential from the voltammetry scans.

The reaction rates r_1, r_2, r_3 and r_4 are plotted as a function of potential in Fig. 5.6. The results show that r_1 and r_2 are virtually identical to each other at all potentials and solution compositions. This is not surprising reflecting that the rate of formation of Cu^0 by pathway 1, *i.e.*, reactions (5.17) and (5.18), is limited by the first step, as is the case under additive–free conditions. r_1 and r_2 increase smoothly during the scan when the additive concentrations are either low (Fig. 5.6a) or high (Fig. 5.6d). On the other hand, at intermediate additive concentrations (Figs. 5.6b and c), r_1 and r_2 increase very little in the first part of the scan, then rise sharply at the critical potential before finally rising more slowly again at the end of the scan. Similar trends are observed for r_3 and r_4 in Figs. 5.6e, f, g and h.

The adsorption rate r_5 and desorption rate r_6 of PEG in reactions (5.21) and (5.22) are plotted in Fig. 5.7. At low and intermediate additive concentrations (Figs. 5.7a–c), the desorption rate exceeds the adsorption rate only slightly in the early part of the scan up to the critical potential. The difference becomes large over a narrow potential range which leads to the observation of abrupt activation at a critical potential. Thereafter, the two rates become essentially equal to each other as they decrease toward zero. Fig. 5.7a shows that at low additive concentrations, the adsorption rate of PEG during the scan is always very small and so the initial amount adsorbed is removed by a potential of -0.55 V. As shown in Figs. 5.7b and c, at intermediate concentrations, the adsorption rate can keep up with the desorption rate as the scan ensues until the critical potential is reached.

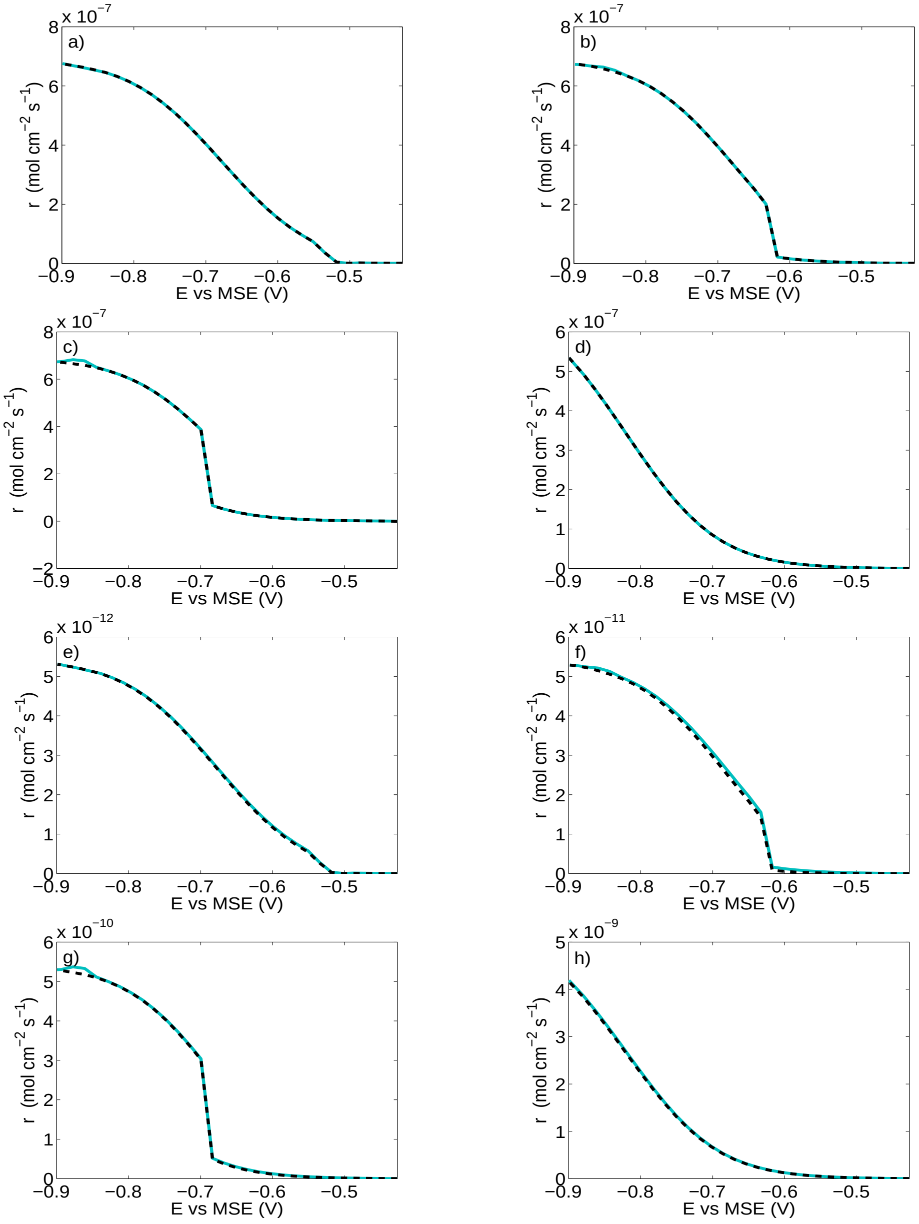

Figure 5.6: Reaction rates (a), (b), (c), (d) r_1 (solid lines) and r_2 (dashed lines) and (e), (f), (g), (h) r_3 (solid lines) and r_4 (dashed lines) versus potential obtained for 0.25 M $CuSO_4$+1.8 M H_2SO_4 solutions containing (a) and (e) 0.001 mM HCl+10 μM PEG, (b) and (f) 0.01 mM HCl+50 μM PEG, (c) and (g) 0.1 mM HCl+10 μM PEG and (d) and (h) 1 mM HCl+50 μM PEG.

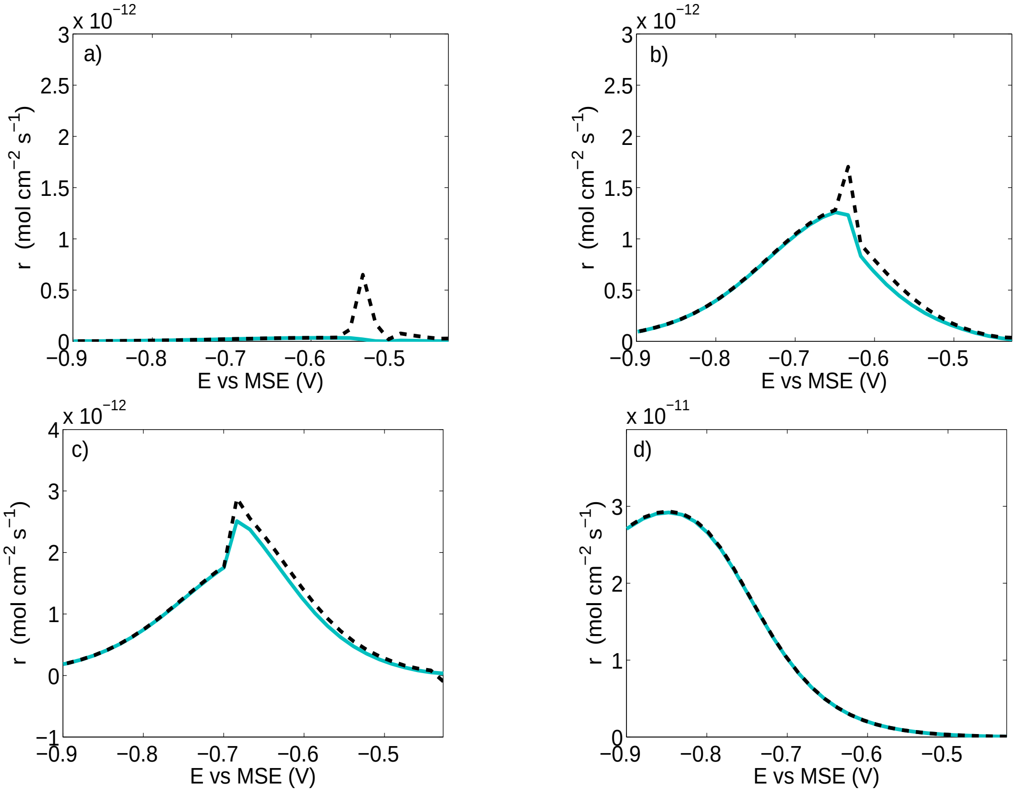

Figure 5.7: Rates of adsorption (solid lines) and desorption (dashed lines) of ClCuPEG plotted versus potential obtained for 0.25 M $CuSO_4$+1.8 M H_2SO_4 solutions containing (a) 0.001 mM HCl+10 μM PEG, (b) 0.01 mM HCl+50 μM PEG, (c) 0.1 mM HCl+10 μM PEG and (d) 1 mM HCl+50 μM PEG.

Fig. 5.7d shows that at high additive concentrations the adsorption and desorption rates are very similar throughout the scan. The desorption rate is only slightly greater than the adsorption rate so that the decrease in Γ_p is more gradual.

The impedance spectra predicted by the model are compared to the experimental data in Fig. 5.8. Given the sensitivity of the EIS technique, good agreement is observed between the calculated and experimental data in Figs. 5.8a, b and c. The first semicircle in Fig. 5.8d is well predicted but the second one which is commonly associated with mass transfer effects is underestimated. An attempt was made to improve the fitting of the second semicircle by reducing the value of the parameter k_7. However, the size of the second semicircle increased as a result and so did the first semicircle. The fitting showed in 5.8d was the best result

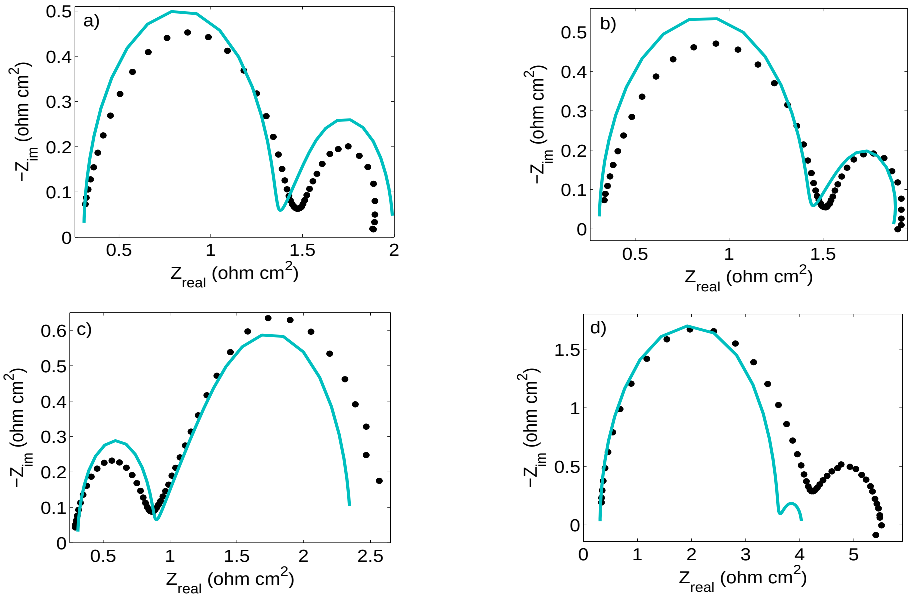

Figure 5.8: Comparison of the model data (solid lines) and measured EIS Nyquist plots (dotted lines) obtained for (a) Experiment 1, (b) Experiment 2, (c) Experiment 3, and (d) Experiment 4 at (a) and (b) -0.65 V, (c) -0.75 V, (d) -0.7 V.

obtained.

The model was also used to predict the impedance spectra for two other conditions at which experiments were done. These experiments were carried out at -0.6 and -0.65 V in solutions with the same compositions as in experiments 2 and 3, respectively. These potentials are more positive than the corresponding critical values and consequently the measured steady state current densities are extremely small. The magnitudes of the measured real and imaginary components of the impedance so obtained reach values one order of magnitude higher than those obtained in the experiments shown in Figs. 5.8b and c. The impedance spectra predicted by the model using the parameters in Table 5.4 compared to the measured spectra are shown in Fig. 5.9. Obviously, the agreement is poor. The steady state current densities predicted by the model for the spectra in Fig. 5.9 are -3.0x10^{-3} and -7.3x10^{-3} A/cm^2, compared to the measured values of -1.0x10^{-3} and -2.0x10^{-3}. Such deviations are very small and certainly acceptable for the range of currents measured during the voltammetry experiments. However, such differences lead to large deviations between the simulated and measured spectra due to the extreme sensitivity of the impedance to changes

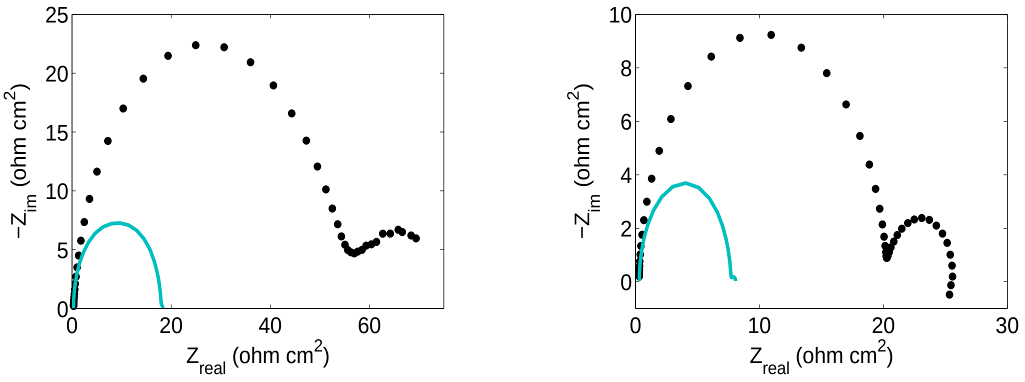

Figure 5.9: Comparison of the model data (solid lines) and measured EIS Nyquist plots (dotted lines) obtained in 0.25 M $CuSO_4$+1.8 M H_2SO_4+0.01 mM HCl+50 μM PEG (left) and 0.25 M $CuSO_4$+1.8 M H_2SO_4+0.1 mM HCl+10 μM PEG (right) solutions at -0.6 V and -0.65 V, respectively.

in the steady state current density particularly when the current density is very low. As shown in Fig. 5.10, a better agreement was observed if k_7 was set to 2.4×10^{-2} rather than to 7×10^{-2} obtained previously and calculated current densities of -1.1x10^{-3} and -2.7x10^{-3} were obtained. However, this worsened the fitting of the model to the spectra in Fig. 5.8d and the current–potential curves in Fig. 5.3. Therefore, the set of values given in Table

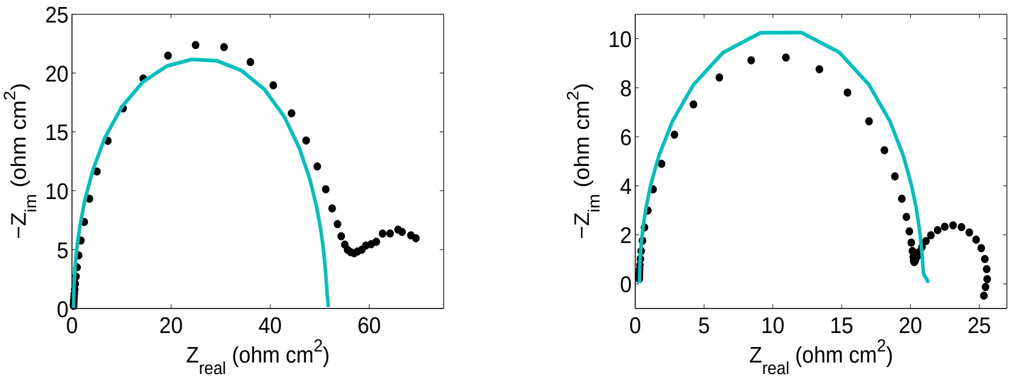

Figure 5.10: Comparison of the model data (solid lines) using k_7=2.4×10^{-2} and measured EIS Nyquist plots (dotted lines) obtained in 0.25 M $CuSO_4$+1.8 M H_2SO_4+0.01 mM HCl+50 μM PEG (left) and 0.25 M $CuSO_4$+1.8 M H_2SO_4+0.1 mM HCl+10 μM PEG (right) solutions at -0.6 V and -0.65 V, respectively.

5.4 was taken as the best estimate.

5.4.2 Sensitivity Analysis

An analysis was carried out to study the sensitivity of the model to the estimates of the parameters. The minimum factor by which each parameter in Table 5.4 had to be multiplied to observe any difference in the predicted current–potential curves was investigated. The parameters β_3, β_4, k_3, k_4, k_5, k_6, k_7, k_8 and C_{dl} were multiplied by factors 1.005, 1.001, 1.08, 1.05, 1.9, 1.02, 1.01, 1.1 and 1.7, respectively, to obtain the results shown in Fig. 5.11. Shown in this figure are also the curves obtained with the parameters in Table 5.4. The main effect observed as a result of the perturbations is the shift of the critical potential to either more positive or negative values, except for the perturbation of k_5 that has only a very small effect at potentials more negative than the critical potential (Fig. 5.11e). As expected, these results show that the values of charge transfer coefficients β_3 and β_4 which are arguments in exponential functions have the largest effect on the electrode response. The model is also sensitive to the parameters k_3, k_4, k_6 and k_7. The model is not strongly sensitive to the parameters k_5, k_8 and C_{dl} since they have to be increased by 90%, 10% and 70% to observe any noticeable difference in the results.

The results in Chapter 3 revealed that the impedance data is more sensitive to changes in the parameter values than the current–potential data. Thus, it would be expected that the perturbations of β_3, β_4, k_3, k_4, k_5, k_6, k_7, k_8 and C_{dl} mentioned above would have a major effect on the impedance spectra. However, the perturbations of β_3, β_4, k_3, k_4, k_6, k_7, k_8 and C_{dl} did not have a significant effect on the results and the impedance spectra (not shown here) were very similar to those shown in Fig. 5.8. This can be explained from the results in Fig. 5.11 that show the perturbations on these parameters to affect the electrode response only very close to the critical potential, but not at potentials somewhat removed from the critical potential. The impedance spectra in Fig. 5.8 were obtained at potentials far enough from the critical potential for these parameters not to influence them significantly. The impedance spectra obtained by perturbing k_5 by a factor of 1.9 are shown in Fig. 5.12. In agreement with the results in Fig. 5.11, only the spectra obtained at intermediate additive concentrations and potentials more negative than the critical potential are affected, as shown in Figs. 5.12b and c.

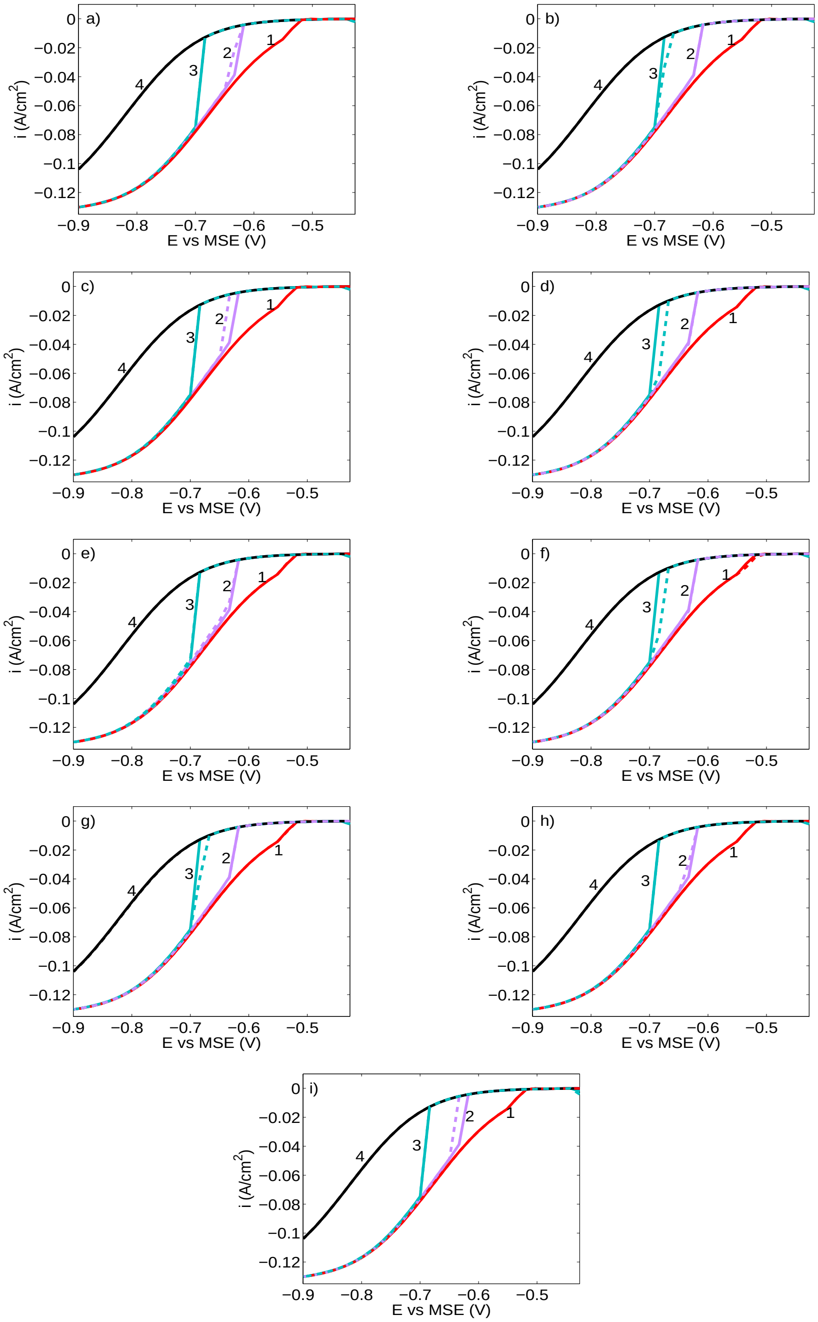

Figure 5.11: Sensitivity analysis of parameters to the current–potential plots. Original parameters (solid lines), effect of (a) β_3, (b) β_4, (c) k_3, (d) k_4, (e) k_5, (f) k_6, (g) k_7, (h) k_8 and (i) C_{dl} perturbations (dashed lines). Factors by which each original parameter is multiplied is given in the text.

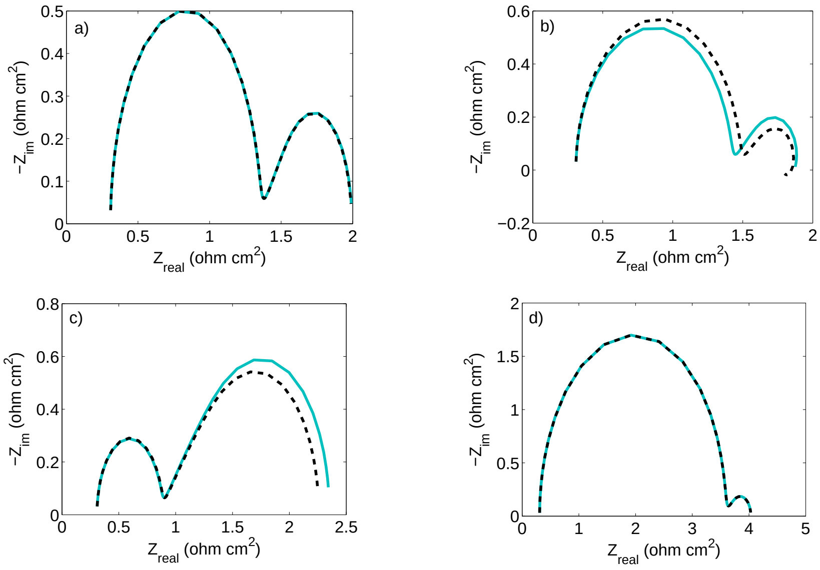

Figure 5.12: Sensitivity analysis of parameters to the Nyquist plots. Original parameters (solid lines), effect of k_5 multiplied by a factor of 1.9 (dashed lines) in (a) Experiment 1, (b) Experiment 2, (c) Experiment 3 and (d) Experiment 4.

5.4.3 Steady State Behavior

As noted previously, an important aspect of the proposed mechanism is the form of the rate expression of PEG desorption. This becomes very apparent when the steady state behavior of the model is examined. Although not shown here, when the rate equations (Eqs. (5.23)–(5.34)) are set to steady state conditions and the resulting algebraic equations are solved, one obtains a quadratic equation in $\overline{\Gamma}_p$ (steady state adsorption density) for the condition $\Gamma_p < \Gamma_0$ and another quadratic equation for the case $\Gamma_p \geq \Gamma_0$. In each case, one of the roots is physically possible while the other is not feasible. Table 5.5 shows how the physically possible solutions of $\overline{\Gamma}_p$ vary with potential for the solution compositions of Experiments 1–4. For low (Experiment 1) and high (Experiment 4) PEG and Cl^- concentrations where the current rises smoothly during the scan, the model predicts only one feasible solution for $\overline{\Gamma}_p$. On the other hand, at intermediate additive concentrations (Experiments 2 and 3) where activation occurs abruptly at a critical potential, the model predicts a range of potentials where two physically possible solutions exist. Further examination of Table 5.5 reveals that the critical potentials observed during Experiments 2 and 3 lie very close to the

Table 5.5: Steady state Γ_p values as a function of applied potential.

Experiment 1		Experiment 2			Experiment 3			Experiment 4	
E (V)	$\overline{\Gamma}_p$x10^{15} (mol cm^{-2})	E (V)	$\overline{\Gamma}_p$x10^{12} (mol cm^{-2})		E (V)	$\overline{\Gamma}_p$x10^{12} (mol cm^{-2})		E (V)	$\overline{\Gamma}_p$x10^{12} (mol cm^{-2})
-0.41	493	**-0.41**	12.5		**-0.43**	20.4		**-0.43**	21.0
-0.45	281	**-0.46**	11.8		**-0.47**	19.8		**-0.46**	21.0
-0.47	228	**-0.47**	11.5	6.59	**-0.49**	19.5		**-0.48**	21.0
-0.49	183	**-0.49**	11.2	5.72	**-0.51**	19.1		**-0.49**	21.0
-0.50	148	**-0.50**	10.8	4.93	**-0.52**	18.5		**-0.51**	21.0
-0.52	118	**-0.52**	10.4	4.15	**-0.54**	17.9		**-0.52**	21.0
-0.53	93.6	**-0.54**	9.84	3.45	**-0.55**	17.1	6.72	**-0.54**	20.9
-0.55	74.2	**-0.55**	9.28	2.85	**-0.57**	16.1	4.67	**-0.56**	20.9
-0.57	59.0	**-0.57**	8.67	2.33	**-0.59**	15.0	3.56	**-0.57**	20.9
-0.58	46.7	**-0.59**	8.01	1.90	**-0.60**	13.7	2.75	**-0.59**	20.9
-0.60	37.1	**-0.60**	7.33	1.55	**-0.62**	12.3	2.16	**-0.61**	20.8
-0.62	29.7	**-0.61**		1.43	**-0.64**	10.9	1.73	**-0.62**	20.8
-0.63	23.7	**-0.61**		1.32	**-0.65**	9.39	1.40	**-0.64**	20.7
-0.65	19.1	**-0.62**		1.26	**-0.67**	7.99	1.13	**-0.65**	20.6
-0.66	15.3	**-0.63**		1.03	**-0.68**		0.923	**-0.67**	20.4
-0.70	9.81	**-0.67**		0.679	**-0.70**		0.721	**-0.70**	20.0
-0.74	5.15	**-0.71**		0.362	**-0.72**		0.617	**-0.75**	18.5
-0.79	2.55	**-0.76**		0.188	**-0.76**		0.332	**-0.80**	15.4
-0.84	1.21	**-0.81**		0.0923	**-0.81**		0.170	**-0.85**	11.7
-0.90	0.466	**-0.88**		0.0338	**-0.88**		0.0642		
		-0.90		0.0234	**-0.90**		0.0453		

negative ends of the potential ranges where two feasible solutions exist. Thus, it appears that the system tends to follow the high $\overline{\Gamma}_p$ condition (*i.e.*, more inhibited) during the forward scan as long as possible before being activated. A nonlinear dynamical analysis is required to determine whether the model can predict this behavior.

Fig. 5.13 shows a plot of the steady state current versus potential for Experiments 1–4 based on the $\overline{\Gamma}_p$ values listed in Table 5.5. In the cases of Experiments 2 and 3, the responses were plotted by assuming the system follows the more inhibited state over the potential range where two solutions exist. The responses agree well with those shown in Fig. 5.3 for the measured and computed voltammograms obtained at a scan rate of 2 mV/s.

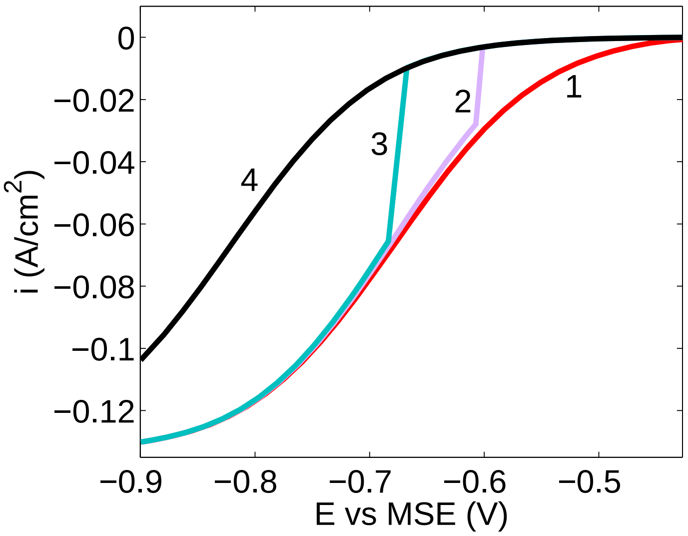

Figure 5.13: Predicted current–potential plots for steady state conditions in 0.25 M $CuSO_4$+1.8 M H_2SO_4 solutions containing (1) 0.001 mM HCl+10 μM PEG, (2) 0.01 mM HCl+50 μM PEG, (3) 0.1 mM HCl+10 μM PEG and (4) 1 mM HCl+50 μM PEG.

Based on the model, such a scan rate is slow enough to allow the electrode response to relax enough to approach steady state conditions.

5.4.4 Prediction of Cyclic Voltammograms

Only the forward scans of current–potential curves were used to estimate the parameters of the model. However, Table 5.5 shows that two states are predicted in certain potential regions that correlate well with the regions where hysteresis is observed in cyclic voltammograms. Fig. 5.14 shows the forward and backward scans predicted using the parameters in Table 5.4 and compared to the experimental data. It should be noted that the computed electrode responses are based on the transient model. Good agreement between the predicted and measured data is observed. Furthermore, the model predicts significant hysteresis in experiments 2 and 3 and slight hysteresis in experiment 1, in agreement with the experimental results.

Fig. 5.15 shows the corresponding surface concentrations for Cu^{2+}, Cl^- and PEG calculated from the model for the forward and backward current–potential scans of Experiments

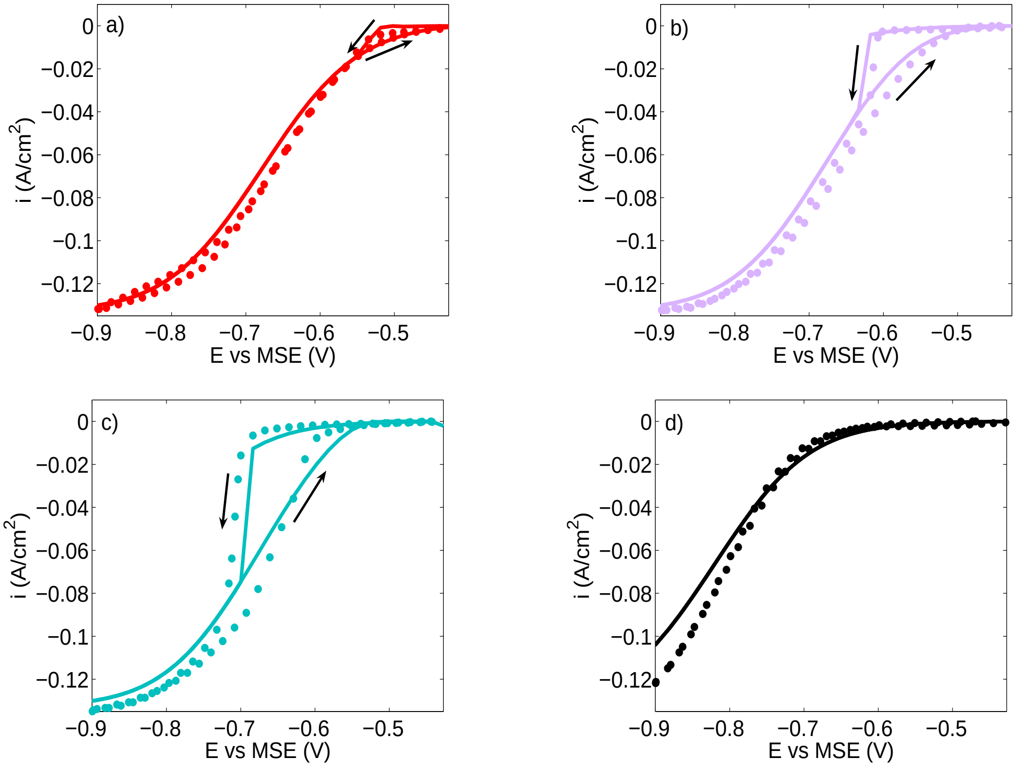

Figure 5.14: Comparison of the model data (solid lines) and cyclic current–potential curves (dotted lines) obtained in 0.25 M $CuSO_4$+1.8 M H_2SO_4 solutions containing (a) 0.001 mM HCl+10 μM PEG, (b) 0.01 mM HCl+50 μM PEG, (c) 0.1 mM HCl+10 μM PEG and (d) 1 mM HCl+50 μM PEG.

1–4. The curves of the computed potential dependence of surface concentration of Cu^{2+} (Fig. 5.15a) are very similar in shape to the corresponding electrode responses in Fig. 5.14. At high PEG and Cl^- concentrations (Experiment 4), the rise in current due to Cu^{2+} reduction is gradual enough that the surface concentration shows no hysteresis. On the other hand, the abrupt rise in the rate of Cu^{2+} reduction at the critical potential in the case of intermediate additive concentrations causes a rapid drop in the surface concentration that cannot be recovered by mass transport. Thus, the surface concentration during the reverse scan is lower than that during the forward scan. The surface concentration of Cl^- is not significantly depleted during the forward and backward scans, as shown in Fig. 5.15b. Fig. 5.15c shows that PEG is not depleted at the electrode surface except in the strongly inhibited case (Experiment 4). However, this depletion is related to the as-

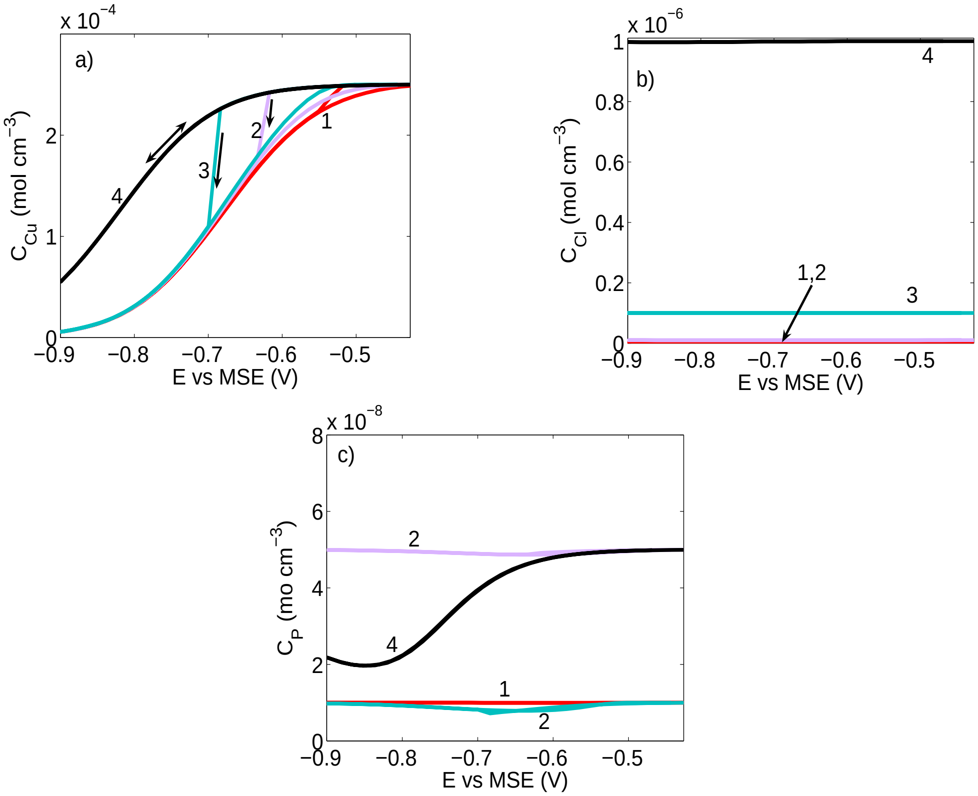

Figure 5.15: Predicted surface concentrations of (a) Cu^{2+}, (b) Cl^{-} and (c) PEG versus potential.

sumption that the products of the desorption reaction (5.22) have no effect on the process and are not specified. Taken together the results in Fig. 5.15 indicate that the hysteresis at intermediate concentrations is due to depletion of Cu^{2+} at the electrode surface. The surface concentration of Cu^{2+} during the reverse scan decreases to the point that the rate of adsorption of the ClCuPEG complex is slowed down, but Cu^{2+} reduction is not. This results in a higher current than during the forward scan where the rate of formation of the inhibiting film is large enough to more strongly suppress copper deposition even in the presence of a higher surface concentration of Cu^{2+}.

5.4.5 Effect of Scan Rate

The model was also used to determine if the effect of the scan rate on the electrode responses shown in Fig. 4.5 could be predicted. The responses were calculated for additive concentrations of 0.1 mM Cl^-+10 μM PEG due to the inability of the model to predict the response at the experimental conditions of 0.1 mM Cl^-+88 μM PEG as explained later. The results in Fig. 5.16 reveal the similar trend of a negative shift in the steep rise portion of the electrode response as in the measurements although the computed effect is more pronounced than that observed experimentally. The critical potential remains almost the same at 2 and 5 mV/s, but shifts to slightly more negative values at 10 and 20 mV/s and significantly more negative values at 50 and 100 mV/s.

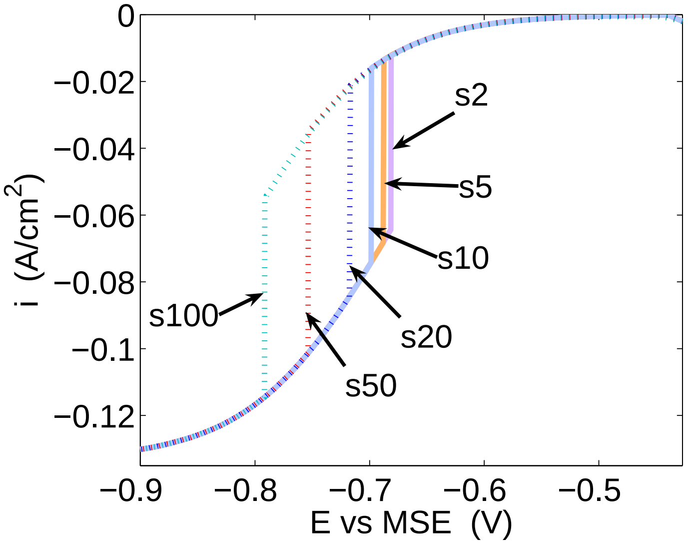

Figure 5.16: Predicted current–potential curves obtained in a solution containing 0.1 mM Cl^-+10 μM PEG at a sweep rate of (S2) 2mV/s, (S5) 5mV/s, (S10) 10mV/s, (S20) 20mV/s, (S50) 50mV/s and (S100) 100mV/s.

5.4.6 Simulation of Series II Experiments

As a further test of the model, an effort was made to determine whether the results of experiment K in the series II experiments of Chapter 4 (Fig. 4.9) could be predicted. In this experiment, the solution contained 0.1 mM Cl^-+88 μM PEG until -0.8 V during the forward scan, whereupon the Cl^- concentration was raised to 1 mM. Fig. 5.17 shows a comparison of the experimental and predicted curves. The computed curve was determined by taking the solution at the outset of the scan to contain 0.1 mM Cl^-+10 μM PEG instead

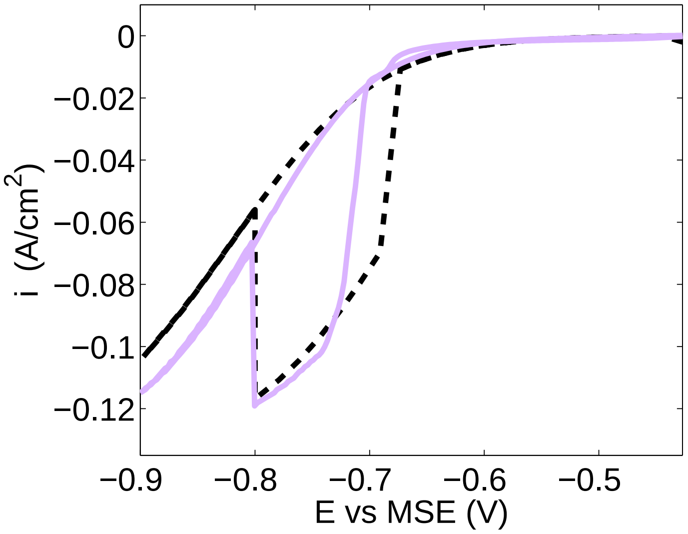

Figure 5.17: Predicted current–potential curve (dashed line) compared to the response obtained in the series II experiment (solid line) with initial and final solutions containing 0.1 mM Cl$^-$+88 μM PEG and 1 mM Cl$^-$+88 μM PEG, respectively.

of 0.1 mM Cl$^-$+88 μM PEG due to the inability of the model to predict the response for the latter case. In agreement with the experimental results, the model predicted restoration of the inhibiting film to occur after the increase of the Cl$^-$ concentration.

5.4.7 Shortcomings of the Model

As any other model, this one is not perfect and not able to predict all of the experimental findings. For example, experimental results in section 4.3.1 and other previous studies show that the electrode response is no longer affected by further additions of Cl$^-$ and PEG when their concentrations have reached a limit. The model developed in this study was not able to predict this limiting condition when 0.1 mM HCl and concentrations higher than 50 μM PEG are present in solution. Strong inhibition was predicted over a wider potential range than in the experimental results and the critical potential was shifted if the concentration of PEG was increased beyond 10 μM in the presence of 0.1 mM HCl. This is not consistent with the findings in section 4.3.1. The disagreement between the model and experimental responses suggests that the model predicts a larger amount of PEG to be attached to the surface above the critical potential compared to the experimental situation. Thus, the adsorption rate which depends on the surface concentration of PEG should be modified to account for the limiting effect. For example, the adsorption of PEG should be constrained by the maximum number of Cl^- linkages available on the surface. The results in section 4.3.2 show that even in the presence of a significant amount of PEG available for adsorption, Cu^{2+} reduction will not be strongly inhibited if not enough Cl^- is present in solution.

Also, lower currents are predicted at higher overpotentials in Experiment 4 of this chapter (Figs. 5.3 and 5.14d). As discussed in Chapter 4, the thickness as well as the conformation of the inhibiting film likely changes as the forward scan ensues. It is possible that if the model accounted for the reduction in the inhibiting film thickness as a function of the amount left on the surface, it could better predict the current–potential curves obtained at high additive concentrations. In the context of the current model, this thickness of the film is accounted for by the retardation factor k_7. It should be recalled that the retardation factor k_7 was assumed to be constant in the current model.

The model was also tested to determine if it could predict acceleration in solutions containing only Cl^- and no PEG. However, the current–potential curves obtained with the parameters given in Table 5.4, but with C_P=0 set in the model do not exhibit acceleration (Fig. 5.18a). Regardless of the chloride concentration, the calculated curves are essentially identical to that obtained in an additive–free solution. This does not mean that the model

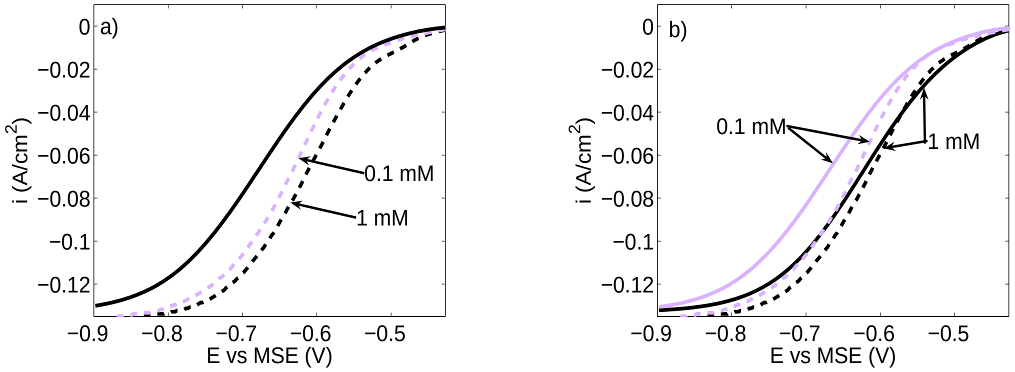

Figure 5.18: Predicted current–potential curves obtained in solutions containing 0.1 and 1 mM Cl^- and no PEG using (a) k_3=1x10^{-4} and (b) k_3=3x10^{-2}. Solid lines represent the predicted data and dashed lines the measured data.

cannot predict acceleration since acceleration is observed when the value of the parameter k_3 is increased to 3x10^{-2} as shown in Fig. 5.18b. Unfortunately, with this value of k_3, the match between the computed and experimental responses when both PEG and Cl^- are present suffers. It is possible that presence of PEG in solution affects the rate at which Cl^- is adsorbed on the surface. If so, the value of k_3 should be different depending on the presence of PEG.

The model was also used to predict chronoamperometry results such as those shown in Fig. 4.7 of the previous chapter. The solution composition used to calculate the transient curves is 0.1 mM Cl^-+10 μM PEG due to the inability of the model to predict the electrode response in a solution containing 0.1 mM Cl^-+88 μM PEG, as discussed at the beginning of this section. The predicted curve for the film formation in a single step measurement at -0.65 V (FF') is compared to the measured response (FF) in Fig. 5.19. These results show

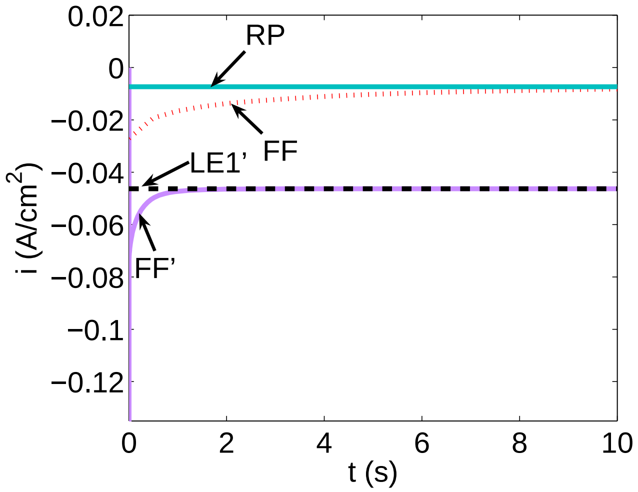

Figure 5.19: Predicted current–time curves obtained in a solution containing 0.1 mM Cl^-+10 μM PEG for the formation (FF') and restoration (LE1') of the inhibiting film. RP denotes the more inhibited steady state value predicted by the model at -0.65 V.

that the current predicted for the formation of the film reaches the value of -0.047 A/cm^2 which is higher than the measured value of -0.008 A/cm^2. Furthermore, a comparison with Fig. 5.14c shows that -0.047 A/cm^2 is the same as that predicted in the reverse scan. It should be noted that the model predicts two steady state current densities under these conditions: -0.047 A/cm^2 and -0.0073 A/cm^2. The measured response (FF) approaches the more inhibited steady state (RP) very well. The disagreement between the curves FF' and FF is an indication that the model is not predicting the shift from the less inhibited to the more inhibited state in this case. A possible explanation for this is that the initial current predicted by the model (FF') increases to high values due to the double layer charging so that the response eventually approaches the current of the less inhibited steady state. The model was also used to predict the restoration of the film (LE1') when the potential was held at -0.65 V during the reverse scan after the forward scan to -0.9 V. The current density in curve LE1' remains the same as the value of the plateau of curve FF' at all times. This may be explained by the fact that after the current reaches the uninhibited value during the forward scan at large overpotentials in LE1', it tends to remain uninhibited rather than shifting to the inhibited state.

The model was also used to predict the dynamics of the desorption of the inhibiting film in the series III experiment where the film is first formed in a solution containing 1 mM Cl^-+88 μM PEG and then desorbed in a solution containing only 1 mM Cl^- (Fig. 4.17). The dynamics of the desorption of the film was measured at -0.55 V after the potential was scanned from OCP to -0.55 V. Fig. 5.20 shows that the initial current is predicted to be higher than the measured value. This is likely due to the assumption that a complete layer

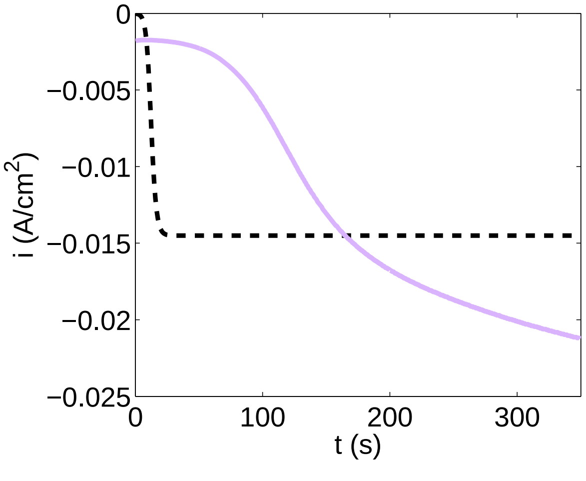

Figure 5.20: Comparison of the predicted (dashed line) and measured (solid line) current–time curves obtained in a series III experiment with solution 1 and 2 containing 1 mM Cl^-+88 μM PEG and 1 mM Cl^-, respectively. The potential is held at -0.55 V after scanning from OCP.

covers the surface at the outset of the scan, which may be not the case in the real situation. Most importantly, the calculated current increases due to the breakdown of the film more quickly than that observed experimentally. It is not clear whether the plateau observed at short times in the experimental curve is due to an unknown aspect of the desorption of the film or an effect that the desorbed species may have in helping to maintain inhibition for a longer period of time. In any event, the model does not account for any of these possibilities. In addition, the calculated and measured currents reach different values after long times during this experiment which is explained by the fact that the acceleration of Cu^{2+} reduction is not predicted with this model using the parameters in Table 5.4.

Chapter 6

Conclusions

6.1 Summary of Contributions

Due to the mathematical complexity of physicochemical models used to obtain impedance data, their solution is inevitably subject to assumptions. In Chapter 3, a physicochemical model was developed that accounts for phenomena neglected in previous EIS studies. It accounts for diffusion, convection and migration as well as chemical and electrochemical reactions. The model was used to predict steady state and impedance data of Cu^{2+} reduction onto an RDE in acidic solution absent of additives. The following points summarize the contributions of this chapter:

- Kinetic and physicochemical parameters were estimated using nonlinear regression compared to less rigorous methods used in most previous studies to estimate parameters of Cu^{2+} reduction.

- The fitting of the model to the impedance data was further improved by accounting for the residual correlation. This correlation was incorporated into the model using the first–order autoregressive process.

- The sensitivity of the model to each parameter was analyzed and not surprisingly was found to be stronger for those parameters associated with the rate controlling step of Cu^{2+} reduction. Particularly, the model was highly insensitive to the rate constant of the backward reaction of the controlling step. Thus, this backward step can be neglected if the model is used for Cu^{2+} reduction under cathodic conditions.

- With the estimated parameters, the importance of the phenomena included in the model was also analyzed. Migration was found to have little effect on either the steady state or impedance results. However, important deviations in the model predictions were observed when convection or chemical reactions were neglected.

Some aspects concerning the mechanism for the formation and disruption of the inhibiting film in solutions containing Cl^- and PEG were studied in Chapter 4. The electrode responses of Cu^{2+} reduction can be classified into three categories depending on the Cl^- and PEG concentrations: *i)* slight inhibition only in the vicinity of the OCP at low additive concentrations, *ii)* transition from strong inhibition to complete re-activation of electrode at a critical potential at intermediate additive levels and *iii)* strong inhibition at lower overpotentials followed by a gradual increase in current at high additive levels. The following points highlight the findings in Chapter 4:

- The dynamics of the formation of the inhibiting film at a certain potential depends on the concentrations of Cl^- and PEG. The formation is relatively slow in the presence of low additive concentrations. However, when the concentrations are increased and reach the point where the inhibiting film completely covers the surface, the electrode response is virtually instantaneous and the current drops significantly due to the onset of strong inhibition.

- The types of electrode responses and dynamics of the formation and disruption of the inhibiting film were explained based on a qualitative description of PEG adsorption and desorption recently presented in the literature regarding the change in conformation of the PEG molecule.

- More current in the reverse than in the forward cathodic scan was observed at intermediate PEG and Cl^- concentrations. Inhibition can be restored when the reversed scan is paused at a potential more positive than the critical value. This indicates that the hysteresis is the result of the slowness of the restoration of the inhibiting film after its removal.

- The importance of Cl^- in regulating the effectiveness of PEG as an inhibitor was highlighted in some of these experiments. After the inhibition of Cu^{2+} reduction is lost at intermediate concentrations when the potential falls below the critical potential, it can be restored if the HCl concentration is raised.

- Evidence that PEG can adsorb in the presence of Cl^- in a Cu^{2+}–free solution was found. However, the film so formed does not strongly inhibit copper deposition when subsequently immersed in a $CuSO_4$ solution. The only way to obtain a strongly inhibiting effect is for Cl^- and PEG to be simultaneously present in the solution where Cu^{2+} is being reduced.

A model more comprehensive than those considered in previous studies was developed in Chapter 5 to describe the electrode responses of Cu^{2+} reduction in the presence of various concentrations of Cl^- and PEG. The contributions of this chapter are summarized as follows:

- The model is able to predict the different shapes of the current–potential curves over a wide range of PEG and Cl^- concentrations as well as the impedance spectra obtained at high and low additive concentrations.

- Key aspects of the model that enable it to predict the effect of PEG and Cl^- on the electrode response are the distinction made between the condition when the electrode is completely covered by the film and when it is partially covered and the non–linear nature of the PEG desorption rate. This nonlinearity arises from the assumption that PEG is displaced from the surface by the deposition of copper.

- At intermediate additive concentrations, the PEG desorption rate is only slightly higher than its adsorption rate during the cathodic scan until it reaches a critical potential, whereupon it rises very sharply to activate the electrode.

- The critical potential was found to be highly sensitive to the estimates of the kinetic parameters.

- Analysis of the model under steady state conditions shows that it permits two physically possible solutions over a range of potentials at the intermediate additive concentrations. This range correlates well with where hysteresis is observed in the experimental current–potential curves. One branch appears to be associated with the response during the forward scan and the other branch with the reverse scan.

- The depletion of Cu^{2+} in the vicinity of the electrode during the reverse scan was found to be responsible for the hysteresis observed in current–potential curves.
- The model was used to predict some of the experimental results of Chapter 4. For example, the model successfully predicts the restoration of inhibition when the Cl^- concentration is increased from 0.1 mM to 1.0 mM at a potential below the critical potential.

6.2 Directions for Future Research

The following suggestions are proposed to complement the study of adsorption and desorption of Cl^- and PEG in Chapter 4:

- The series II experiments in this study in which PEG and Cl^- were added in stages to investigate the dynamics of inhibiting film formation were carried out at a specific potential. A similar series of experiments should be done at different potentials. These experiments would reveal useful information regarding the potential dependence of the dynamics of adsorption and desorption of the inhibiting film.
- Interesting changes in the dynamics of the formation of the inhibiting film with increments in the concentration of Cl^- and/or PEG were found in the series II experiments in Figs. 4.14 and 4.15. Since additives cannot be removed from the electrolytic solution, it was impossible to study with this type of experiment the effect of the concentrations of Cl^- and PEG on the dynamics of the desorption of the inhibiting film. However, the design of a micro–fluidic cell such as that described in [124] allows the solution in the cell to be exchanged by another with a different composition during a continuous measurement. Thus, the concentrations of Cl^- and/or PEG can be reduced from one solution to the other by small amounts. The exchange of the solutions can be repeated several times to study the desorption of the inhibiting film over a wide range of PEG and Cl^- concentrations.

Future research is proposed to make further improvements to the model developed in Chapter 5. The following directions are proposed:

- The adsorption of PEG in the current model is assumed to proceed according to a 1:1 mole ratio of PEG and $CuCl_{(ads)}$ to form the inhibiting complex. From previous studies, it is likely that more than one Cl^- linkage participates in the adsorption of PEG although the exact number is unknown. Moreover, this number may change during adsorption and desorption according to the conformation of each PEG molecule. The model could be further improved by allowing for the fact that more than one Cl^- linkage can be associated with each adsorbed PEG molecule. With this modification, the adsorption of PEG particularly when present at high concentrations will be more sensitive to the number of actual Cl^- adsorbed. It is hoped that this will enable the model to predict the limit in the current–potential curves observed when the PEG concentration is increased beyond a maximum value and the Cl^- concentration has an intermediate value such as 0.1 mM.

- The change in PEG conformation during adsorption and desorption should lead to variation in film thickness. The model distinguishes between the conditions when the electrode is completely and partially covered, but no consideration of the change in the film thickness was made. An extension of the model accounting for the change in the film thickness would predict more retardation of Cu^{2+} reduction in the presence of a thicker film.

- This model should be complemented with a dynamical stability analysis. This analysis could reveal useful information concerning the jump from inhibited state to activated state and onset of hysteresis observed in some current–potential curves.

- This model could be used to predict the filling of vias and trenches in the presence of Cl^- and PEG alone. This would provide further insight into how superfilling is achieved in the presence of these additives alone.

- This model can also be extended to account for the effect of other additives such as MPS or SPS to describe copper electrodeposition on planar electrodes and in vias and trenches from solutions containing MPS, PEG and Cl^- together.

References

[1] P. C. Andricacos. Copper on chip interconections. A breakthrough in electrodeposition to make better chips. *Electrochemical Society Interface*, 8(1):32–37, 1999.

[2] E. W. Thompson. Acid copper plating for electronics. *Transactions of the Institute of Metal Finishing*, 59(1):30–32, 1981.

[3] Y. Cao, P. Taephaisitphongse, R. Chalupa, and A. C. West. Three-additive model of superfilling of copper. *Journal of the Electrochemical Society*, 148(7):C466–C472, 2001.

[4] W.-P. Dow, H.-S. Huang, and Z. Lin. Interactions between brightener and chloride ions on copper electroplating for laser-drilled via-hole filling. *Electrochemical and Solid-State Letters*, 6(9):C134–C136, 2003.

[5] W.-P. Dow and H.-S. Huang. Roles of chloride ion in microvia filling by copper electrodeposition. I. Studies using SEM and optical microscope. *Journal of the Electrochemical Society*, 152(2):C67–C76, 2005.

[6] W.-P. Dow, H.-S. Huang, M.-Y. Yen, and H.-S. Wang. Influence of convection-dependent adsorption of additives on microvia filling by copper electroplating. *Journal of the Electrochemical Society*, 152(6):C425–C434, 2005.

[7] W.-P. Dow, M.-Y. Yen, W.-B. Lin, and S.-W. Ho. Influence of molecular weight of polyethylene glycol on microvia filling by copper electroplating. *Journal of the Electrochemical Society*, 152(11):C769–C775, 2005.

[8] M. Hasegawa, , and T. Osaka. Effects of additives on copper electrodeposition in

submicrometer trenches. *Journal of the Electrochemical Society*, 152(4):C221–C228, 2005.

[9] D. Josell, B. Baker, C. Witt, D. Wheeler, and T. P. Moffat. Via filling by electrodeposition: Superconformal silver and copper and conformal nickel. *Journal of the Electrochemical Society*, 149(12):C637–C641, 2002.

[10] M. Kang, M. E. Gross, and A. A. Gewirth. Atomic force microscopy examination of Cu electrodeposition in trenches. *Journal of the Electrochemical Society*, 150(5):C292–C301, 2003.

[11] J. J. Kelly and A. C. West. Leveling of 200 nm features by organic additives. *Electrochemical and Solid-State Letters*, 2(11):561–563, 1999.

[12] S.-K. Kim and J. J. Kim. Superfilling evolution in Cu electrodeposition. Dependence on the aging time of the accelerator. *Journal of the Electrochemical Society*, 7(9):C98–C100, 2004.

[13] K. Kondo, N. Yamakawa, Z. Tanaka, and K. Hayashi. Copper Damascene electrodeposition and additives. *Journal of Electroanalytical Chemistry*, 559(15):137–142, 2003.

[14] T. P. Moffat, J. E. Bonevich, W. H. Huber, A. Stanishevsky, D. R. Kelly, G. R. Stafford, and D. Josell. Superconformal electrodeposition of copper in 500-900 nm features. *Journal of the Electrochemical Society*, 147(12):4524–4535, 2000.

[15] T. P. Moffat, D. Wheeler, C. Witt, and D. Josell. Superconformal electrodeposition using derivitized substrates. *Electrochemical and Solid-State Letters*, 5(12):C110–C112, 2002.

[16] T. P. Moffat, D. Wheeler, M. D. Edelstein, and D. Josell. Superconformal film growth: mechanism and quantification. *IBM Journal of Research and Development*, 49(1):19–36, 2005.

[17] P. Taephaisitphongse, Y. Cao, and A. C. West. Electrochemical and fill studies of a multicomponent additive package for copper deposition. *Journal of the Electrochemical Society*, 148(7):C492–C497, 2001.

[18] J. E. Bauerle. Study of solid electrolyte polarization by a complex admittance method. *Journal of Physics and Chemistry of Solids*, 30(12):2657–2670, 1969.

[19] C. Ji, G. Oskam, and P. C. Searson. Electrodeposition of copper on silicon from sulfate solution. *Journal of the Electrochemical Society*, 148(11):C746–C752, 2001.

[20] V. D. Jović and B. M. Jović. Copper electrodeposition from copper acid baths in the presence of PEG and NaCl. *Journal of the Serbian Chemical Society*, 66(11-12):935–952, 2001.

[21] J. G. Long, P. C. Searson, and P. M. Vereecken. Electrochemical characterization of adsorption-desorption of the cuprous-suppressor-chloride complex during electrodeposition of copper. *Journal of the Electrochemical Society*, 153(4):C258–C264, 2006.

[22] X. Wu, H. Ma, S. Chen, Z. Xu, and A. Sui. General equivalent circuits for faradaic electrode processes under electrochemical reaction control. *Journal of the Electrochemical Society*, 146(5):1847–1853, 1999.

[23] K.-M. Yin and L. I. Lu. Parametric study on the electrochemical impedance spectroscopy of organic-coated steels in hydrochloric acid solutions. *Journal of Coatings Technology*, 75(941):65–72, 2003.

[24] P. Zhang, T. J. O'Keefe, and P. Yu. Electrochemical characterization of the effects of impurities and organic additives in lead electrowinning from fluoborate electrolyte. *Hydrometallurgy*, 61(3):207–221, 2001.

[25] J. R. Macdonald. *Impedance Spectroscopy.* John Wiley and Sons, 1987.

[26] B. C. Baker and A. C. West. Electrochemical impedance spectroscopy study of nickel-iron deposition. I. Experimental results. *Journal of the Electrochemical Society*, 144(1):164–169, 1997.

[27] B. C. Baker and A. C. West. Electrochemical impedance spectroscopy study of nickel-iron deposition. II. Theoretical interpretation. *Journal of the Electrochemical Society*, 144(1):169–175, 1997.

[28] E. Chassaing and R. Wiart. Epitaxial growth and electrode impedance of copper electrodeposits. *Electrochimica Acta*, 29(5):649–660, 1984.

[29] C.-C. Cheng and A. C. West. Nickel deposition in the presence of coumarin: An electrochemical impedance spectroscopy study. *Journal of the Electrochemical Society*, 144(9):3050–3056, 1997.

[30] C. Gabrielli, P. Moçotéguy, H. Perrot, and R. Wiart. Mechanism of copper deposition in a sulphate bath containing chlorides. *Journal of Electroanalytical Chemistry*, 572(2):367–375, 2004.

[31] C. Gabrielli, P. Moçotéguy, H. Perrot, D. Nieto-Sanz, and Z. Zdunek. A model for copper deposition in the Damascene process. *Electrochimica Acta*, 51(8-9):1462–1472, 2006.

[32] A. K. Hauser and J. Newman. Singular perturbation analysis of the faradaic impedance of copper dissolution accounting for the effects of finite rates of a homogeneous reaction. *Journal of the Electrochemical Society*, 136(10):2820–2831, 1989.

[33] R. V. Homsy and J. Newman. An asymptotic solution for the Warburg impedance of a rotating disk electrode. *Journal of the Electrochemical Society*, 121(4):521–523, 1974.

[34] R. Ichino, C. Cachet, and R. Wiart. Mechanism of zinc electrodeposition in acidic sulfate electrolytes containing Pb^{2+} ions. *Electrochimica Acta*, 41(7-8):1031–1039, 1996.

[35] J. J. Kelly and A. C. West. Copper deposition in the presence of polyethylene glycol. II. Electrochemical impedance spectroscopy. *Journal of the Electrochemical Society*, 145(10):3477–3481, 1998.

[36] S. Krzewska. Impedance investigation of the mechanism of copper electrodeposition from acidic perchlorate electrolyte. *Electrochimica Acta*, 42(23-24):3531–3540, 1997.

[37] L. Muresan, L. Oniciu, and R. Wiart. On the kinetics of lead electrodeposition in fluorosilicate electrolyte. Part I: Inhibiting effect of sodium lignin sulphonate. *Journal of Applied Electrochemistry*, 23(1):66–71, 1993.

[38] L. Muresan, L. Oniciu, and R. Wiart. Kinetics of lead deposition in fluorosilicate electrolyte. Part II: Inhibiting effect of horse-chestnut extract (HCE) and of sodium lignin sulphonate-HCE mixtures. *Journal of Applied Electrochemistry*, 24(4):332–336, 1994.

[39] D. A. Scherson and J. Newman. The Warburg impedance in the presence of convective flow. *Journal of the Electrochemical Society*, 127(1):110–113, 1980.

[40] B. Tribollet and J. Newman. The modulated flow at a rotating disk electrode. *Journal of the Electrochemical Society*, 130(10):2016–2026, 1983.

[41] A. A. Gewirth, P. C. Andricacos, and J. A. Switzer. Hot topics in electrodeposition. *Electrochemical Society Interface*, 7(1):22–25, 1998.

[42] C.-K. Hu and J. M. E. Harper. Copper interconnections and reliability. *Materials Chemistry and Physics*, 52(1):5–16, 1998.

[43] A. Radisic, Y. Cao, P. Taephaisitphongse, A. C. West, and P. C. Searson. Direct copper electrodeposition on TaN barrier layers. *Journal of the Electrochemical Society*, 150(5):C362–C367, 2003.

[44] P. C. Andricacos, C. Huzch, J. O. Dukovic, J. Harkans, and H. Deligianni. Damascene copper electroplating for chip interconections. *IBM Journal of Research and Development*, 42(5):567–574, 1998.

[45] D. Padhi, J. Yahalom, S Gandikota, and G. Dixit. Planarization of copper thin films by electropolishing in phosphoric acid for ULSI applications. *Journal of the Electrochemical Society*, 150(1):G10–G14, 2003.

[46] D. Josell, D. Wheeler, W. H. Huber, J. E. Bonevich, and T. P. Moffat. A simple equation for predicting superconformal electrodeposition in submicrometer trenches. *Journal of the Electrochemical Society*, 148(12):C767–C773, 2001.

[47] T. P. Moffat, D. Wheeler, W. H. Huber, and D. Josell. Superconformal electrodeposition of copper. *Electrochemical and Solid-State Letters*, 4(4):C26–C29, 2001.

[48] S. K. Cho, S.-K. Kim, and J. J. Kim. Superconformal Cu electrodeposition using DPS. A substitutive accelerator for bis(3-sulfopropyl) disulfide. *Journal of the Electrochemical Society*, 152(5):C330–C333, 2005.

[49] M. Hayase, M. Taketani, K. Aizawa, T. Hatsuzawa, and K. Hayabusa. Copper bottom up deposition by breakdown of PEG-Cl inhibition. *Electrochemical and Solid-State Letters*, 5(10):C98–C101, 2002.

[50] M. Hayase, M. Taketani, T. Hatsuzawa, and K. Hayabusa. Preferential copper electrodeposition at submicrometer trenches by consumption of halide ion. *Electrochemical and Solid-State Letters*, 6(6):C92–C95, 2003.

[51] T. Kobayashi, J. Kawasaki, K. Mihara, and H. Honma. Via-filling using electroplating for build-up PCBs. *Electrochimica Acta*, 47(1):85–89, 2001.

[52] J. Reid, C. Gack, and S. J. Hearne. Cathodic depolarization effect during Cu electroplating on patterned wafers. *Electrochemical and Solid-State Letters*, 6(2):C26–C29, 2003.

[53] A. C. West, S. Mayer, and J. Reid. A superfilling model that predicts bump formation. *Electrochemical and Solid-State Letters*, 4(7):C50–C53, 2001.

[54] B.-H. Wu, C.-C. Wan, and Y.-Y. Wang. Void-free anisotropic deposition for IC interconnect with polyethylene glycol as the single additive based on uneven adsorption distribution. *Journal of Applied Electrochemistry*, 33(9):823–830, 2003.

[55] D. Varandarajan, C. Y. Lee, A. Krishnamoorthy, D. J. Duquette, and W. N. Gill. A tertiary current distribution model for the pulse plating of copper into high aspect ratios sub-0.25 μm trenches. *Journal of the Electrochemical Society*, 147(9):3382–3392, 2000.

[56] M. Kang and A. A. Gewirth. Influence of additives on copper electrodeposition on physical vapor deposited (PVD) copper substrates. *Journal of the Electrochemical Society*, 150(6):C426–C434, 2003.

[57] A. Radisic, A. C. West, and P. C. Searson. Influence of additives on nucleation and growth of copper on n−Si(111) from acidic sulfate solutions. *Journal of the Electrochemical Society*, 149(2):C94–C99, 2002.

[58] J. J. Kelly, C. Tian, and A. C. West. Leveling and microstructural effects of additives for copper electrodeposition. *Journal of the Electrochemical Society*, 146(7):2540–2545, 1999.

[59] M. Hasegawa, Y. Okinaka, Y. Shacham-Diamand, and T. Osaka. Void-free trench-filling by electroless copper deposition using the combination of accelerating and inhibiting additives. *Electrochemical and Solid-State Letters*, 9(8):C138–C140, 2006.

[60] J. O'M. Bockris and A. K. N. Reddy. *Modern Electrochemistry*, volume 2. Plenum/Rosseta, 1970.

[61] A. J. Bard and L. R. Faulker. *Electrochemical Methods. Fundamentals and Applications.* John Wiley and Sons, Inc., 1980.

[62] D. D. Macdonald. *Transient Techniques in Electrochemistry.* Plenum Press, 1977.

[63] K. M. Gorbunova and Z. A. Tkachik. Copper electrocrystallization mechanism according to morphological data and impedance measurements. *Electrochimica Acta*, 16(2):191–200, 1971.

[64] J. D. Reid and A. P. David. Impedance behavior of a sulfuric acid-cupric sulfate/copper cathode interface. *Journal of the Electrochemical Society*, 134(6):1389–1394, 1987.

[65] W.-C. Tsai, C.-C. Wan, and Y.-Y. Wang. Frequency effect of pulse plating on the uniformity of copper deposition in plated through holes. *Journal of the Electrochemical Society*, 150(5):C267–C272, 2003.

[66] R. Wiart. Elementary steps of electrodeposition analysed by means of impedance spectroscopy. *Electrochimica Acta*, 35(10):1587–1593, 1990.

[67] G. Fabricius and G. Sundholm. The effect of additives on the electrodeposition of copper studied by the impedance technique. *Journal of Applied Electrochemistry*, 15(6):797–801, 1985.

[68] C. Gabrielli, P. Moçotéguy, H. Perrot, A. Zdunek, P. Bouard, and M. Haddix. Electrochemical impedance spectroscopy investigation of bath aging in Damascene process chemistries. *Electrochemical and Solid-State Letters*, 7(3):C31–C34, 2004.

[69] S. Goldbach, W. Messing, T. Daenen, and F. Lapicque. Coupled effects of chloride ions and branch chained polypropylene ether $\mathrm{LP}-1$ on the electrochemical deposition of copper from sulfate solutions. *Electrochimica Acta*, 44(2-3):323–335, 1998.

[70] J. D. Reid and A. P. David. Effects of polyethylene glycol on the electrochemical characteristics of copper cathodes in an acid copper medium. *Plating and Surface Finishing*, 74(1):66–70, 1987.

[71] S. Varvara, L. Muresan, I. C. Popescu, and G. Maurin. Kinetics of copper electrodeposition in the presence of triethyl-benzyl ammonium chloride. *Journal of Applied Electrochemistry*, 33(8):685–692, 2003.

[72] A. Lasia. Electrochemical impedance spectroscopy and its applications. In B. E. Conway, J. O'M. Bockris, and R. E. White, editors, *Modern Aspects of Electrochemistry*, volume 32, pages 143–248. Kluer Academic/Plenum, 1999.

[73] M. E. Huerta Garrido and M. D. Pritzker. EIS and statistical analysis of copper electrodeposition accounting for multi-component transport and reactions. *Journal of Electroanalytical Chemistry*, 594(2):118–132, 2006.

[74] R. Caban and T. W. Chapman. Statistical analysis of electrode kinetics measurements–copper deposition from $\mathrm{C}u\mathrm{SO}_4 - \mathrm{H}_2\mathrm{SO}_4$ solutions. *Journal of the Electochemical Society*, 124(9):1371–1379, 1977.

[75] E. E. Farndon, F. C. Walsh, and S. A. Campbell. Effect of thiourea, benzotriazole and 4,5-dithiaoctane-1,8-disulphonic acid on the kinetics of copper deposition from dilute acid sulphate solutions. *Journal of Applied Electrochemistry*, 25(6):574–583, 1995.

[76] E. Mattsson and J. O'M. Bockris. Galvanostatic studies of the kinetics of deposition and dissolution in the copper+copper sulfate system. *Transactions of the Faraday Society*, 55(9):1586–1601, 1959.

[77] N. Tantavichet and M. D. Pritzker. Low and high frequency pulse current plating of copper onto a rotating disk electrode. *Journal of the Electrochemical Society*, 149(5):C289–C299, 2002.

[78] N. Tantavichet and M. D. Pritzker. Low and high frequency pulse current and pulse reverse plating of copper. *Journal of the Electrochemical Society*, 150(10):C665–C677, 2003.

[79] M. Yokoi, S. Konishi, and T. Hayashi. Mechanism of electrodeposition and dissolution of copper in an acid copper sulfate bath. II. Mixed controlled reaction model. *Denki Kagaku*, 50(12):941–945, 1982.

[80] V. G. Levich. *Physicochemical Hydrodynamics*. Prentice-Hall, Inc., 1962.

[81] G. Fabricius, K. Kontturi, and G. Sundholm. Influence of thiourea and thiourea ageing on the electrodeposition of copper from acid sulfate solutions studied by the ring-disc technique. *Journal of Applied Electrochemistry*, 26(11):1179–1183, 1996.

[82] L. Mirkova and S. Rashkov. Anodic behaviour of copper during electrorefining using a rotating ring-disc electrode. *Journal of Applied Electrochemistry*, 24(5):420–425, 1994.

[83] P. M. Vereecken, R. A. Binstead, H. Deligianni, and P. C. Andricacos. The chemistry of additives in Damascene copper plating. *IBM Journal of Research and Development*, 49(1):3–18, 2005.

[84] S. Yoon, M. Schwartz, and K. Nobe. Rotating ring-disk electrode studies of copper electrodeposition: Effect of chloride ions and organic additives. *Plating and Surface Finishing*, 81(12):65–74, 1994.

[85] D. P. Barkey, F. Oberholtzer, and Q. Wu. A reaction-plane model for the open-circuit potential of copper in aerated copper sulfate solution. *Journal of the Electrochemical Society*, 145(2):590–595, 1998.

[86] D. Hua and D. Barkey. Corrosion of copper in acid-sulfate plating baths with additives. *Plating and Surface Finishing*, 90(7):40–44, 2003.

[87] J. O'M. Bockris and M. Enyo. Mechanism of electrodeposition and dissolution processes of copper in aqueous solutions. *Transactions of the Faraday Society*, 58:1187–1202, 1962.

[88] O. R. Brown and H. R. Thirsk. The rate-determining step in the electrodeposition of copper on copper from aqueous cupric sulphate solutions. *Electrochimica Acta,*, 10(4):383–393, 1965.

[89] B.-H. Wu, C.-C. Wan, and Y.-Y. Wang. Modeling of acid copper anisotropic deposition based on detailed calculation of the electrolyte composition. *Journal of the Electrochemical Society*, 150(1):C7–C15, 2003.

[90] MATLAB, 2004. the MATH WORKS Inc., Version 7.0.1.

[91] L. F. Shampine, J. Kierzenka, and M. W. Reichelt. Solving boundary value problems for ordinary differential equations in MATLAB with bvp4c. [Online] ftp://ftp.mathworks.com/pub/doc/papers/bvp, 2000.

[92] MATLAB help, September (2004). version 7.0.1.

[93] J. S. Newman. *Electrochemical Systems.* Prentice Hall, 1991.

[94] R. Chang. *Chemistry.* McGraw–Hill, 1998.

[95] M. E. Huerta Garrido and M. D. Pritzker. Reply to "Remarks on 'EIS and statistical analysis of copper electrodeposition accounting for multi-component transport and reactions' [M. E. Huerta Garrido, M. D. Pritzker, J. Electroanal. Chem. 594 (2006) 118]" by A. Lasia. *Journal of Electroanalytical Chemistry*, 2007. Submitted for publication.

[96] N. R. Draper and H. Smith. *Applied Regression Analysis.* John Wiley and Sons, 1981.

[97] D. M. Bates and D. G. Watts. *Nonlinear Regression Analysis and its Applications.* John Wiley and Sons, 1988.

[98] P. Agarwal, M. E. Orazem, and L. H. Garcia-Rubio. Measurement models for electrochemical impedance spectroscopy. I. Demonstration of applicability. *Journal of the Electrochemical Society*, 139(7):1917–1927, 1992.

[99] P. Agarwal, O. D. Crisalle, M. E. Orazem, and L. H. Garcia-Rubio. Application of measurement models to impedance spectroscopy. II. Determination of the stochastic contribution to the error structure. *Journal of the Electrochemical Society*, 142(12):4149–4158, 1995.

[100] P. Agarwal, M. E. Orazem, and L. H. Garcia-Rubio. Application of measurement models to impedance spectroscopy. III. Evaluation of consistency with the Kramers-Kronig relations. *Journal of the Electrochemical Society*, 142(12):4159–4168, 1995.

[101] M. E. Huerta Garrido and M. D. Pritzker. Voltammetric study of the inhibition effect of polyethylene glycol and chloride ions on copper deposition. *Journal of the Electrochemical Society*, 2007. Submitted for publication.

[102] D. Josell, D. Wheeler, W. H. Huber, and T. P. Moffat. Superconformal electrodeposition in submicron features. *Physical Review Letters*, 87(1):016102/1–016102/4, 2001.

[103] D. Josell, D. Wheeler, and T. P. Moffat. Superconformal electrodeposition in vias. *Electrochemical and Solid-State Letters*, 5(4):C49–C52, 2002.

[104] D. Wheeler, D. Josell, and T. P. Moffat. Modeling superconformal electrodeposition using the level set method. *Journal of the Electrochemical Society*, 150(5):C302–C310, 2003.

[105] R. Akolkar and U. Landau. A time-dependent transport-kinetics model for additive interactions in copper interconnect metallization. *Journal of the Electrochemical Society*, 151(11):C702–C711, 2004.

[106] W.-P. Dow, H.-S. Huang, M.-Y. Yen, and H.-H. Chen. Roles of chloride ion in microvia filling by copper electrodeposition. II. Studies using EPR and galvanostatic measurements. *Journal of the Electrochemical Society*, 152(2):C77–C88, 2005.

[107] K. R. Hebert. Analysis of current-potential hysteresis during electrodeposition of copper with additives. *Journal of the Electrochemical Society*, 148(11):C726–C732, 2001.

[108] T. P. Moffat, D. Wheeler, and D. Josell. Electrodeposition of copper in the SPS-PEG-Cl additive system. I. Kinetic measurements: influence of SPS. *Journal of the Electrochemical Society*, 151(4):C262–C271, 2004.

[109] M. Tan and J. N. Harb. Additive behavior during copper electrodeposition in solutions containing Cl^-, PEG, and SPS. *Journal of the Electrochemical Society*, 150(6):C420–C425, 2003.

[110] L. D. Burke, A. M. O'Connell, R. Sharna, and C. A. Buckley. Involvement of a metastable surface state in the electrocatalytic, electrodeposition and bath additive behaviour of copper in acid solution. *Journal of Applied Electrochemistry*, 36(8):919–929, 2006.

[111] J. P. Healy, D. Pletcher, and M. Goodenough. The chemistry of the additives in an acid copper electroplating bath. Part I. Polyethylene glycol and chloride ion. *Journal of Electroanalytical Chemistry*, 338(1-2):155–165, 1992.

[112] M. Petri, D. M. Kolb, U. Memmert, and H. Meyer. Adsorption of PEG on Au(111) single-crystal electrodes and its influence on copper deposition. *Journal of the Electrochemical Society*, 151(12):C793–C797, 2004.

[113] M. Yokoi, S. Konishi, and T. Hayashi. Adsorption behaviour of polyoxyethyleneglycole on the copper surface in an acid copper sulfate bath. *Denki Kagaku*, 52(4):218–223, 1984.

[114] L. Bonou, M. Eyraud, R. Denoyel, and Y. Massiani. Influence of additives on Cu electrodeposition mechanisms in acid solution: direct current study supported by non-electrochemical measurements. *Electrochimica Acta*, 47(26):4139–4148, 2002.

[115] D. Stoychev and C. Tsvetanov. Behaviour of poly(ethylene glycol) during electrodeposition of bright copper coatings in sulfuric acid electrolytes. *Journal of Applied Electrochemistry*, 26(7):741–749, 1996.

[116] J. J. Kelly and A. C. West. Copper deposition in the presence of polyethylene glycol. I. Quartz crystal microbalance study. *Journal of the Electrochemical Society*, 145(10):3472–3476, 1998.

[117] N. Tantavichet and M. D. Pritzker. Effect of plating mode, thiourea and chloride on the morphology of copper deposits produced in acidic sulphate solutions. *Electrochimica Acta*, 50(9):1849–1861, 2005.

[118] M. Eyraud, S. Kologo, L. Bonou, and Y. Massiani. Effect of additives on Cu electrodeposits: electrochemical study coupled with EQCM measurements. *Journal of Electroceramics*, 16(1):55–63, 2006.

[119] Z. V. Feng, X. Li, and A. A. Gewirth. Inhibition due to the interaction of polyethylene glycol, chloride, and copper in plating baths: a surface-enhanced raman study. *Journal of Physical Chemistry B*, 107(35):9415–9423, 2003.

[120] D. S. Stoychev, I. Vitanova, St. Rashkov, and T. Vitanov. Adsorption of substances acting as brighteners in the electrolytic deposition of copper. *Surface Technology*, 7(6):427–432, 1974.

[121] M. L. Walker, L. J. Richter, and T. P. Moffat. In situ ellipsometric study of PEG/Cl^- coadsorption on Cu, Ag, Au. *Journal of The Electrochemical Society*, 152(6):C403–C407, 2005.

[122] M. R. H. Hill and G. T. Rogers. Polyethylene glycol in copper electrodeposition onto a rotating disk electrode. *Journal of Electroanalytical Chemistry*, 86(1):179–188, 1978.

[123] T. Pearson and J. K. Dennis. The effect of pulsed reverse current on the polarization behaviour of acid copper plating solutions containing organic additives. *Journal of Applied Electrochemistry*, 20(2):196–208, 1990.

[124] M. J. Willey and A. C. West. Microfluidic studies of adsorption and desorption of polyethylene glycol during copper electrodeposition. *Journal of the Electrochemical Society*, 153(10):C728–C734, 2006.

[125] B. Bozzini, L. D'Urzo, C. Mele, and V. Romanello. Electrodeposition of Cu from acidic sulphate solutions in the presence of polyethylene glycol and chloride ions. *Journal of Materials Science: Materials in Electronics*, 17(11):915–923, 2006.

[126] R. Ding, X. Zhang, J. W. Evans, and F. M. Doyle. EQCM study of the influence of copper ions on the adsorption of polyethylene glycol and bis(sodiumsulfopropyl) disulfide at a copper cathode. In F. M. Doyle, G. H. Kelsall, and R. Woods, editors, *ECS Transactions*, volume 2, pages 281–292. The Electrochemical Society, 2006.

[127] K. Doblhofer, S. Wasle, D. M. Soares, K. G. Weil, and G. Ertl. An EQCM study of the electrochemical copper(II)/copper(I)/copper system in the presence of PEG and chloride ions. *Journal of the Electrochemical Society*, 150(10):C657–C664, 2003.

[128] K. Kondo, T. Matsumoto, and K. Watanabe. Role of additives for copper Damascene electrodeposition. Experimental study on inhibition and acceleration effects. *Journal of the Electrochemical Society*, 151(4):C250–C255, 2004.

[129] Z. Nagy, J. P. Blaudeau, N. C. Hung, L. A. Curtiss, and D. J. Zurawski. Chloride ion catalysis of the copper deposition reaction. *Journal of the Electrochemical Society*, 142(6):L87–L89, 1995.

[130] K. R. Hebert. Role of chloride ions in suppression of copper electrodeposition by polyethylene glycol. *Journal of The Electrochemical Society*, 152(5):C283–C287, 2005.

[131] G.-S. Kim, T. Merchant, J. D'Urso, L. A. Gochberg, and K. F. Jensen. Systematic study of surface chemistry and comprehensive two-dimensional tertiary current distribution model for copper electrochemical deposition. *Journal of the Electrochemical Society*, 153(11):C761–C772, 2006.

[132] B. A. Finlayson. *Nonlinear Analysis in Chemical Engineering.* McGraw-Hill, 1980.

[133] L. Masaro, X. X. Zhu, and P. M. Macdonald. Self-diffusion of oligo- and poly(ethylene glycol)s in poly(vinyl alcohol) aqueous solutions as studied by pulsed-gradient NMR spectroscopy. *Macromolecules*, 31(12):3880–3885, 1998.

Appendix A

Linearization

The linearization procedure of the EIS models presented in Chapters 3 and 5 is shown in more detail in this appendix. The expressions for the applied potential and all other time-dependent variables such as concentration, surface coverage, current density and solution potential are expressed as

$$E(t) = \overline{E} + \mathrm{Re}\left\{\widetilde{E}\exp(\mathrm{j}\omega t)\right\}, \tag{A.1}$$

$$y(t) = \overline{y} + \mathrm{Re}\left\{\widetilde{y}\exp(\mathrm{j}\omega t)\right\}. \tag{A.2}$$

A.1 Additive-free Model

Although an explicit expression for $R_i(z,t)$ is not defined in this problem, it will have the same form as any other response variable, *i.e.*, $R_i(t) = \overline{R}_i + \mathrm{Re}\left\{\widetilde{R}_i\exp(\mathrm{j}\omega t)\right\}$. This assumption does not affect the final expression obtained. The following expressions result from substituting Eq. (A.2) for each dependent variable into Eq. (3.2):

$$\begin{aligned}\frac{\partial\left(\overline{C}_i + \mathrm{Re}\left\{\widetilde{C}_i\exp(\mathrm{j}\omega t)\right\}\right)}{\partial t} &= D_i\frac{\partial^2\left(\overline{C}_i + \mathrm{Re}\left\{\widetilde{C}_i\exp(\mathrm{j}\omega t)\right\}\right)}{\partial z^2}\\ &- v_z\frac{\partial\left(\overline{C}_i + \mathrm{Re}\left\{\widetilde{C}_i\exp(\mathrm{j}\omega t)\right\}\right)}{\partial z}\\ &+ \frac{z_iD_iF}{RT}\frac{\partial}{\partial z}\left(\left(\overline{C}_i + \mathrm{Re}\left\{\widetilde{C}_i\exp(\mathrm{j}\omega t)\right\}\right)\frac{\partial\left(\overline{\phi}_\mathrm{s} + \mathrm{Re}\left\{\widetilde{\phi}_\mathrm{s}\exp(\mathrm{j}\omega t)\right\}\right)}{\partial z}\right)\\ &+ \overline{R}_i + \mathrm{Re}\left\{\widetilde{R}_i\exp(\mathrm{j}\omega t)\right\},\ \textit{on}\ 0 < z < 3\delta,\end{aligned} \tag{A.3}$$

This leads to

$$\begin{aligned}\mathrm{Re}\left\{\mathrm{j}\omega\widetilde{C}_i\exp\left(\mathrm{j}\omega t\right)\right\} &= D_i\frac{\mathrm{d}^2\overline{C}_i}{\mathrm{d}z^2}-\upsilon_z\frac{\mathrm{d}\overline{C}_i}{\mathrm{d}z}+\frac{z_iD_iF}{RT}\frac{\mathrm{d}}{\mathrm{d}z}\left(\overline{C}_i\frac{\mathrm{d}\overline{\phi}_\mathrm{s}}{\mathrm{d}z}\right)+\overline{R}_i\\ &+\mathrm{Re}\left\{\left(D_i\frac{\mathrm{d}^2\widetilde{C}_i}{\mathrm{d}z^2}-\upsilon_z\frac{\mathrm{d}\widetilde{C}_i}{\mathrm{d}z}+\frac{z_iD_iF}{RT}\frac{\mathrm{d}}{\mathrm{d}z}\left(\overline{C}_i\frac{\mathrm{d}\widetilde{\phi}_\mathrm{s}}{\mathrm{d}z}+\widetilde{C}_i\frac{\mathrm{d}\overline{\phi}_\mathrm{s}}{\mathrm{d}z}\right)+\widetilde{R}_i\right)\exp\left(\mathrm{j}\omega t\right)\right\}\\ &+\mathrm{Re}\left\{\frac{z_iD_iF}{RT}\frac{\mathrm{d}}{\mathrm{d}z}\left(\widetilde{C}_i\frac{\mathrm{d}\widetilde{\phi}_\mathrm{s}}{\mathrm{d}z}\right)\exp\left(2\mathrm{j}\omega t\right)\right\}\ \textit{on}\ 0<z<3\delta, \qquad \text{(A.4)}\end{aligned}$$

From the zeroth order condition, $D_i\frac{\mathrm{d}^2\overline{C}_i}{\mathrm{d}z^2}-\upsilon_z\frac{\mathrm{d}\overline{C}_i}{\mathrm{d}z}+\frac{z_iD_iF}{RT}\frac{\mathrm{d}}{\mathrm{d}z}\left(\overline{C}_i\frac{\mathrm{d}\overline{\phi}_\mathrm{s}}{\mathrm{d}z}\right)+\overline{R}_i=0$. Since a small-amplitude signal is used in the EIS technique, the term $\widetilde{C}_i\frac{\mathrm{d}\widetilde{\phi}_\mathrm{s}}{\mathrm{d}z}\exp\left(2\mathrm{j}\omega t\right)$ is neglected and Eq. (A.4) is reduced to

$$\mathrm{j}\omega\widetilde{C}_i=D_i\frac{\mathrm{d}^2\widetilde{C}_i}{\mathrm{d}z^2}-\upsilon_z\frac{\mathrm{d}\widetilde{C}_i}{\mathrm{d}z}+\frac{z_iD_iF}{RT}\frac{\mathrm{d}}{\mathrm{d}z}\left(\overline{C}_i\frac{\mathrm{d}\widetilde{\phi}_\mathrm{s}}{\mathrm{d}z}+\widetilde{C}_i\frac{\mathrm{d}\overline{\phi}_\mathrm{s}}{\mathrm{d}z}\right)+\widetilde{R}_i\ \textit{on}\ 0<z<3\delta. \qquad \text{(A.5)}$$

From the stoichiometric relations between the homogeneous rates of generation R_i of the five species i in the solution given in Eqs. (3.23)–(3.25), one obtains

$$\overline{R}_1+\mathrm{Re}\left\{\widetilde{R}_1\exp\left(\mathrm{j}\omega t\right)\right\}=-\overline{R}_4-\mathrm{Re}\left\{\widetilde{R}_4\exp\left(\mathrm{j}\omega t\right)\right\}, \qquad \text{(A.6)}$$

$$\overline{R}_2+\mathrm{Re}\left\{\widetilde{R}_2\exp\left(\mathrm{j}\omega t\right)\right\}=-\overline{R}_5-\mathrm{Re}\left\{\widetilde{R}_5\exp\left(\mathrm{j}\omega t\right)\right\}, \qquad \text{(A.7)}$$

$$\overline{R}_3+\mathrm{Re}\left\{\widetilde{R}_3\exp\left(\mathrm{j}\omega t\right)\right\}=-\left(\overline{R}_4+\mathrm{Re}\left\{\widetilde{R}_4\exp\left(\mathrm{j}\omega t\right)\right\}+\overline{R}_5+\mathrm{Re}\left\{\widetilde{R}_5\exp\left(\mathrm{j}\omega t\right)\right\}\right), \qquad \text{(A.8)}$$

Since $\overline{R}_1=-\overline{R}_4$, $\overline{R}_2=-\overline{R}_5$ and $\overline{R}_3=-\left(\overline{R}_4+\overline{R}_5\right)$, this leads to

$$\widetilde{R}_1=-\widetilde{R}_4, \qquad \text{(A.9)}$$

$$\widetilde{R}_2=-\widetilde{R}_5, \qquad \text{(A.10)}$$

$$\widetilde{R}_3=-\left(\widetilde{R}_4+\widetilde{R}_5\right). \qquad \text{(A.11)}$$

Then, Eqs. (A.9)–(A.11) are combined with (A.5) to yield

$$j\omega\widetilde{C}_1+j\omega\widetilde{C}_4=B_1+B_4, \qquad \text{(A.12)}$$

$$j\omega\widetilde{C}_2+j\omega\widetilde{C}_5=B_2+B_5, \qquad \text{(A.13)}$$

$$j\omega\widetilde{C}_3+j\omega\widetilde{C}_4+j\omega\widetilde{C}_5=B_3+B_4+B_5,, \qquad \text{(A.14)}$$

where

$$B_i = D_i \frac{\mathrm{d}^2 \widetilde{C}_i}{\mathrm{d}^2 z} - \upsilon_z \frac{\mathrm{d}\widetilde{C}_i}{\mathrm{d}z} + \frac{z_i D_i F}{RT} \frac{\mathrm{d}}{\mathrm{d}z} \left(\overline{C}_i \frac{\mathrm{d}\widetilde{\phi}_{\mathrm{s}}}{\mathrm{d}z} + \widetilde{C}_i \frac{\mathrm{d}\overline{\phi}_{\mathrm{s}}}{\mathrm{d}z} \right),\ i = 1, 2, .., 5.$$

The electroneutrality condition and the equilibrium conditions are written in terms of Eq. (A.2) as follows:

$$\begin{aligned} & z_1 \overline{C}_1 + z_1 \mathrm{Re}\left\{ \widetilde{C}_1 \exp(\mathrm{j}\omega t) \right\} + z_2 \overline{C}_2 + z_2 \mathrm{Re}\left\{ \widetilde{C}_2 \exp(\mathrm{j}\omega t) \right\} + z_3 \overline{C}_3 + z_3 \mathrm{Re}\left\{ \widetilde{C}_3 \exp(\mathrm{j}\omega t) \right\} \\ & \qquad + z_5 \overline{C}_5 + z_5 \mathrm{Re}\left\{ \widetilde{C}_5 \exp(\mathrm{j}\omega t) \right\} = 0, \end{aligned} \tag{A.15}$$

$$K' \overline{C}_4 + K' \mathrm{Re}\left\{ \widetilde{C}_4 \exp(\mathrm{j}\omega t) \right\} = \left(\overline{C}_1 + \mathrm{Re}\left\{ \widetilde{C}_1 \exp(\mathrm{j}\omega t) \right\} \right) \left(\overline{C}_3 + \mathrm{Re}\left\{ \widetilde{C}_3 \exp(\mathrm{j}\omega t) \right\} \right), \tag{A.16}$$

$$K" \overline{C}_5 + K" \mathrm{Re}\left\{ \widetilde{C}_5 \exp(\mathrm{j}\omega t) \right\} = \left(\overline{C}_2 + \mathrm{Re}\left\{ \widetilde{C}_2 \exp(\mathrm{j}\omega t) \right\} \right) \left(\overline{C}_3 + \mathrm{Re}\left\{ \widetilde{C}_3 \exp(\mathrm{j}\omega t) \right\} \right). \tag{A.17}$$

From the zeroth order problem, *i.e.*, $z_1 \overline{C}_1 + z_2 \overline{C}_2 + z_3 \overline{C}_3 + z_5 \overline{C}_5 = 0$, $K' \overline{C}_4 = \overline{C}_1\ \overline{C}_3$ and $K" \overline{C}_5 = \overline{C}_2\ \overline{C}_3$. Also, since the products $\widetilde{C}_1\ \widetilde{C}_3$ and $\widetilde{C}_2\ \widetilde{C}_3$ can be neglected, Eqs. (A.15)–(A.17) become

$$z_1 \widetilde{C}_1 + z_2 \widetilde{C}_2 + z_3 \widetilde{C}_3 + z_5 \widetilde{C}_5 = 0, \tag{A.18}$$

$$K' \widetilde{C}_4 = \widetilde{C}_1 \widetilde{C}_3, \tag{A.19}$$

$$K" \widetilde{C}_5 = \widetilde{C}_2 \widetilde{C}_3. \tag{A.20}$$

The conditions at the surface and bulk boundaries required to solve Eqs. (A.12)–(A.14) and (A.18)–(A.20) are written as

$$C_i(t, 3\delta) = C_i^{\mathrm{b}}, \tag{A.21}$$

$$\phi_{\mathrm{s}}(t, 3\delta) = 0, \tag{A.22}$$

$$\begin{aligned} & D_1 \left. \frac{\partial C_1}{\partial z} \right|_{z=0} + \frac{z_1 D_1 F}{RT} \left. \left(C_1(0,t) \frac{\partial \phi_{\mathrm{s}}}{\partial z} \right) \right|_{z=0} \\ & \qquad + D_4 \left. \frac{\partial C_4}{\partial z} \right|_{z=0} + \frac{z_4 D_i F}{RT} \left. \left(C_4(0,t) \frac{\partial \phi_{\mathrm{s}}}{\partial z} \right) \right|_{z=0} = r_1 - r_{-1}, \end{aligned} \tag{A.23}$$

$$\begin{aligned} & D_2 \left. \frac{\partial C_2}{\partial z} \right|_{z=0} + \frac{z_2 D_2 F}{RT} \left. \left(C_2(0,t) \frac{\partial \phi_{\mathrm{s}}}{\partial z} \right) \right|_{z=0} \\ & \qquad + D_5 \left. \frac{\partial C_5}{\partial z} \right|_{z=0} + \frac{z_5 D_5 F}{RT} \left. \left(C_5(0,t) \frac{\partial \phi_{\mathrm{s}}}{\partial z} \right) \right|_{z=0} = 0, \end{aligned} \tag{A.24}$$

$$
\begin{aligned}
D_3 \frac{\partial C_3}{\partial z}\bigg|_{z=0} &+ \frac{z_3 D_3 F}{RT}\left(C_3(0,t)\frac{\partial \phi_\mathrm{s}}{\partial z}\right)\bigg|_{z=0} \\
&+ D_4 \frac{\partial C_4}{\partial z}\bigg|_{z=0} + \frac{z_4 D_i F}{RT}\left(C_4(0,t)\frac{\partial \phi_\mathrm{s}}{\partial z}\right)\bigg|_{z=0} \\
&+ D_5 \frac{\partial C_5}{\partial z}\bigg|_{z=0} + \frac{z_5 D_5 F}{RT}\left(C_5(0,t)\frac{\partial \phi_\mathrm{s}}{\partial z}\right)\bigg|_{z=0} = 0.
\end{aligned}
\tag{A.25}
$$

Substitution of Eq. (A.2) into (A.21)–(A.25) gives

$$
\overline{C}_i(3\delta) + \mathrm{Re}\left\{\widetilde{C}_i(3\delta)\exp\left(\mathrm{j}\omega t\right)\right\} = C_i^\mathrm{b}, \tag{A.26}
$$

$$
\overline{\phi}_\mathrm{s}(3\delta) + \mathrm{Re}\left\{\widetilde{\phi}_\mathrm{s}(3\delta)\exp\left(\mathrm{j}\omega t\right)\right\} = 0, \tag{A.27}
$$

$$
\begin{aligned}
D_1 &\frac{\partial\left(\overline{C}_1 + \mathrm{Re}\left\{\widetilde{C}_1\exp\left(\mathrm{j}\omega t\right)\right\}\right)}{\partial z}\Bigg|_{z=0} \\
&+ \frac{z_1 D_1 F}{RT}\left(\left(\overline{C}_1(0) + \mathrm{Re}\left\{\widetilde{C}_1(0)\exp\left(\mathrm{j}\omega t\right)\right\}\right)\frac{\partial\left(\overline{\phi}_\mathrm{s} + \mathrm{Re}\left\{\widetilde{\phi}_\mathrm{s}\exp\left(\mathrm{j}\omega t\right)\right\}\right)}{\partial z}\right)\Bigg|_{z=0} \\
&+ D_4 \frac{\partial\left(\overline{C}_4 + \mathrm{Re}\left\{\widetilde{C}_4\exp\left(\mathrm{j}\omega t\right)\right\}\right)}{\partial z}\Bigg|_{z=0} \\
&+ \frac{z_4 D_4 F}{RT}\left(\left(\overline{C}_4(0) + \mathrm{Re}\left\{\widetilde{C}_4(0)\exp\left(\mathrm{j}\omega t\right)\right\}\right)\frac{\partial\left(\overline{\phi}_\mathrm{s} + \mathrm{Re}\left\{\widetilde{\phi}_\mathrm{s}\exp\left(\mathrm{j}\omega t\right)\right\}\right)}{\partial z}\right)\Bigg|_{z=0} \\
&= \overline{r}_1 + \mathrm{Re}\left\{\widetilde{r}_1\exp\left(\mathrm{j}\omega t\right)\right\} - \overline{r}_{-1} - \mathrm{Re}\left\{\widetilde{r}_{-1}\exp\left(\mathrm{j}\omega t\right)\right\},
\end{aligned}
\tag{A.28}
$$

$$
\begin{aligned}
D_2 &\frac{\partial\left(\overline{C}_2 + \mathrm{Re}\left\{\widetilde{C}_2\exp\left(\mathrm{j}\omega t\right)\right\}\right)}{\partial z}\Bigg|_{z=0} \\
&+ \frac{z_2 D_2 F}{RT}\left(\left(\overline{C}_2(0) + \mathrm{Re}\left\{\widetilde{C}_2(0)\exp\left(\mathrm{j}\omega t\right)\right\}\right)\frac{\partial\left(\overline{\phi}_\mathrm{s} + \mathrm{Re}\left\{\widetilde{\phi}_\mathrm{s}\exp\left(\mathrm{j}\omega t\right)\right\}\right)}{\partial z}\right)\Bigg|_{z=0} \\
&+ D_5 \frac{\partial\left(\overline{C}_5 + \mathrm{Re}\left\{\widetilde{C}_5\exp\left(\mathrm{j}\omega t\right)\right\}\right)}{\partial z}\Bigg|_{z=0} \\
&+ \frac{z_5 D_5 F}{RT}\left(\left(\overline{C}_5(0) + \mathrm{Re}\left\{\widetilde{C}_5(0)\exp\left(\mathrm{j}\omega t\right)\right\}\right)\frac{\partial\left(\overline{\phi}_\mathrm{s} + \mathrm{Re}\left\{\widetilde{\phi}_\mathrm{s}\exp\left(\mathrm{j}\omega t\right)\right\}\right)}{\partial z}\right)\Bigg|_{z=0} = 0,
\end{aligned}
\tag{A.29}
$$

$$
\begin{aligned}
& D_3 \left.\frac{\partial\left(\overline{C}_3+\operatorname{Re}\left\{\widetilde{C}_3 \exp(\mathrm{j}\omega t)\right\}\right)}{\partial z}\right|_{z=0} \\
&\quad + \frac{z_3 D_3 F}{RT}\left.\left(\left(\overline{C}_3(0)+\operatorname{Re}\left\{\widetilde{C}_3(0)\exp(\mathrm{j}\omega t)\right\}\right)\frac{\partial\left(\overline{\phi}_{\mathrm{s}}+\operatorname{Re}\left\{\widetilde{\phi}_{\mathrm{s}}\exp(\mathrm{j}\omega t)\right\}\right)}{\partial z}\right)\right|_{z=0} \\
& + D_4 \left.\frac{\partial\left(\overline{C}_4+\operatorname{Re}\left\{\widetilde{C}_4 \exp(\mathrm{j}\omega t)\right\}\right)}{\partial z}\right|_{z=0} \\
& + \frac{z_4 D_4 F}{RT}\left.\left(\left(\overline{C}_4(0)+\operatorname{Re}\left\{\widetilde{C}_4(0)\exp(\mathrm{j}\omega t)\right\}\right)\frac{\partial\left(\overline{\phi}_{\mathrm{s}}+\operatorname{Re}\left\{\widetilde{\phi}_{\mathrm{s}}\exp(\mathrm{j}\omega t)\right\}\right)}{\partial z}\right)\right|_{z=0} \\
& + D_5 \left.\frac{\partial\left(\overline{C}_5+\operatorname{Re}\left\{\widetilde{C}_5 \exp(\mathrm{j}\omega t)\right\}\right)}{\partial z}\right|_{z=0} \\
& + \frac{z_5 D_5 F}{RT}\left.\left(\left(\overline{C}_5(0)+\operatorname{Re}\left\{\widetilde{C}_5(0)\exp(\mathrm{j}\omega t)\right\}\right)\frac{\partial\left(\overline{\phi}_{\mathrm{s}}+\operatorname{Re}\left\{\widetilde{\phi}_{\mathrm{s}}\exp(\mathrm{j}\omega t)\right\}\right)}{\partial z}\right)\right|_{z=0} = 0,
\end{aligned}
\tag{A.30}
$$

Once zeroth order relations are canceled, Eqs. (A.26)–(A.30 are reduced to give

$$\widetilde{C}_i(3\delta) = 0, \tag{A.31}$$

$$\widetilde{\phi}_{\mathrm{s}}(3\delta) = 0, \tag{A.32}$$

$$\widetilde{N}_1^s + \widetilde{N}_4^s = \widetilde{r}_1 - \widetilde{r}_{-1}, \tag{A.33}$$

$$\widetilde{N}_2^s + \widetilde{N}_5^s = 0, \tag{A.34}$$

$$\widetilde{N}_3^s + \widetilde{N}_4^s + \widetilde{N}_5^s = 0, \tag{A.35}$$

where

$$\widetilde{N}_i^s = D_i \left.\frac{\mathrm{d}\widetilde{C}_i}{\mathrm{d}z}\right|_{z=0} + \frac{z_i D_i F}{RT}\left.\left(\overline{C}_i \frac{\mathrm{d}\widetilde{\phi}_{\mathrm{s}}}{\mathrm{d}z} + \widetilde{C}_i \frac{\mathrm{d}\overline{\phi}_{\mathrm{s}}}{\mathrm{d}z}\right)\right|_{z=0}, \quad i = 1, 2, .., 5, \tag{A.36}$$

According to Eqs. (3.13)–(3.16), the reaction rates can be expressed as a function of one or more of the following variables: potential corrected for ohmic drop, surface concentration of Cu^{2+} and surface coverage of $Cu(I)$, *i.e.*,

$$r = f\left(E', C_1^{\mathrm{s}}, \theta_{Cu}\right). \tag{A.37}$$

Therefore, for the conditions of an EIS experiment, the reaction rate can be expressed as a Taylor series expansion with all second and higher order terms neglected as follows:

$$r(t) = \overline{r} + \left.\frac{\partial f}{\partial E'}\right|_{ss} \left(E'(t) - \overline{E}'\right) + \left.\frac{\partial f}{\partial C_1^{\mathrm{s}}}\right|_{ss} \left(C_1^{\mathrm{s}}(t) - \overline{C}_1^{\mathrm{s}}\right) + \left.\frac{\partial f}{\partial \theta_{Cu}}\right|_{ss} \left(\theta_{Cu}(t) - \overline{\theta}_{Cu}\right). \quad (A.38)$$

Substituting each term in parenthesis in Eq. (A.38) by Eq. (A.2) leaves

$$r(t) = \overline{r} + \left.\frac{\partial f}{\partial E'}\right|_{ss} \mathrm{Re}\left\{\widetilde{E}' \exp(\mathrm{j}\omega t)\right\} + \left.\frac{\partial f}{\partial C_1^{\mathrm{s}}}\right|_{ss} \mathrm{Re}\left\{\widetilde{C}_1^{\mathrm{s}} \exp(\mathrm{j}\omega t)\right\} + \left.\frac{\partial f}{\partial \theta_{Cu}}\right|_{ss} \mathrm{Re}\left\{\widetilde{\theta}_{Cu} \exp(\mathrm{j}\omega t)\right\}. \quad (A.39)$$

Eq. (A.39) can be re-written and a new variable $\widetilde{r}$ introduced as follows

$$\begin{aligned} r(t) &= \overline{r} + \mathrm{Re}\left\{\left(\left.\frac{\partial f}{\partial E'}\right|_{ss} \widetilde{E}' + \left.\frac{\partial f}{\partial C_1^{\mathrm{s}}}\right|_{ss} \widetilde{C}_1^{\mathrm{s}} + \left.\frac{\partial f}{\partial \theta_{Cu}}\right|_{ss} \widetilde{\theta}_{Cu}\right) \exp(\mathrm{j}\omega t)\right\} \\ &= \overline{r} + \mathrm{Re}\left\{\widetilde{r} \exp(\mathrm{j}\omega t)\right\}, \end{aligned} \quad (A.40)$$

where

$$\widetilde{r} = \left.\frac{\partial f}{\partial E'}\right|_{ss} \widetilde{E}' + \left.\frac{\partial f}{\partial C_1^{\mathrm{s}}}\right|_{ss} \widetilde{C}_1^{\mathrm{s}} + \left.\frac{\partial f}{\partial \theta_{Cu}}\right|_{ss} \widetilde{\theta}_{Cu}. \quad (A.41)$$

This result can be applied to each of the expressions in Eqs. (3.13)–(3.16) by setting f to be r_1, r_{-1}, r_2 and r_{-2} in turn. This yields

$$\begin{aligned} \widetilde{r}_1 = &\left[-\beta_1 \frac{F}{RT} k_1 \exp\left(-\beta_1 \frac{F\overline{E}'}{RT}\right) \overline{C}_1^{\mathrm{s}} (1 - \overline{\theta}_{Cu})\right] \widetilde{E}' \\ &+ \left[k_1 \exp\left(-\beta_1 \frac{F\overline{E}'}{RT}\right) (1 - \overline{\theta}_{Cu})\right] \widetilde{C}_1^{\mathrm{s}} \\ &- \left[k_1 \exp\left(-\beta_1 \frac{F\overline{E}'}{RT}\right) \overline{C}_1^{\mathrm{s}}\right] \widetilde{\theta}_{Cu}, \end{aligned} \quad (A.42)$$

$$\begin{aligned} \widetilde{r}_{-1} = &\left[(1 - \beta_1) \frac{F}{RT} k_{-1} \exp\left((1 - \beta_1) \frac{F\overline{E}'}{RT}\right) \overline{\theta}_{Cu}\right] \widetilde{E}' \\ &+ \left[k_{-1} \exp\left((1 - \beta_1) \frac{F\overline{E}'}{RT}\right)\right] \widetilde{\theta}_{Cu}, \end{aligned} \quad (A.43)$$

$$\begin{aligned} \widetilde{r}_2 = &\left[-\beta_2 \frac{F}{RT} k_2 \exp\left(-\beta_2 \frac{F\overline{E}'}{RT}\right) \overline{\theta}_{Cu}\right] \widetilde{E}' \\ &+ \left[k_2 \exp\left(-\beta_2 \frac{F\overline{E}'}{RT}\right)\right] \widetilde{\theta}_{Cu}, \end{aligned} \quad (A.44)$$

$$\widetilde{r}_{-2} = \left[(1-\beta_2)\frac{F}{RT}k_{-2}\exp\left((1-\beta_2)\frac{F\overline{E}'}{RT}\right)(1-\overline{\theta}_{Cu})\right]\widetilde{E}' - \left[k_{-2}\exp\left((1-\beta_2)\frac{F\overline{E}'}{RT}\right)\right]\widetilde{\theta}_{Cu}. \tag{A.45}$$

In order to determine $\widetilde{E}'$, Eqs. (A.1) and (A.2) are substituted into (3.10):

$$\begin{aligned}\overline{E}' + \mathrm{Re}\left\{\widetilde{E}'\exp(\mathrm{j}\omega t)\right\} &= \overline{E} + \mathrm{Re}\left\{\widetilde{E}\exp(\mathrm{j}\omega t)\right\} - \overline{i}R_\mathrm{s} - \mathrm{Re}\left\{\widetilde{i}\exp(\mathrm{j}\omega t)\right\}R_\mathrm{s} \\ &= \overline{E} - \overline{i}R_\mathrm{s} + \mathrm{Re}\left\{\left(\widetilde{E} - \widetilde{i}R_\mathrm{s}\right)\exp(\mathrm{j}\omega t)\right\}.\end{aligned} \tag{A.46}$$

By matching zeroth and first order terms in $\exp(\mathrm{j}\omega t)$, the following expressions are obtained

$$\overline{E}' = \overline{E} - \overline{i}R_\mathrm{s}, \tag{A.47}$$

$$\mathrm{Re}\left\{\widetilde{E}'\exp(\mathrm{j}\omega t)\right\} = \mathrm{Re}\left\{\left(\widetilde{E} - \widetilde{i}R_\mathrm{s}\right)\exp(\mathrm{j}\omega t)\right\}. \tag{A.48}$$

Eq. (A.48) can be rearranged to yield

$$\mathrm{Re}\left\{\left(\widetilde{E}' - \widetilde{E} + \widetilde{i}R_\mathrm{s}\right)\exp(\mathrm{j}\omega t)\right\} = 0. \tag{A.49}$$

The requirement that this equality hold for all values of t leads to

$$\widetilde{E}' = \widetilde{E} - \widetilde{i}R_\mathrm{s}. \tag{A.50}$$

Now, the same procedure is followed to obtain an expression for $\widetilde{\theta}_{Cu}$. Eqs. (A.2) and (A.40) are substituted into Eq. (3.18) to yield

$$\begin{aligned}\Gamma\frac{\partial\left(\overline{\theta}_{Cu} + \mathrm{Re}\left\{\widetilde{\theta}_{Cu}\exp(\mathrm{j}\omega t)\right\}\right)}{\partial t} &= \overline{r}_1 + \mathrm{Re}\left\{\widetilde{r}_1\exp(\mathrm{j}\omega t)\right\} - \overline{r}_{-1} - \mathrm{Re}\left\{\widetilde{r}_{-1}\exp(\mathrm{j}\omega t)\right\} \\ &- \overline{r}_2 - \mathrm{Re}\left\{\widetilde{r}_2\exp(\mathrm{j}\omega t)\right\} + \overline{r}_{-2} + \mathrm{Re}\left\{\widetilde{r}_{-2}\exp(\mathrm{j}\omega t)\right\},\end{aligned} \tag{A.51}$$

$$\Gamma\mathrm{Re}\left\{\frac{\partial\left(\widetilde{\theta}_{Cu}\exp(\mathrm{j}\omega t)\right)}{\partial t}\right\} = \overline{r}_1 - \overline{r}_{-1} - \overline{r}_2 + \overline{r}_{-2} + \mathrm{Re}\left\{(\widetilde{r}_1 - \widetilde{r}_{-1} - \widetilde{r}_2 + \widetilde{r}_{-2})\exp(\mathrm{j}\omega t)\right\}, \tag{A.52}$$

From the zeroth order problem, $\overline{r}_1 - \overline{r}_{-1} - \overline{r}_2 + \overline{r}_{-2}$=0 and thus Eq. (A.52) is simplified to

$$\Gamma\mathrm{j}\omega\widetilde{\theta}_{Cu} = \widetilde{r}_1 - \widetilde{r}_{-1} - \widetilde{r}_2 + \widetilde{r}_{-2}, \tag{A.53}$$

where $\widetilde{r}_1$, $\widetilde{r}_{-1}$, $\widetilde{r}_2$ and $\widetilde{r}_{-2}$ are given by Eqs. (A.42)–(A.45). $\widetilde{i}$ is calculated by substituting Eq. (A.2) into (3.9)

$$\overline{i} + \mathrm{Re}\left\{\widetilde{i}\exp\left(\mathrm{j}\omega t\right)\right\} = \overline{i}_{\mathrm{f}} + \mathrm{Re}\left\{\widetilde{i}_{\mathrm{f}}\exp\left(\mathrm{j}\omega t\right)\right\} + C_{\mathrm{dl}}\frac{\partial\left(\overline{E}' + \mathrm{Re}\left\{\widetilde{E}'\exp\left(\mathrm{j}\omega t\right)\right\}\right)}{\partial t}, \quad \text{(A.54)}$$

Since $\overline{i} = \overline{i}_{\mathrm{f}}$, then Eq. (A.54) results in the following expression

$$\widetilde{i} = \widetilde{i}_{\mathrm{f}} + C_{\mathrm{dl}}\mathrm{j}\omega\widetilde{E}'. \quad \text{(A.55)}$$

An expression for $\widetilde{i}_{\mathrm{f}}$ results from the substitution of Eq. (A.2) into (3.17), *i.e.*,

$$\begin{aligned}\overline{i}_{\mathrm{f}} + \mathrm{Re}\left\{\widetilde{i}_{\mathrm{f}}\exp\left(\mathrm{j}\omega t\right)\right\} &= -F\overline{r}_1 - F\mathrm{Re}\left\{\widetilde{r}_1\exp\left(\mathrm{j}\omega t\right)\right\} + F\overline{r}_{-1} + F\mathrm{Re}\left\{\widetilde{r}_{-1}\exp\left(\mathrm{j}\omega t\right)\right\} \\ &\quad - F\overline{r}_2 - F\mathrm{Re}\left\{\widetilde{r}_2\exp\left(\mathrm{j}\omega t\right)\right\} + F\overline{r}_{-2} + F\mathrm{Re}\left\{\widetilde{r}_{-2}\exp\left(\mathrm{j}\omega t\right)\right\} \\ &= -F(\overline{r}_1 - \overline{r}_{-1} + \overline{r}_2 - \overline{r}_{-2}) + \mathrm{Re}\left\{-F\left(\widetilde{r}_1 - \widetilde{r}_{-1} + \widetilde{r}_2 - \widetilde{r}_{-2}\right)\,\exp\left(\mathrm{j}\omega t\right)\right\}. \quad \text{(A.56)}\end{aligned}$$

Since $\overline{i}_{\mathrm{f}} = -F(\overline{r}_1 - \overline{r}_{-1} + \overline{r}_2 - \overline{r}_{-2})$, then Eq. (A.56) simplifies to

$$\widetilde{i}_{\mathrm{f}} = -F\left(\widetilde{r}_1 - \widetilde{r}_{-1} + \widetilde{r}_2 - \widetilde{r}_{-2}\right). \quad \text{(A.57)}$$

A.2 Additive Model

The derivation of the mass balance equations of the model of copper electrodeposition in the presence of Cl^- and PEG is similar to that followed in Section A.1. Only the linearization of the reaction rate expressions is presented here. The reaction rates r_1 to r_6 are functions of the potential corrected for ohmic drop, the surface concentrations of Cu^{2+}, Cl^- and PEG and the surface coverages of $Cu(I)$, $CuCl$ and $ClCuPEG$, *i.e.*,

$$r = f\left(E', C^{\mathrm{s}}_{Cu}, C^{\mathrm{s}}_{Cl}, C^{\mathrm{s}}_{P}, \theta_{Cu}, \theta_{Clc}, \Gamma_p\right). \quad \text{(A.58)}$$

The reaction rates can also be expressed as follows:

$$\begin{aligned}r(t) = \overline{r} &+ \left.\frac{\partial f}{\partial E'}\right|_{ss}\left(E'(t) - \overline{E}'\right) + \left.\frac{\partial f}{\partial C^{\mathrm{s}}_{Cu}}\right|_{ss}\left(C^{\mathrm{s}}_{Cu}(t) - \overline{C}^{\mathrm{s}}_{Cu}\right) + \left.\frac{\partial f}{\partial C^{\mathrm{s}}_{Cl}}\right|_{ss}\left(C^{\mathrm{s}}_{Cl}(t) - \overline{C}^{\mathrm{s}}_{Cl}\right) \\ &+ \left.\frac{\partial f}{\partial C^{\mathrm{s}}_{P}}\right|_{ss}\left(C^{\mathrm{s}}_{P}(t) - \overline{C}^{\mathrm{s}}_{P}\right) + \left.\frac{\partial f}{\partial \theta_{Cu}}\right|_{ss}\left(\theta_{Cu}(t) - \overline{\theta}_{Cu}\right) \\ &+ \left.\frac{\partial f}{\partial \theta_{Clc}}\right|_{ss}\left(\theta_{Clc}(t) - \overline{\theta}_{Clc}\right) + \left.\frac{\partial f}{\partial \Gamma_p}\right|_{ss}\left(\Gamma_p(t) - \overline{\Gamma}_P\right). \quad \text{(A.59)}\end{aligned}$$

Substituting Eq. (A.2) for each term in parenthesis in Eq. (A.59) and rearranging leaves

$$r(t) = \overline{r} + \mathrm{Re}\left\{\widetilde{r}\exp\left(\mathrm{j}\omega t\right)\right\}, \tag{A.60}$$

where

$$\begin{aligned}\widetilde{r} = \left.\frac{\partial f}{\partial E'}\right|_{ss}\widetilde{E}' + \left.\frac{\partial f}{\partial C^{\mathrm{s}}_{Cu}}\right|_{ss}\widetilde{C}^{\mathrm{s}}_{Cu} + \left.\frac{\partial f}{\partial C^{\mathrm{s}}_{Cl}}\right|_{ss}\widetilde{C}^{\mathrm{s}}_{Cl} + \left.\frac{\partial f}{\partial C^{\mathrm{s}}_{P}}\right|_{ss}\widetilde{C}^{\mathrm{s}}_{P} + \left.\frac{\partial f}{\partial \theta_{Cu}}\right|_{ss}\widetilde{\theta}_{Cu}& \\ + \left.\frac{\partial f}{\partial \theta_{Clc}}\right|_{ss}\widetilde{\theta}_{Clc} + \left.\frac{\partial f}{\partial \Gamma_p}\right|_{ss}\widetilde{\Gamma}_{P}.&\end{aligned} \tag{A.61}$$

Eq. (A.61) is applied to the model when $\Gamma_p < \Gamma_0$ by setting f to be r_1, r_2, r_3, r_4, r_5 and r_6 given by Eqs. (5.23)–(5.28), resulting in the following:

$$\begin{aligned}\widetilde{r}_1 = &\left[-\beta_1\frac{F}{RT}k_1\exp\left(-\beta_1\frac{F\overline{E}'}{RT}\right)\overline{C}^{\mathrm{s}}_{Cu}\left(1-\overline{\theta}_{Cu}-\overline{\theta}_{Clc}-\frac{\overline{\Gamma}_p}{\Gamma_0}\right)\right]\widetilde{E}' \\ &+\left[k_1\exp\left(-\beta_1\frac{F\overline{E}'}{RT}\right)\left(1-\overline{\theta}_{Cu}-\overline{\theta}_{Clc}-\frac{\overline{\Gamma}_p}{\Gamma_0}\right)\right]\widetilde{C}^{\mathrm{s}}_{Cu} \\ &-\left[k_1\exp\left(-\beta_1\frac{F\overline{E}'}{RT}\right)\overline{C}^{\mathrm{s}}_{Cu}\right]\left(\widetilde{\theta}_{Cu}+\widetilde{\theta}_{Clc}+\frac{1}{\Gamma_0}\widetilde{\Gamma}_p\right),\end{aligned} \tag{A.62}$$

$$\begin{aligned}\widetilde{r}_2 = &\left[-\beta_2\frac{F}{RT}k_2\exp\left(-\beta_2\frac{F\overline{E}'}{RT}\right)\overline{\theta}_{Cu}\right]\widetilde{E}' \\ &-\left[(1-\beta_2)\frac{F}{RT}k_{-2}\exp\left((1-\beta_2)\frac{F\overline{E}'}{RT}\right)\left(1-\overline{\theta}_{Cu}-\overline{\theta}_{Clc}-\frac{\overline{\Gamma}_p}{\Gamma_0}\right)\right]\widetilde{E}' \\ &+\left[k_2\exp\left(-\beta_2\frac{F\overline{E}'}{RT}\right)+k_{-2}\exp\left((1-\beta_2)\frac{F\overline{E}'}{RT}\right)\right]\widetilde{\theta}_{Cu} \\ &+\left[k_{-2}\exp\left((1-\beta_2)\frac{F\overline{E}'}{RT}\right)\right]\left(\widetilde{\theta}_{Clc}+\frac{1}{\Gamma_0}\widetilde{\Gamma}_p\right),\end{aligned} \tag{A.63}$$

$$\begin{aligned}\widetilde{r}_3 = &\left[-\beta_3\frac{F}{RT}k_3\exp\left(-\beta_3\frac{F\overline{E}'}{RT}\right)\overline{C}^{\mathrm{s}}_{Cu}\overline{C}^{\mathrm{s}}_{Cl}\left(1-\overline{\theta}_{Cu}-\overline{\theta}_{Clc}-\frac{\overline{\Gamma}_p}{\Gamma_0}\right)\right]\widetilde{E}' \\ &+\left[k_3\exp\left(-\beta_3\frac{F\overline{E}'}{RT}\right)\left(1-\overline{\theta}_{Cu}-\overline{\theta}_{Clc}-\frac{\overline{\Gamma}_p}{\Gamma_0}\right)\right]\left(\overline{C}^{\mathrm{s}}_{Cl}\widetilde{C}^{\mathrm{s}}_{Cu}+\overline{C}^{\mathrm{s}}_{Cu}\widetilde{C}^{\mathrm{s}}_{Cl}\right) \\ &-\left[k_3\exp\left(-\beta_3\frac{F\overline{E}'}{RT}\right)\overline{C}^{\mathrm{s}}_{Cu}\overline{C}^{\mathrm{s}}_{Cl}\right]\left(\widetilde{\theta}_{Cu}+\widetilde{\theta}_{Clc}+\frac{1}{\Gamma_0}\widetilde{\Gamma}_p\right),\end{aligned} \tag{A.64}$$

$$\widetilde{r}_4 = \left[-\beta_4 \frac{F}{RT} k_4 \exp\left(-\beta_4 \frac{F\overline{E}'}{RT}\right) \overline{\theta}_{Clc}\right] \widetilde{E}' + \left[k_4 \exp\left(-\beta_4 \frac{F\overline{E}'}{RT}\right)\right] \widetilde{\theta}_{Clc}, \tag{A.65}$$

$$\widetilde{r}_5 = \left[k_5 \overline{\theta}_{Clc}\right] \widetilde{C}^{\mathrm{s}}_P + \left[k_5 \overline{C}^{\mathrm{s}}_P\right] \widetilde{\theta}_{Clc}. \tag{A.66}$$

$$\widetilde{r}_6 = \left[k_6 \overline{\Gamma}_p\right] \left(\widetilde{r}_2 + \widetilde{r}_4\right) + \left[k_6 \left(\overline{r}_2 + \overline{r}_4\right)\right] \widetilde{\Gamma}_p. \tag{A.67}$$

Eq. (A.67) also applies when $\Gamma_p \geq \Gamma_0$. The rest of the expressions are obtained from setting f in Eq. (A.61) to be r_1, r_2, r_3, r_4 and r_5 given by Eqs. (5.29)–(5.33) which results in the following:

$$\begin{aligned}\widetilde{r}_1 = &\left[-\beta_1 \frac{F}{RT} k_7\, k_1 \exp\left(-\beta_1 \frac{F\overline{E}'}{RT}\right) \overline{C}^{\mathrm{s}}_{Cu} (1 - \overline{\theta}_{Cu} - \overline{\theta}_{Clc})\right] \widetilde{E}' \\ &+ \left[k_7\, k_1 \exp\left(-\beta_1 \frac{F\overline{E}'}{RT}\right) (1 - \overline{\theta}_{Cu} - \overline{\theta}_{Clc})\right] \widetilde{C}^{\mathrm{s}}_{Cu} \\ &- \left[k_7\, k_1 \exp\left(-\beta_1 \frac{F\overline{E}'}{RT}\right) \overline{C}^{\mathrm{s}}_{Cu}\right] \left(\widetilde{\theta}_{Cu} + \widetilde{\theta}_{Clc}\right),\end{aligned} \tag{A.68}$$

$$\begin{aligned}\widetilde{r}_2 = &\left[-\beta_2 \frac{F}{RT} k_7\, k_2 \exp\left(-\beta_2 \frac{F\overline{E}'}{RT}\right) \overline{\theta}_{Cu}\right] \widetilde{E}' \\ &- \left[(1-\beta_2) \frac{F}{RT} k_7\, k_{-2} \exp\left((1-\beta_2) \frac{F\overline{E}'}{RT}\right) (1 - \overline{\theta}_{Cu} - \overline{\theta}_{Clc})\right] \widetilde{E}' \\ &+ \left[k_7\, k_2 \exp\left(-\beta_2 \frac{F\overline{E}'}{RT}\right) + k_7\, k_{-2} \exp\left((1-\beta_2) \frac{F\overline{E}'}{RT}\right)\right] \widetilde{\theta}_{Cu} \\ &+ \left[k_7\, k_{-2} \exp\left((1-\beta_2) \frac{F\overline{E}'}{RT}\right)\right] \widetilde{\theta}_{Clc},\end{aligned} \tag{A.69}$$

$$\begin{aligned}\widetilde{r}_3 = &\left[-\beta_3 \frac{F}{RT} k_7\, k_3 \exp\left(-\beta_3 \frac{F\overline{E}'}{RT}\right) \overline{C}^{\mathrm{s}}_{Cu} \overline{C}^{\mathrm{s}}_{Cl} (1 - \overline{\theta}_{Cu} - \overline{\theta}_{Clc})\right] \widetilde{E}' \\ &+ \left[k_7\, k_3 \exp\left(-\beta_3 \frac{F\overline{E}'}{RT}\right) (1 - \overline{\theta}_{Cu} - \overline{\theta}_{Clc})\right] \left(\overline{C}^{\mathrm{s}}_{Cl} \widetilde{C}^{\mathrm{s}}_{Cu} + \overline{C}^{\mathrm{s}}_{Cu} \widetilde{C}^{\mathrm{s}}_{Cl}\right) \\ &- \left[k_7\, k_3 \exp\left(-\beta_3 \frac{F\overline{E}'}{RT}\right) \overline{C}^{\mathrm{s}}_{Cu} \overline{C}^{\mathrm{s}}_{Cl}\right] \left(\widetilde{\theta}_{Cu} + \widetilde{\theta}_{Clc}\right),\end{aligned} \tag{A.70}$$

$$\widetilde{r}_4 = \left[-\beta_4 \frac{F}{RT} k_7 \; k_4 \exp\left(-\beta_4 \frac{F\overline{E}'}{RT} \right) \overline{\theta}_{Clc} \right] \widetilde{E}' + \left[k_7 \; k_4 \exp\left(-\beta_4 \frac{F\overline{E}'}{RT} \right) \right] \widetilde{\theta}_{Clc}, \tag{A.71}$$

$$\widetilde{r}_5 = \left[k_8 \overline{\theta}_{Clc} (\Gamma_s - \overline{\Gamma}_p) \right] \widetilde{C}^{\mathrm{s}}_P + \left[k_8 \overline{C}^{\mathrm{s}}_P (\Gamma_s - \overline{\Gamma}_p) \right] \widetilde{\theta}_{Clc} - \left[k_8 \overline{C}^{\mathrm{s}}_P \overline{\theta}_{Clc} \right] \widetilde{\Gamma}_p, \tag{A.72}$$